Summer 2021

# Phase formation and thermal conductivity of zirconium carbide

Yue Zhou



Department: Materials Science and Engineering

# PHASE FORMATION AND THERMAL CONDUCTIVITY OF ZIRCONIUM CARBIDE

by

YUE ZHOU

A DISSERTATION

Presented to the Graduate Faculty of the

MISSOURI UNIVERSITY OF SCIENCE AND TECHNOLOGY

In Partial Fulfillment of the Requirements for the Degree

DOCTOR OF PHILOSOPHY

in

MATERIALS SCIENCE AND ENGINEERING

2021

Approved by:

William Fahrenholtz, Advisor
Gregory Hilmas
Jeremy Watts
Wayne Huebner
Joseph Graham

## PUBLICATION DISSERTATION OPTION

This dissertation consists of the following articles, formatted in the style used by the Missouri University of Science and Technology:

Paper I, found on pages 20-40, has been published in the *Journal of the European Ceramic Society*.

Paper II, found on pages 41-58, has been published in the *Journal of the American Ceramic Society*.

Paper III, found on pages 59-90, has been published in the *Journal of Materials Science and Technology*.

Paper IV, found on pages 91-115, has been published to the *Journal of the American Ceramic Society*.

# ABSTRACT

This research focused on the synthesis and phase formation of zirconium carbide with different carbon contents, and lattice thermal conductivity of zirconium carbide with different carbon vacancy, hafnium, and oxygen contents.

Nominally pure phase $ZrC_X$ was synthesized by solid-state reaction of zirconium hydride ($ZrH_2$) and carbon black at a temperature as low as 1300°C. The powder synthesized at 1300°C was carbon deficient $ZrC_X$. Carbon stoichiometry of the as-synthesized powders increased as the synthesis temperature increased. As the synthesis temperature increase, the oxygen content of $ZrC_X$ decreased due to the increasing C site occupancy. Low stoichiometry $ZrC_{0.6}$ powders were synthesized at 1300°C and 2000°C, and the formed phases were investigated. Carbon vacancy ordered phases were detected by neutron diffraction and selected area electron diffraction.

Lattice thermal conductivities of $ZrC_X$ with different carbon contents (x=1.0, 0.75, 0.5) and different hafnium contents (3.125 at% and 6.25 at% were studied theoretically. A combination of first-principles calculations and the Debye-Callaway model was employed to predict the lattice thermal conductivities. Lattice thermal conductivities of all the compositions decreased as temperature increased. Increasing carbon vacancy content reduced the lattice thermal conductivity while increasing the grain size increased the lattice thermal conductivity. Lattice thermal conductivities of $ZrC_X$ also decreased as the content of Hf increased. Carbon vacancies and Hf impurities decreased the phonon transport, thus the lattice thermal conductivity decreased.

# ACKNOWLEDGEMENTS

First, I thank my academic advisor Dr. William Fahrenholtz for his guidance and ideas for my Ph.D. research. He ranked 270 as a world materials scientist by a Stanford study, thus his profound understanding of ultra-high temperature ceramics and phase diagrams drove my research. As the editor-in-chief of the Journal of the American Ceramic Society, he helped me a lot with my paper writing; I cherished this very much as an international student. His reputation in ceramics yielded the opportunities for me to present my research to the world at international conferences.

I thank Dr. Gregory Hilmas. He always has ideas and suggestions for my work. His facilities and instrumentation resources gave me the opportunities to perform experiments based on my ideas.

I appreciate our associate research professor Dr. Jeremy Watts. He maintains facilities and instruments very well. My experiments were never delayed. I also learned a lot of experimental and process methods from him.

Finally, I thank Dr. Joseph Graham for his help with my theoretical studies. He has a broad knowledge based of solid-state physics and quantum mechanics, which makes him understand my calculation results well. I learned about quantum mechanics from him and realized that I need to learn much more for my future work.

# TABLE OF CONTENTS

Page

# LIST OF ILLUSTRATIONS

SECTION Page

PAPER IV

# LIST OF TABLES

SECTION Page

PAPER IV

# 1. INTRODUCTION

Zirconium carbide is a promising barrier layer material for tristructural-isotropic (TRISO) fuel particles that are employed in high-temperature gas-cooled reactors. Typically, that barrier layer is made of SiC. Due to the better stability under irradiation and mechanical integrity of ZrC, it could substitute for SiC in the future. Thus, it is essential to study the thermal properties of ZrC.

The most commonly used synthesis method to produce ZrC is carbothermal reduction. However, carbon stoichiometry is difficult to control for $ZrC_x$ synthesis due to the range of carbon stoichiometry and dissolved oxygen is difficult to remove. According to some theoretical $ZrC_x$ crystal structure and phase studies, carbon vacancy ordered phase preferred to form in $ZrC_x$ when x approaches the lower limit for stability of the rock salt structure. This contradicts the extensively accepted Zr-C phase diagram that is based on the experimental findings, which does not show vacancy ordering. Carbon stoichiometry affects the thermal conductivity of $ZrC_x$. Systematic theoretical and experimental studies are needed. In addition, it is impossible to completely separate Zr and Hf from each other. Hf impurities are present in $ZrC_x$ before and after synthesis. However, the effects of Hf impurities on the thermal conductivity of ZrC was rarely discussed in previous works.

In this research, solid state reaction was used for synthesis of $ZrC_x$ with controlled carbon stoichiometry. Starting materials were $ZrH_2$ and carbon black with different mixing ratios. Dissolved oxygen levels were characterized in different $ZrC_x$ compositions. Phase formation of $ZrC_{0.6}$ was investigated using neutron diffraction and

selected area electron diffraction. Ordered phase can be formed after solid state reaction synthesis without a long period of isothermal holding. Different synthesis temperatures did not affect the vacancy ordering degree significantly. Lattice thermal conductivities of $ZrC_x$ with different carbon contents were calculated using first-principles calculation combined with the Debye-Callaway model method. Lattice thermal conductivity decreased as temperature increased. As the carbon content increased, lattice thermal conductivity decreased. The natural distributions of Zr isotopes, grain boundaries, and the interactions between phonons negatively affected lattice thermal conductivity. Hf impurities in $ZrC_x$ reduced the lattice thermal conductivity. A small amount of Hf decreased the lattice thermal conductivity of ZrC significantly. While further increase the Hf impurity content did not affected the lattice thermal conductivity a lot.

Zirconium carbide powder synthesis, the formed phases, and the intrinsic thermal properties were studied in this thesis; there were four objectives. First, the effects of the Zr:C and synthesis temperatures on the synthesized $ZrC_x$ powders were studied. Second, carbon vacancy ordering was quantified in $ZrC_{0.6}$ synthesized at different temperatures. Third, lattice thermal conductivities of $ZrC_x$ with different carbon contents were predicted using a combined method of first-principles calculations and the Debye-Callaway model. Fourth, a theoretical study of the effects of Hf impurities on $ZrC_x$ lattice thermal conductivity was conducted.

# LITERATURE REVIEW

## 2.1. ZIRCONIUM CARBIDE PROPERTIES

Zirconium carbide, as one of the transition metal monocarbides (TMCs), belongs to the family of ultra-high temperature ceramics (UHTCs)[1]. It has a combination of properties including high melting point (3420°C)[2], high strength (> 400MPa) and hardness (> 25 GPa)[3], high thermal conductivity (> 20W/m·K)[4], low electric resistivity (~ 60 μΩ·cm)[5], excellent corrosion resistance[6][7], and good thermal stability[8][9]. Zirconium carbide has a relatively high thermal conductivity among TMCs[10], which is a merit for using it in nuclear applications. In previously published reports, thermal conductivities of $ZrC_x$ were measured [8][9][11][12][13]. However, those measured values had discrepancies as shown in Figure 2.1. In one study, ZrC with a relative density of 93.3% had a thermal conductivity range of 31 to 38 W/m·K at temperatures from 200 to 1000°C [12]. In another study, ZrC with relative density of 91.9% had a thermal conductivity range from 18 to 26 W/m·K at temperatures ranging from 300 to 1100°C [11]. The differences between those values were due to the different average grain sizes, carbon vacancy contents, and porosity levels of the sintered $ZrC_x$ ceramics. The sintering methods and characteristics of $ZrC_x$ in previous studies are summarized in Table 2.1. In those studies, ZrC ceramics with larger grain sizes, lower carbon vacancy contents, and higher relative densities possessed the highest thermal conductivities.

**2.1.1. Phase and Crystal Structure.** A phase diagram of the Zr-C system is shown in Figure 2.2[14]. The $ZrC_x$ phase had a carbon stoichiometry ranging from 0.63 to 0.98 based on an experimental study[2]. In this carbon stoichiometry range, $ZrC_x$ was

stable in the rock-salt crystal structure ($Fm\bar{3}m$, space group No. 225) as shown in Figure 2.3. The sublattices of both Zr and C are face centered cubic.

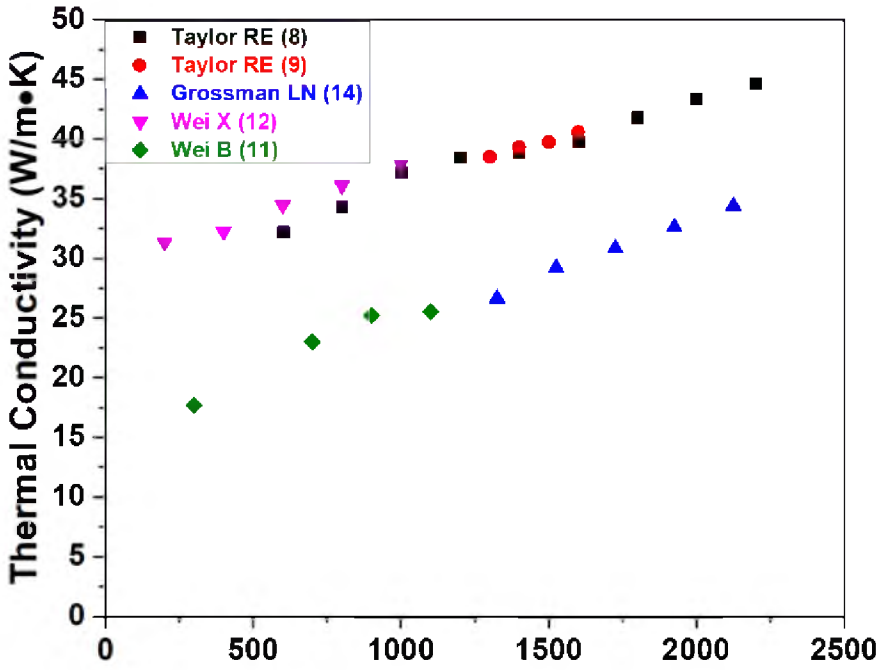


Figure 2.1. Thermal conductivities of zirconium carbide ceramics measured in previous studies.

For $ZrC_x$, experimental studies revealed that carbon vacancies can be ordered, which results in the formation of a superlattice. For example, $ZrC_{0.61}$ powder synthesized using a mechanochemical method and densified by spark plasma sintering contained ordered carbon vacancies as shown by selected area electron diffraction (SAED)[15]. In another study, a $ZrC_{0.7}$ sample prepared by arc-melting followed by annealing had a

Table 2.1. Densification methods and sample characteristics of $ZrC_x$ from previous studies sorted by highest to lowest thermal conductivity.

| Ref. | Densification method | Composition | Relative density | Average grain size | Impurity Content | Thermal conductivity (W/m·K) |
|---|---|---|---|---|---|---|
| 8 | HP | $ZrC_{0.98}$ | 95% | 50 μm | <0.2 wt% | 32.2, 600°C |
| 13 | HP | $ZrC_{0.98}$ | 95% | 50 μm | <0.2 wt% | 38.5, 1300°C |
| 12 | SPS | ZrC | 93.3% | ~10 μm | N/A | 31.3, 200°C |
| 14 | HP | ZrC | 91.5% | N/A | >0.165 wt% | 26.7, 1325°C |
| 11 | HP | ZrC | 91.9% | 3.7 μm | N/A | 17.7, 300°C |

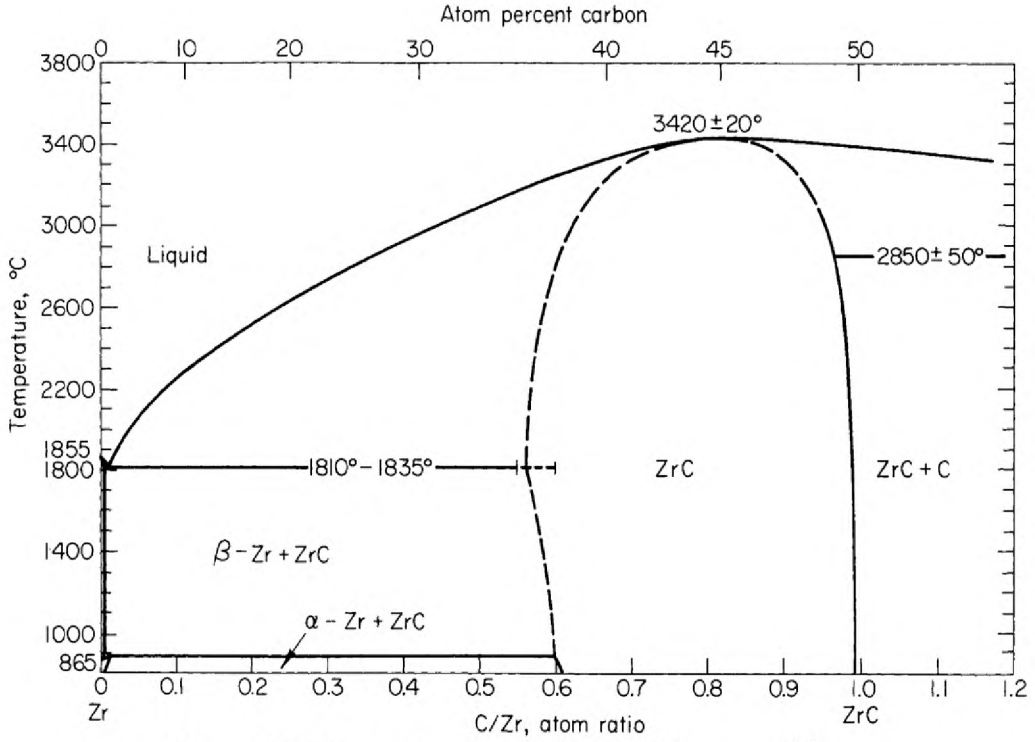


Figure 2.2. Phase diagram of the Zr-ZrC system[14].

superlattice as revealed using a combination characterization methods including electrical resistivity, differential thermal analysis, and X-ray diffraction[16]. In addition to experimental studies, carbon vacancy ordering in sub-stoichiometric zirconium carbide

was studied theoretically[17][18]. Figure 2.4 shows a computational Zr-C phase diagram[19]. According to this study, ordered phases of $ZrC_x$ could be formed at temperatures under 1300 K for carbon stoichiometries ranging from x = 0.5 to 0.98. In two theoretical studies, stable and meta-stable $ZrC_x$ crystal structures were predicted by combining a cluster expansion method, first-principles calculations[20], and state-of-art evolutionary algorithms[21]. The stability of the crystal structure was determined based on the calculation of formation enthalpies. Ordered phases of $ZrC_x$ ranged across the entire carbon stoichiometry range from x = 0.5 to 1.

**2.1.2. Thermal Conductivity.** The total thermal conductivity of a material includes contributions from electron and phonon components. The electron contribution can be estimated using the Wiedemann-Franz law[22], $\kappa_e = \frac{L_0 T}{\rho}$, where $L_0 = 2.45\times10^{-8}$ $W/\Omega\cdot K^2$ is the theoretical Lorenz number, $T$ is the absolute temperature, and $\rho$ is the electrical resistivity. At low temperatures (<100 K), thermal conductivity is mainly (>95 %) due to phonon transport[23]. Electron transports dominate the thermal conductivity at high temperatures (>1000 K)[24]. In general, the thermal conductivity of $ZrC_x$ increases as temperature increases (Figure 2.1), in contrast to the trend in most ceramics. The thermal conductivity of $ZrC_x$ was also affected by carbon stoichiometry. Carbon vacancies in $ZrC_x$ scatter phonons and electrons, which decreased the thermal conductivity as x increased[25]. The thermal conductivity of ZrC decreased as relative density decreased[12] and porous ZrC can be considered as a high-temperature insulation material[26][27]. Impurities in $ZrC_x$ also decrease the thermal conductivity. Common impurities in

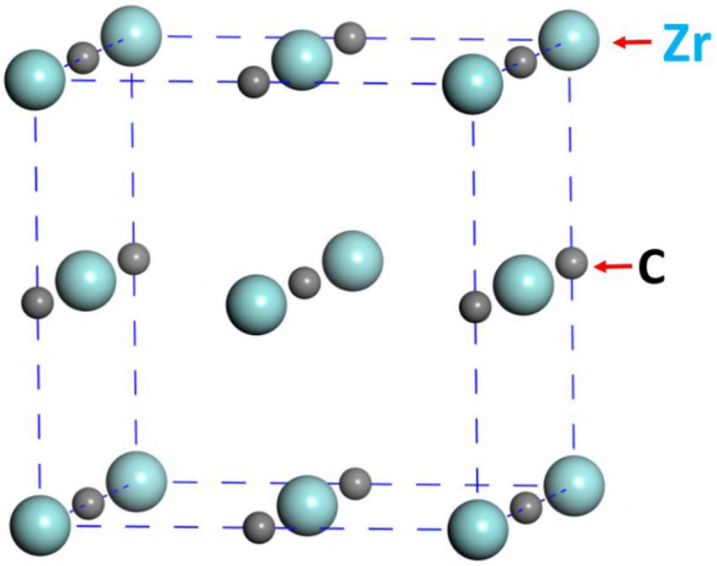


Figure 2.3. Crystal structure of ZrC.

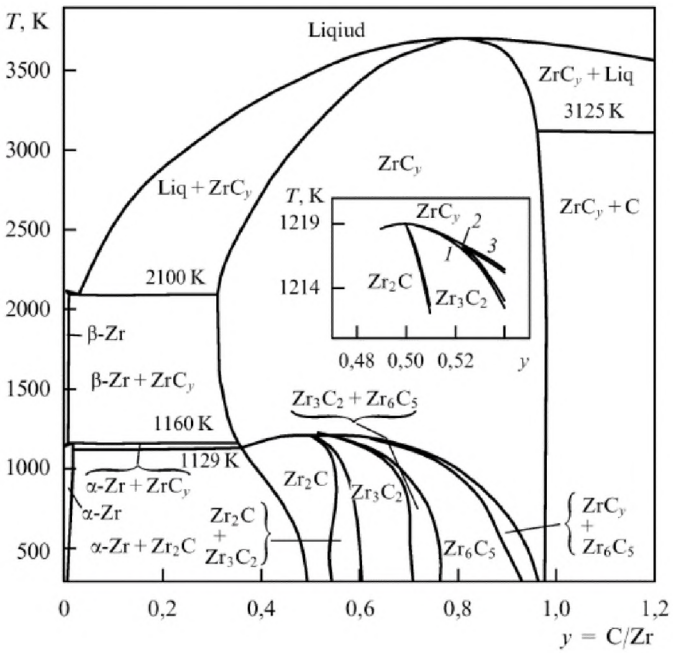


Figure 2.4. Computational Zr-C phase diagram[17].

zirconium carbide include hafnium[28], oxygen, and nitrogen. A study revealed that a composite that consisted of $C/ZrO_2/ZrC$, had a thermal conductivity as low as 0.057 $W/m \cdot K$[29].

## 2.2. SAMPLE PREPARATION

High yield and low cost synthesis methods are in demand for producing $ZrC_x$ powder with controlled composition and particle size. Densification methods for fabricating bulk $ZrC_x$ ceramics with high-relative density and low impurity contents also need to be studied.

**2.2.1. $ZrC_x$ Synthesis.** $ZrC_x$ can be synthesized using different methods established by previous studies. For preparing $ZrC_x$ coatings, chemical vapor deposition (CVD) is the most common method, and it uses the reaction between zirconium halides (e.g., $ZrCl_4$) and hydrocarbon compounds (e.g., $CH_4$)[30][31]. Molten salt synthesis was also developed to coat ZrC on the surface of flake graphite at a temperature as low as 900°C[32]. Hexagonal shaped ZrC platelets were formed after self-propagating high-temperature synthesis when 20 mass% of Al was added into starting Zr and C powders[33]. Solid-state reaction, carbothermal reduction, molten salt synthesis, electrochemical synthesis, laser pyrolysis, and mechanochemical synthesis methods were used for powder synthesis in previous studies [34][35][36][37][38][39][40][41][42][43]. Compared with other synthesis methods, solid state reaction and carbothermal reaction have advantages that include: they are relatively simple; they control the particle morphology; and they can control carbon stoichiometry. However, carbothermal reaction synthesis requires high reaction temperatures and long holding periods due to the high enthalpy of

ZrC formation, and the need to remove residual oxygen from the resulting powder particles. Particle size increases as the synthesis temperature increases.

**2.2.2. $ZrC_x$ Densification.** Bulk ceramics made of $ZrC_x$ are typically prepared by hot-pressing or spark plasma sintering (SPS)[44][12]. Hot-pressing is a necessary process to fabricate high quality monolithic $ZrC_x$ ceramics with low porosities. Understanding the mechanism progress is essential. Low carbon content $ZrC_x$ is easily densified according to an experimental study[45]. Sinterability decreased as carbon content increased. The mechanism of reaction hot-pressing (RHP) and the progress of $ZrC_x$ densification were studied theoretically[46]. For single step RHP, at the initiation of densification, starting materials of Zr and C were densified at a certain rate. Then, the densification rate suddenly accelerated due to the creep of Zr. At the same time, the content of the hard $ZrC_x$ phase kept increasing. This stage ended after approximately 30-40 vol% of the Zr had reacted Zr and the system contained 40-50 vol% of the hard $ZrC_x$ phase. As the pores were removed, the densification rate decreased, and finally reached a constant rate. Relative density during this stage increased initially due to the creep of Zr, then decreased once a certain amount of Zr had reacted because of the de-densification of $ZrC_x$ formation relative to the creep of Zr.

Based on previous reports, RHP is the best way to obtain high purity ZrC ceramics if the cost is not considered. The starting carbon must be well dispersed when mixing with the starting Zr to avoid the formation of graphite during hot pressing. Then, carbon must fully react with Zr during hot pressing. Annealing may be considered to remove the dissolved oxygen or nitrogen from the lattice.

## 2.3. OXIDATION AND NITRIDATION

Except for Hf, the most common impurities in $ZrC_x$ are O and N. Oxidation and nitridation can occur during powder synthesis or densification as well as during long-term exposure to air.

**2.3.1. ZrC Oxidation.** One of the disadvantages to zirconium carbide is that it has poor oxidation resistance. Oxidation can be inhibited by the formation of a dense oxidized layer on the outside of ZrC particles. Porous $ZrO_2$ layers are not able to protect ZrC particles[47]. In addition to the external oxide, O dissolves into the $ZrC_x$ lattice when using carbothermal reduction to synthesize ZrC. The O atoms substitute onto carbon sites in the lattice[48], and the dissolved oxygen increases the metal—non-metal bond strength[49]. Therefore, the dissolution of oxygen into $ZrC_x$ decreases the lattice parameter compared to $ZrC_x$ with carbon vacancies. The kinetics of ZrC oxidation have been

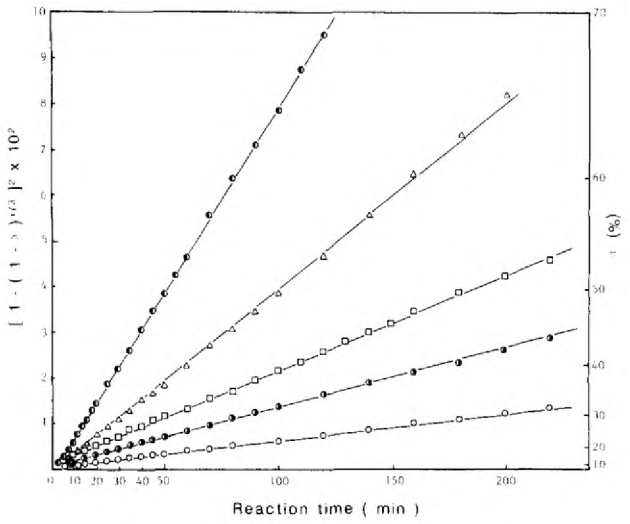


Figure 2.5. Jander's plot for the isothermal oxidation kinetics of ZrC at an oxygen pressure of 1.3 kPa at different temperatures[50].

studied previously. The reaction rate of ZrC and $O_2$ exhibited a linear relationship with with time for increasing temperatures that was calculated using Jander's equation[50], as

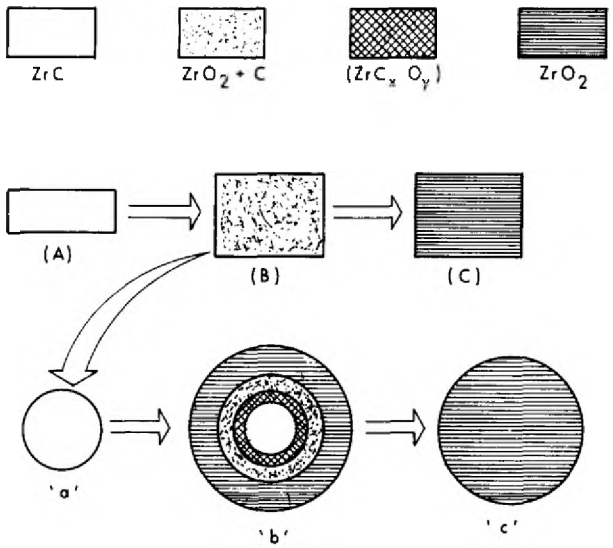


Figure 2.6. Mechanistic model for the oxidation of ZrC to $ZrO_2$[51].

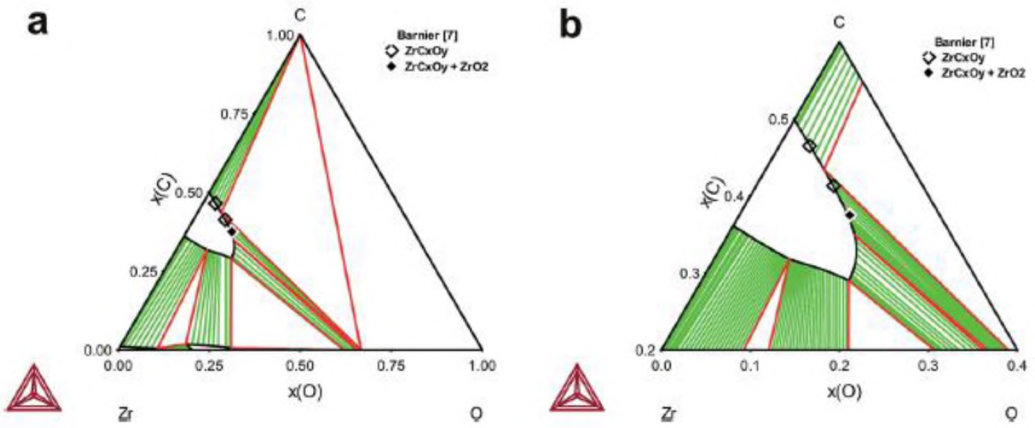


Figure 2.7. (a) Calculated isothermal section of the Zr-C-O system at 2000°C with experimental data; (b) focused on zirconium oxycarbide solid solution[58].

shown in Figure 2.5. The mechanism for ZrC oxidation was studied using X-ray diffraction. The ZrC sample was heated in a mixture gas of oxygen, and argon. Oxidation products at different degrees of progress were measured. During oxidation, oxygen diffused from the outside to the inside of the bulk ZrC. A zirconium oxycarbide layer was initially formed outside of the ZrC particle, then $ZrO_2$ formed as carbon separated from ZrC. Finally, all carbon of the carbon from the initial $ZrC_x$ reacted with oxygen. The final oxidation product was $ZrO_2$[51]. The progress of ZrC oxidation is depicted in Figure 2.6. At the beginning of oxidation, the cubic structure of $ZrO_2$ (preferred to grow in (220) orientation) was formed on the surface of ZrC because the crystal structure was stabilized by C. As oxidation progressed, the C content was reduced and the cubic $ZrO_2$ transformed into a monoclinic structure[52][53]. Usually, oxidized layers on ZrC surfaces have cracks due to the mismatch of the thermal expansion coefficients[54][55]. The weight of the oxidized layer presented a parabolic rise with time under certain temperatures and oxygen pressures[50][51][52]. Oxygen that was dissolved into the lattice of sub-stoichiometric $ZrC_x$ formed a zirconium oxycarbide phase. Zirconium oxycarbide ceramics have been made by solid state synthesis[49] for a composition of $ZrC_{0.64}O_{0.26}$ ,and for carbothermal reduction[56] using a composition range from $ZrC_{0.79}O_{0.13}$ to $ZrC_{0.97}O_{0.04}$. In addition, $ZrC_{0.6}O_{0.4}$ was formed using an oxygen diffusion method by heat treating $ZrC_{0.6}$[57]. Both $ZrC_x$ and $ZrC_{0.6}O_{0.4}$ were in ordered structures as determined by selected area electron diffraction (SAED). The Zr-O-C ternary phase diagrams at different temperatures were calculated using CALPHAD method based on experimental data. In the zirconium oxycarbide phase region, the maximum dissolved oxygen increased as

temperature increased. At 2000°C, the zirconium oxycarbide phase with highest oxygen content was $ZrC_{0.540}O_{0.298}$, as shown in Figure 2.7[58].

**2.3.2. $ZrC_x$ Nitridation.** Another common impurity in ZrC is nitrogen[59]. Zirconium carbonitrides synthesis has been described in previous reports. It was synthesized by magnetron sputtering with a flowing $Ar/N_2/C_2H_2$ atmosphere. The crystal structure was the same as ZrC[60]. The $ZrC_xN_y$ was also synthesized using a two-step carbothermal reduction-nitridation method. ZrC was first synthesized by carbothermal reduction. Then, the ZrC was that synthesized was nitrided under a flowing $H_2/N_2$ atmosphere[61].

## 2.4. ZrC IRRADIATION

The fourth-generation commercial nuclear reactors were built using high-temperature reactors that have outlet temperatures higher than 1000°C. The current fuel particles for those reactors are tri-isotropic (TRISO) particles, which consist of a number of layers. A cross-section image of a TRISO particle is shown in Figure 2.8. The kernel of the TRISO fuel particle could be $UO_2$, $UC_2$, or the mixture of the two. Outside of the kernel are layers including a porous pyrolytic carbon (buffer) layer, an inner pyrolytic carbon layer, SiC layer, and an outer dense pyrolytic carbon layer. The function of those layers, especially for the SiC layer, is to contain the fission products to prevent their diffusion out of the particle[62]. ZrC is a candidate to replace SiC in TRISO particles because it has a higher melting point and lower neutron-absorption cross-section than SiC. The SiC and ZrC layers are usually deposited on the particles by chemical vapor deposition (CVD)[63]. The properties of ZrC under irradiation and the diffusion of fission

products through ZrC were studied previously. ZrC is resistant to fission products generated from $UC_2$ and $(Th,U)O_2$ kernels. The mechanical integrity of ZrC is excellent after irradiated[64]. This is crucial for TRISO particles because the volume of ZrC can changed after irradiation due to the formation of defect clusters. The mechanisms of diffusion for fission products and their retention in ZrC are not clear. Although the fission elements have similar atomic radii to Zr, the formation energy of Zr vacancies is much higher than for the formation of C vacancies according to a theoretical study[65]. The diffusion parameters of Xe in $ZrC_x$ with different carbon stoichiometries were studied. The activation energy increased as carbon stoichiometry increased from x = 0.58 to 0.83. Then higher carbon content reduced the activation energy due to the decreased number of

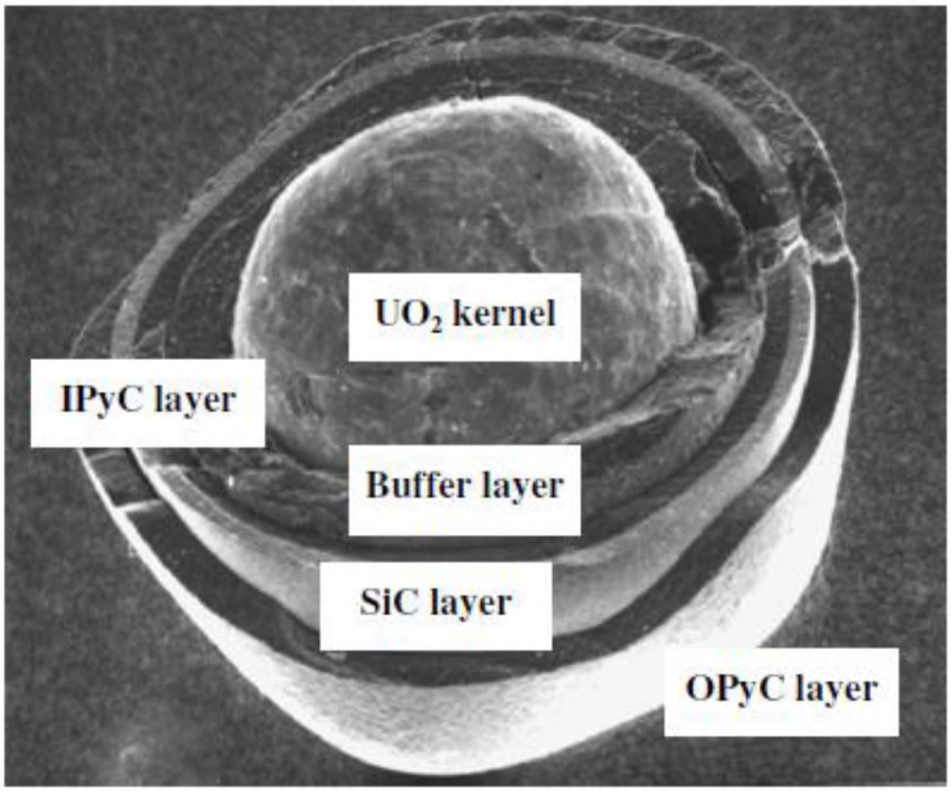


Figure 2.8. Cross section of current TRISO fuel particle.

C vacancies[66]. The release of $^{90}Sr$ in $ZrC_{1.3}$ (note that $ZrC_{1.3}$ contains both $ZrC_x$ and free C) was determined using volume diffusion. The diffusion rates in the grain bulk and grain boundary were approximately equal. The diffusion mechanism for $^{137}Cs$ and $^{144}Ce$ in $ZrC_{1.3}$ was determined as grain boundary diffusion[67]. ZrC inhibits the migration of $UO_2$, And other highly diffusive elements such as silver and europium isotopes, which can be retained in ZrC at high temperatures[68]. ZrC is sensitive to oxidation, therefore a ZrC layer can be used as an oxygen getter for the $UO_2$ kernel TRISO fuel particle. Directly coating a ZrC layer outside of the $UO_2$ kernel can retain all fission products after a long period of post-irradiation annealing at high temperatures[69]. In general, $ZrC_x$ was quite stable under neutron irradiation at different temperatures. After neutron irradiation, some unidentified dislocation loops were present in $ZrC_x$ as identified by TEM; the size of the loops increased with increasing temperature. Loop sizes in the bulk were larger than near the surface because of lack of surface sink. Lattice parameters were slightly larger than the non-irradiated ones. Mechanical properties increased after the irradiation treatment. Thermal conductivity decreased after irradiation due to increased phonon-scattering[70][71].

## 2.5. $ZrC_x$ THEORETICAL STUDIES

Theoretical studies of $ZrC_x$ have been used to study densification mechanisms, phase diagrams, crystal structures for different compositions, mechanical properties, chemical bonding, and thermal properties.

**2.5.1. Zr-C Phase Diagram.** A Zr-C phase diagram was calculated using an order parameter function method. Ordered single and double phases were determined

with carbon stoichiometries ranging from x = 0.5 to 1.0 under 1220 K, as shown in Figure 2.4[72].

**2.5.2. $ZrC_x$ Crystal Structures.** The ZrC crystal structure with vacancies, antisite defects, and interstitials was examined by calculating defect energeties with ab initio methods. The most favorable defect was carbon vacancy with carbon interstitials second. The highest defect energy was for the formation of Zr interstitials[73]. Crystal structures of $ZrC_x$ were investigated using a combination of cluster expansion methods and first-principles calculations. Ground states of $Zr_8C_7$, $Zr_6C_5$, $Zr_4C_3$, $Zr_3C_2$, and $Zr_2C$ were ordered phases with structures of *$P4_332$*, *C2/m*, *C2/m*, *Fddd*, and *Fd-3m,* respectively. The ordering enthalpy of $ZrC_x$ decreased with increasing carbon vacancy

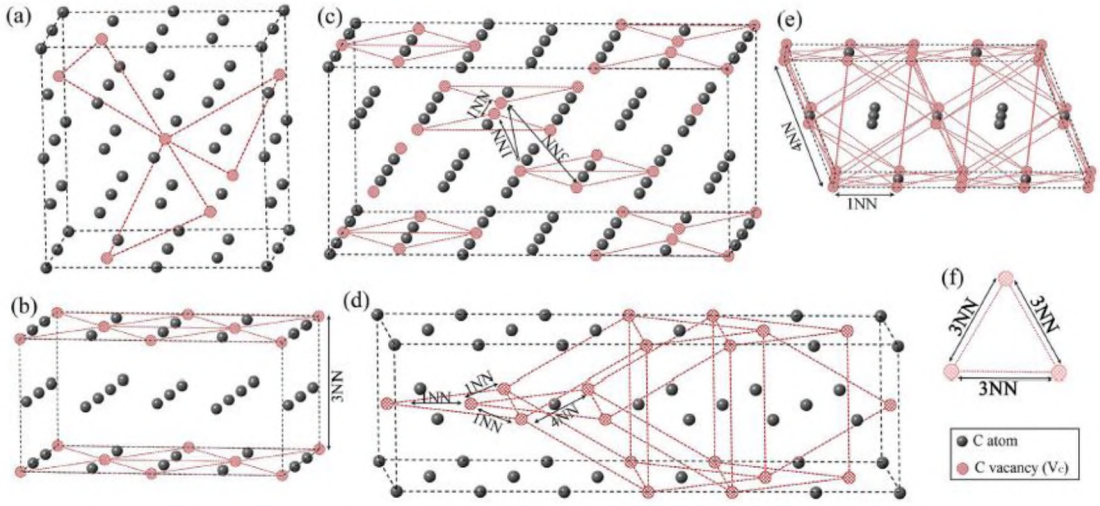


Figure 2.9. Carbon vacancy configurations in C-sublattice of (a) $Zr_8C_7$, (b) $Zr_6C_5$, (c) $Zr_4C_3$, (d) $Zr_3C_2$ and (e) $Zr_2C$. (Note: 1NN is the 1st nearest neighboring; 2NN is the 2nd nearest neighboring; 3NN is the 3rd nearest neighboring; 4NN is the 4th nearest neighboring.)

concentrations and it reached the lowest level when x was approximately 0.5. Carbon vacancy configurations of the C-sublattice for the ground states structures were also predicted, as shown in Figure 2.9[74]. Except for $Zr_2C$, the above compositions also had metastable phases as follows: *P-42₁m* for $Zr_8C_7$, *P3₁12* and *C2/c* for $Zr_6C_5$, *C2/m* for $Zr_4C_3$ and $Zr_3C_2$, and *P4₃32* for $Zr_8C_5$[75]. Their formation energies were slightly higher than their stable counterparts. Theoretical XRD patterns for stable and metastable phases included superlattice peaks. Similar results from the sub-stoichiometry $ZrC_x$ crystal structure were also calculated by USPEX code based on DFT and Vienna Ab-initio Simulation Package (VASP). Space groups of carbon vacancy ordered phases of $Zr_8C_7$, $Zr_7C_6$, $Zr_6C_5$, $Zr_5C_4$, $Zr_4C_3$, $Zr_3C_2$ and $Zr_2C$ are *P4₃32*, *R-3*, *C2/m*, *P-1*, *C2/c*, *C2/m*, and *Fd-3m*[76]. More details regarding the predicted crystal structures, such as atom positions and coordination numbers, were given in another theoretical study[21].

**2.5.3. $ZrC_x$ Theoretical Mechanical Properties.** Stable and metastable $ZrC_x$ phases were mentioned in 1.5.2[74]. For those structures, theoretical mechanical properties decreased as carbon content decreased. Elastic properties of $ZrC_x$ under pressure were studied using a norm-conserving pseudopotentials method. The structure became more dense under pressure, which increased the bulk modulus[79]. Effects of carbon vacancies and O/N impurities on the mechanical properties, which include bulk modulus, shear modulus, Pugh's ratio, and Vickers hardness, were calculated. In general, mechanical properties decayed with increased carbon vacancy content and oxygen concentration. However, nitrogen impurities slightly enhanced the mechanical properties[82].

**2.5.4. ZrC Chemical Bonding.** First-principles calculations were employed to study the electron density of states, electron charge density, and Mulliken population of

$ZrC_x$ using the CASTEP code. Electron density of states and electron charge density revealed the strong covalent bonds between Zr and C atoms. Ionic and metallic bonds were also present in the structure based on the Mulliken population data[77]. A strong nearest-neighbor force constant between Zr and C was disclosed. Carbon atoms were ionized by negative charges[78]. Carbon vacancies weakens the chemical bonding of Zr-C that included covalent bonds, and strength the Zr-Zr metallic bond[77].

**2.5.5. $ZrC_x$ Theoretical Thermal Conductivity.** The increasing thermal conductivities of $ZrC_x$ with increasing temperature were explained by a theoretical study. Phonon thermal conductivity was calculated using a molecular dynamic methods, and electron thermal conductivity was calculated with DFT using the same empirical potential as used for the phonon calculations. Phonon thermal conductivity decreased regularly with increasing temperature. The increase in total thermal conductivity with increasing temperature was attributed to the electron contribution to thermal conductivity. Carbon vacancies significantly affected the phonon thermal conductivity; however, the electron thermal conductivity was not affected by carbon vacancies. Two primary reasons were identified as the cause of the increasing electron thermal conductivity with increasing temperature. First, electron thermal conductivity was determined using theWiedemann-Franz law ($\kappa_e = L\sigma T$), where $L$ is the Lorenz number, $\sigma$ is electrical conductivity, and T is absolute temperature. ZrC was defined as a semi-metal, the Lorenz number of the semi-metal increased with increased temperature, which caused an increase in the electron contribution to thermal conductivity. Second, the electron density of states at the Fermi level increased with increasing temperature, which in turn increase the electron thermal conductivity[i]. In another study, electrical conductivity of ZrC was

calculated using Boltzmann transport approach from 0 K to 3500 K. At low temperatures, thermal conductivity initially increased sharply from 0 K to approximately 200 K, then it decreased with increasing temperatures and reached the lowest at approximately 1200 K. As the temperature further increased, thermal conductivity increased almost linearly. Grain boundaries restricted the transport of phonons, so the thermal conductivity was dependent on grain size and increased with increasing grain sizes[81].

## 2.6. ZrC APPLICATIONS

ZrC ceramics or composites containing ZrC can be used in rocket technology[82][83][84], cutting tools[85][86][87], nuclear reactor particle fuel[88][89][62][90][91][92][6], solar power receivers[93], and field emitter arrays[94]. The addition of ZrC can increase the ablation resistance of copper infiltrated tungsten, which is used for rudders in rocket motors. Pitch-derived ZrC/C composites also have good ablation resistance, making these composites suitable for aerospace applications. ZrC/W based composites are able to withstand ultra-high temperatures, so they can be used for rocket nozzles. Likewise, ZrC-$ZrB_2$ and ZrC-$TiB_2$ composites have superior mechanical properties; they are good candidates for cutting tools materials. ZrC is capable of retaining the fission product elements in the nuclear fuel kernel, so it is a promising barrier coating layer for TRISO fuel particles. Additionally, ZrC has good spectral selectivity, which is a well-known characteristics of ultra-high temperature ceramics. This property makes ZrC applicable for solar power receivers. ZrC is stable under high emitted currents. Combined with other properties, bulk and coating ZrC are promising for field emission applications.

## PAPER

# I. SYNTHESIS OF $ZRC_X$ WITH CONTROLLED CARBON STOICHIOMETRY BY LOW TEMPERATURE SOLID STATE REACTION

Yue Zhou*, Thomas W. Heitmann', William G. Fahrenholtz*, Gregory E. Hilmas*

**Department of Materials Science and Engineering, Missouri University of Science and Technology, Rolla, Missouri 65409, USA*

*'The Missouri Research Reactor, University of Missouri, Columbia, Missouri 65211, USA*

## ABSTRACT

Zirconium carbide ($ZrC_x$) powders were synthesized at temperatures between 1300°C and 2000°C by solid state reaction of zirconium hydride ($ZrH_2$) and carbon black. Crystal structure, lattice parameters and grain sizes of the as-synthesized $ZrC_x$ powders were characterized for two different starting $ZrH_2$:C ratios of 1:0.60 and 1:0.98. Powders with stoichiometry approaching $ZrC_{0.98}$ were synthesized at temperatures as low as 1600°C whereas $ZrC_x$ powders synthesized at lower temperatures had lower carbon contents regardless of the starting $ZrH_2$:C ratio. Crystallite sizes as small as about 50 nm were obtained due to the low synthesis temperature. Oxygen dissolved into the $ZrC_x$ lattice when carbon vacancies were present. Neutron diffraction analysis was used to determine that carbon stoichiometry increased and dissolved oxygen content decreased as synthesis temperature increased.

***Keywords*:** Zirconium carbide powder; Low temperature synthesis; X-ray diffraction; Carbon stoichiometry; Powder oxidation; Electron microscopy; Neutron diffraction; Intrinsic property.

## 1. INTRODUCTION

Zirconium carbide ($ZrC_x$) ceramics are proposed for use in extreme environments due to a combination of properties including high melting point (3420°C)[1], high strength (>400 MPa) and hardness (>25 GPA)[2], high thermal conductivity (>20 W/m·K) and low electrical resistivity (~60 μΩ·cm)[3], excellent corrosion resistance[4][5], and good thermal stability[6][7]. Some of the applications proposed for ZrCx ceramics include as a matrix or surface coating for fiber reinforced ultra-high temperature ceramic (UHTC) composites[8][9], and as structural or fission product barrier coatings for tri-isotropic (TRISO) coated nuclear fuel pellets[10].

Low cost and high yield methods are needed for the fabrication of powders with controlled composition and microstructure. Various methods have been reported for preparation of $ZrC_x$. Chemical vapor deposition (CVD) using the reaction between zirconium halides (e.g. $ZrCl_4$) and hydrocarbon compounds ($CH_4$) is the most common method for preparing $ZrC_x$ coatings[11][12]. Bulk $ZrC_x$ ceramics are typically prepared by hot-pressing (HP) or spark plasma sintering (SPS) of $ZrC_x$ powders with or without sintering aids[13][14]. For powder synthesis, solid state reactions[15][16][17][18], carbothermal reduction[19,20], molten salt synthesis[21], electrochemical synthesis[22] and laser pyrolysis[23][24] have been reported.

Solid state reaction and carbothermal reduction have several advantages compared to other synthesis methods including relatively simple processes along with control of the particle morphology of zirconium carbide and carbon stoichiometry. Mechanosynthesis of $ZrC_x$ was accomplished by grinding Zr and graphite powders by high-energy milling at room temperature[25]. Hexagonal monolayer platelets of (111) oriented $ZrC_x$ were grown by self-propagating high-temperature synthesis (SHS) using Al as an additive to control growth[26]. Nanocrystalline $ZrC_x$ was produced by reaction of $ZrO_2$, $Li_2CO_3$ and Mg in an autoclave at 600°C[27]. Zirconium oxycarbide powders with carbon stoichiometries ranging from 0.79 to 0.97 were synthesized by carbothermal reduction[28]. Nanosize particles $ZrC_x$ encased by a graphitic shell were synthesized by a combination of mechanical milling and annealing metal-carbon powder mixtures[29].

Carbothermal reduction is the most common method for synthesis of ZrCx and has been reported to occur in two steps[30]. During the first step, oxygen-rich primary zirconium oxycarbide forms by solid-gas reactions. The particles formed in the first step are covered by amorphous carbon. In the second step, secondary carbon-rich zirconium oxycarbide forms continuously on the primary zircnoium oxycarbide particles. Two zirconium oxycarbides consume each other forming a homogeneous composition. At the same time, oxygen is removed by reaction with the reducing environment that is rich in carbon monoxide. At the conclusion of the second stage, zirconium carbide powder with its highest carbon stoichiometry and minimum oxygen content is produced. Depending on the presence of impurities and the ratios of starting materials, oxygen can be present in different amounts in the zirconium oxycarbide lattice on carbon sites[28]. Unfortunately, many reports of synthesis of $ZrC_x$ do not analyze the resulting powders using methods

that can unambiguously determine carbon stoichiometry and oxygen content. For example, x-ray diffraction (XRD) analysis is the most common method used to characterize synthesized powders, but the lattice parameter of $ZrC_x$ has a complex relationship with carbon and oxygen contents that requires independent measurement of either oxygen or carbon content to explicitly determine carbon stoichiometry and dissolved oxygen content[31].

The purpose of this study was to investigate the effect of synthesis temperature and the starting ratio of zirconium to carbon on the composition of the resulting $ZrC_x$ powders.

## 2. EXPERIMENTAL

### 2.1. STARTING MATERIALS

Commercial $ZrH_2$ (Min. 95.5%, 27.1 μm, Chemadyne, LLC., Canoga Park, CA) and carbon black (BP-1100, Cabot Corporation, Alpharetta, GA, USA) powders were used as starting materials for $ZrC_x$ synthesis. The powders were batched with molar ratios of $ZrH_2$:C = 1:0.98 and 1:0.60. The powders were mixed by ball milling using zirconia grinding media in acetone for 12 hours under a rotation speed of 50 rpm. Afterward, rotary evaporation (Rotavapor R-124, Bucchi, Flawil, Germany) was employed to remove the acetone from the slurry at a temperature of 80°C, vacuum of 250 mmHg and a rotation speed of 90 rpm. For synthesis, pellets were produced by uniaxial pressing of three grams of mixed powder.

## 2.2. SYNTHESIS OF $ZRC_X$ POWDERS

Synthesis (Reaction 1 and 2, where *y* is the molar ratio of C to Zr in the starting powder) was conducted in a graphite element furnace (3060-FP20, Thermal Technology, Santa Rosa, CA, USA) under flowing argon. The mixed powder was heated from room temperature to 800°C at a heating rate of 10°C/min, and a dwell time of 2 hours to promote decomposition of $ZrH_2$. Synthesis was promoted by heating to temperatures ranging from 1300°C to 2000°C for 3 hours.

$$ZrH_{2(s)} \rightarrow Zr_{(s)} + H_{2(g)} \tag{1}$$

$$Zr_{(s)} + yC_{(s)} \rightarrow ZrC_{x(s)} + (y-x)C_{(s)} \tag{2}$$

## 2.3. CHARACTERIZATION

Phases were identified using X-ray diffraction (XRD, PANalytical X'Pert3 Powder, Malvern Panalytical Inc., Westborough, MA, USA) with Cu $K_\alpha$ radiation ($\lambda = 1.5418$ Å). Lattice parameters and average crystallite sizes were determined using the Rietveld method (RIQAS4, Materials Data Inc., Livermore, CA, USA). The reliability factors $R_p$ and $R_{wp}$ were calculated by Equations 3 and 4:

$$R_p = \frac{\sum_i |cY^{sim}(2\theta_i) - I^{exp}(2\theta_i) + Y^{back}(2\theta_i)|}{\sum_i |I^{exp}(2\theta_i)|} \tag{3}$$

$$R_{wp} = \left\{ \frac{[\sum_i w_i (cY^{sim}(2\theta_i) - I^{exp}(2\theta_i) + Y^{back}(2\theta_i))^2]}{\sum_i w_i (I^{exp}(2\theta_i))^2} \right\}^{1/2} \tag{4}$$

where $c$ is an optimized scaling factor that produces the lowest value of $R_{wp}$, $w_i = 1/I^{exp}(2\theta_i)$ is a weighting function, $I^{exp}(2\theta_i)$ is the angle-dependent intensity from an

experimental spectrum, $Y^{sim}(2\theta_i)$ is the simulated diffraction intensity without the background contribution, $Y^{back}(2\theta_i)$ is the background intensity of the measured spectrum[32]. Total oxygen contents were determined by gas-fusion analysis (Leco, Model TC500, St. Joseph, MI, USA). Transmission electron microscopy (TEM, Tecnai F-20, FEI, Hillsboro, OR, USA) was used to observe the structure of $ZrC_x$ grains using an accelerating voltage of 200 kV. To make TEM specimens, 3 wt% of synthesized powder was suspended in acetone under ultrasonic vibration for 30 minutes, and then dropped on a Cu TEM grid with a carbon film (Carbon Film only on 400 mesh, Copper, Beijing Zhongjingkeyi Technology Co., Ltd, Beijing, China). Selected area electron diffractions (SAED) was used to determine the crystal structures for phase composition analysis. Surface areas were measured by nitrogen absorption (NOVA 1000, Quantachrome, Boynton Beach, FL, USA) and BET analysis. Equivalent particle sizes were calculated by assuming spherical particles using Equation (5),

$$x = 6/S\rho \tag{5}$$

where $S$ is the specific surface area and $\rho$ is the true density of the powder. Neutron powder diffraction (NPD) was measured using a high-resolution powder diffractometer. Neutrons with a wavelength of $\lambda = 1.485$ Å were selected using a double-focusing Si (511) crystal monochromator. About 1.5 grams of powder was loaded into a vanadium cell which was held in an aluminum exchange gas can. Diffraction patterns were collected by a set of five linear position-sensitive detectors (LPSDs). Data was binned in 0.05° steps over the 20° angular range covered by each LPSD. Five detector arm positions achieved a total 2θ range from 4.45° to 104.4° with position counting for ~3.5

hours. Neutron diffraction patterns were analyzed by Rietveld refinement method using an open source code FULLPROF[33].

## 3. RESULT AND DISCUSSION

Reaction 1 produced $ZrC_x$ at temperature of 1300°C and higher for both starting $ZrH_2$:C $ZrH_2$:C ratios. Figure 1a shows the XRD patterns for powders produced using a starting $ZrH_2$:C ratio of 1:0.98, but patterns for powders produced from a starting $ZrH_2$:C ratio of 1:0.60 were similar (see Appendices). In both cases, $ZrC_x$, with the $Fm\bar{3}m$ crystal structure (JCPDF card 35-0784), was the only phase detected and no extra peaks were apparent. The peaks shifted to lower angles as the synthesis temperature increased

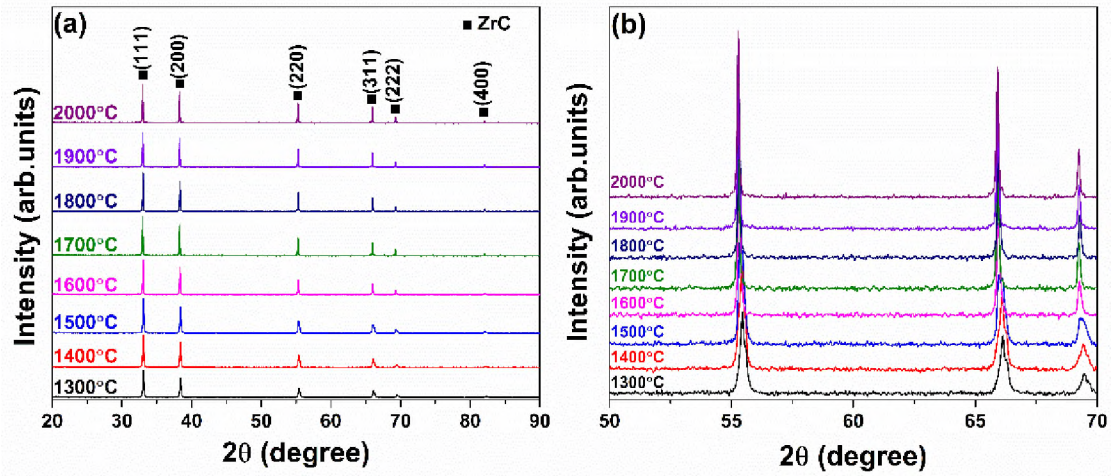


Figure 1. XRD patterns for $ZrC_x$ powders synthesized using a starting $ZrH_2$:C ratio of 1:0.98 after heating to different temperatures and indexed to the $Fm\bar{3}m$ crystal structure showing that: a) only $ZrC_x$ was detected, and b) peaks shifted to lower angles as synthesis temperature increased.

(Figure 1b) indicating that lattice parameters increased with increasing synthesis temperature. Based on the observations described above, $ZrC_x$ can be synthesized by solid state reaction of $ZrH_2$ and carbon black at temperature as low as 1300°C. Amorphous carbon was observed after the powder with a starting $ZrH_2$:C ratio of 1:0.98 was reacted at 1300°C. Figure 2a shows lighter regions that appear to be amorphous carbon along with darker grains that are $ZrC_x$. Increasing the synthesis temperature to 2000°C (Figure 2b) caused the excess carbon to disappear. No amorphous carbon was present when the starting

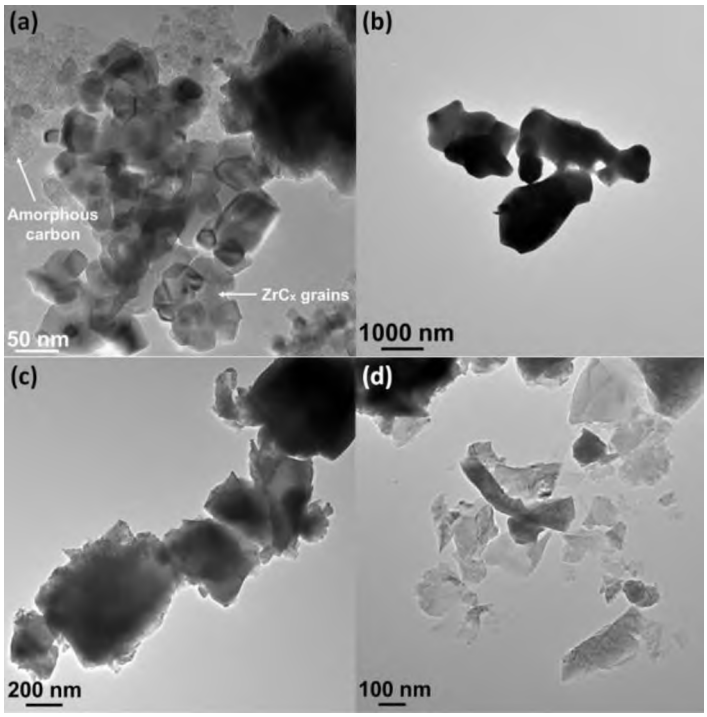


Figure 2. TEM micrographs for $ZrC_x$ powders synthesized using starting $ZrH_2$:C ratios of: (a)1:0.98 after heating to 1300°C; (b)1:0.98 after heating to 2000°C; (c)1:0.60 after heating to 1300°C; (d)1:0.60 after heating to 2000°C.

$ZrH_2$:C ratio was 1:0.60 (Figures 2c and 2d). The results indicated that $ZrC_x$ was carbon deficient after synthesis at 1300°C, even with sufficient carbon present to produce fully

stoichiometric $ZrC_{0.98}$. Excess carbon was not detected by XRD analysis for any combination of $ZrH_2$:C ratio and synthesis temperature. Hence, other reports of $ZrC_x$ synthesis from a starting Zr:C ratio of ~1 likely produce a combination of carbon-deficient $ZrC_x$ and excess amorphous carbon that goes undetected by XRD and other typical characterization methods.

The temperature at which excess carbon dissolved into the $ZrC_x$ lattice was determined by heating powder with a starting $ZrH_2$:C ratio of 1:0.98 to intermediate temperatures between 1300°C and 2000°C. Amorphous carbon was still observed around $ZrC_x$ grains after reaction at 1500°C (Figure 3a). However, no amorphous carbon was found in powders that were heated to 1600°C (Figure 3b). Hence, a synthesis temperature of at least 1600°C was needed to fully react Zr and C when present in a starting ratio of $ZrH_2$:C of 1:0.98.

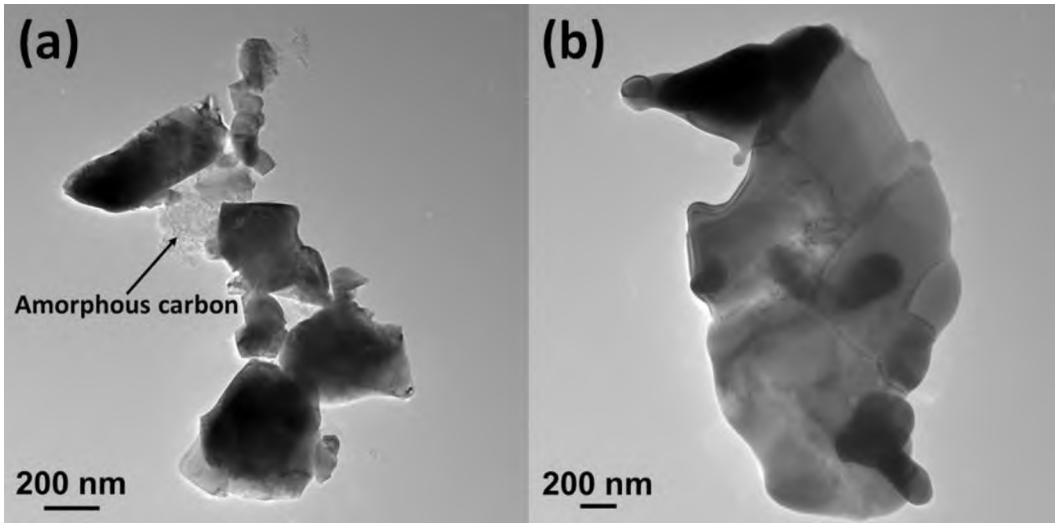


Figure 3. TEM micrographs for $ZrC_x$ powders synthesized using a starting $ZrH_2$ : C ratio of 1 : 0.98 after heating to (a) 1500°C, (b) 1600°C.

The synthesis temperature affected the lattice parameter of $ZrC_x$ powders. As can be seen in Figure 4, the lattice parameter of powders synthesized at temperatures below 1500°C increased with increasing synthesis temperature from 4.686 Å for synthesis at 1300°C to 4.699 Å for synthesis at 1500°C. The increase in lattice parameter could be due to the increasing carbon content in the $ZrC_x$ lattice in this temperature range based on the relationship reported by Jackson and Lee[34]. In contrast, the lattice parameter decreased in the next temperature regime from 4.699 Å at 1500°C to 4.694 Å 1700°C. In this regime, the decrease in lattice parameter was attributed to the loss of dissolved oxygen and/or

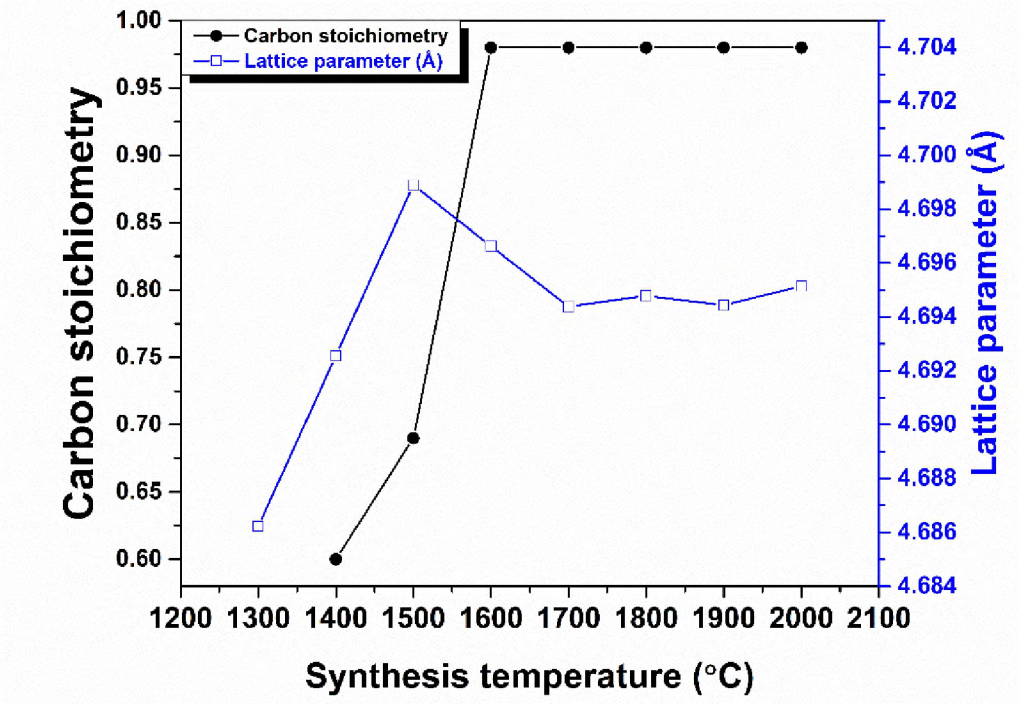


Figure 4. Lattice parameter and estimated carbon stoichiometry for $ZrC_x$ powders synthesized using a starting $ZrH_2$:C ratio of 1:0.98 that were heated to different temperatures. Note that error bars on the lattice parameters are smaller than the data points. The lines were added as guides.

lattice parameter was constant at ~4.694 Å, indicating that neither the carbon nitrogen from the $ZrC_x$ lattice[35]. Starting $ZrH_2$ powder include oxygen impurity, and both oxygen and nitrogen impurities exist in the flowing argon. At 1700°C and above, the stoichiometry nor the dissolved content of oxygen and/or nitrogen changed significantly in this temperature regime.

Changes in the lattice parameter indicated that the carbon content of $ZrC_x$ changed as synthesis temperature changed for powders synthesized using a starting $ZrH_2$:C ratio of 1:0.98. The correlation between lattice parameter and carbon content determined by Jackson and Lee[34] was used to estimate carbon content from lattice parameters determined by Rietveld refinement of XRD patterns. The lattice parameter after synthesis at 1300°C was ~4.686 Å, which would indicate a carbon content of less than $ZrC_{0.60}$ after reaction at this temperature. Since the minimum C content shown by most Zr-C phase diagrams is $x = 0.60$[36], the lattice parameter for this synthesis condition may have been affected by dissolved oxygen and/or nitrogen or by strain that was due to the fine crystallite size (discussed below). Hence, no estimate of carbon stoichiometry was made for powders synthesized at 1300°C by this method. The lattice parameter was 4.693Å after synthesis at 1400°C, which correlated to a carbon stoichiometry of $ZrC_{0.60}$. Likewise, the lattice parameter increased to 4.699 Å after synthesis at 1500°C, indicating a carbon stoichiometry of $ZrC_{0.69}$. At temperatures of 1600°C and higher, full carbon stoichiometry was assumed based on TEM observations discussed above wherein no excess carbon was present. Lattice parameters of those powders are in the range of 4.694 Å to 4.697 Å (see Appendices), which is slightly lower than the value of ~4.697 Å indicated by Jackson and Lee[34] for $ZrC_{0.98}$. The reduction in lattice parameter compared

to the fully stoichiometric value could be due to either a small fraction of carbon vacancies or residual dissolved oxygen and/or nitrogen in the lattice.

Crystallite size increased as synthesis temperature increased. As shown in Figure 5 for a starting $ZrH_2$:C ratio of 1:0.98, synthesis at low temperatures (1300°C and 1400°C) resulted in a crystallite size between 40 nm and 50 nm. At this size, the particles could have significant compressive strain, which could also affect the lattice parameter measurements. Rietveld refinement indicated residual strains of up to about 0.09% after synthesis at 1300°C (Table 1). Above 1400°C, crystallite size increased continuously with increasing

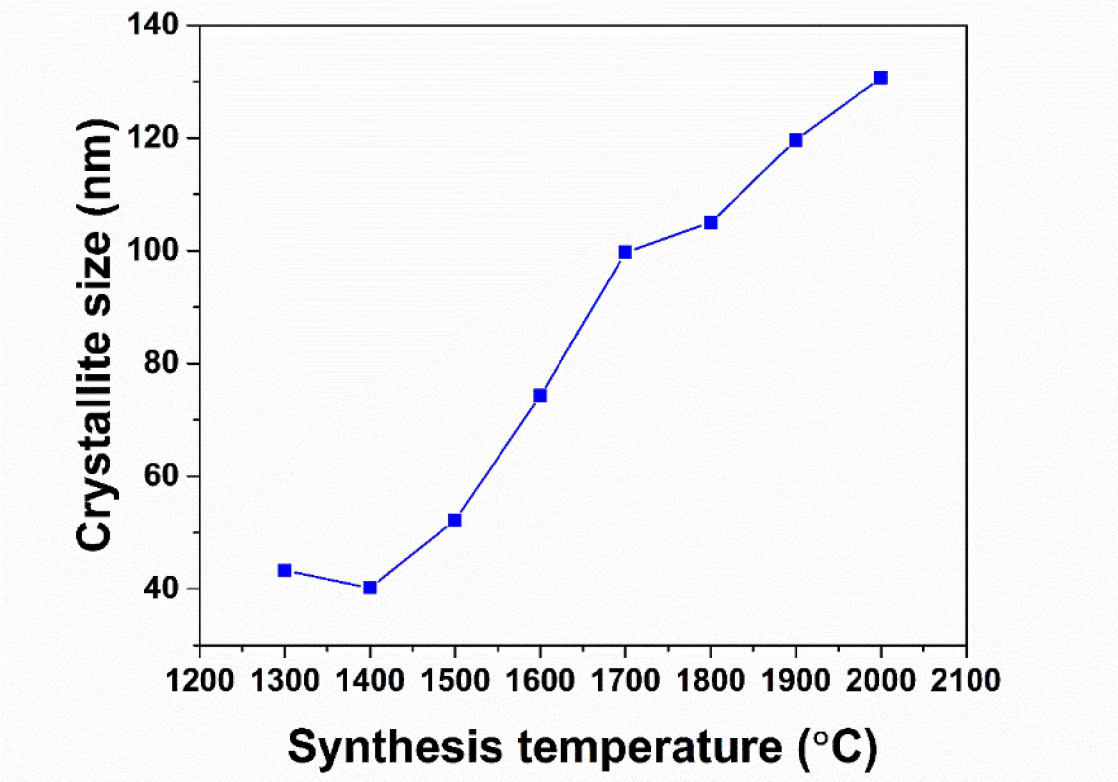


Figure 5. Crystallite sizes for $ZrC_x$ powder synthesized using a starting $ZrH_2$:C ratio of 1:0.98 heated to different temperatures.

synthesis temperature, reaching ~130 nm for a synthesis temperature of 2000°C. Representative morphologies of as-synthesized $ZrC_x$ powders were shown in Figures 2 and 3. For powders synthesized at temperatures of 1500°C and higher, crystallite sizes estimated by Rietveld method were smaller than observed by TEM. For example, Figure 6 shows a TEM micrograph for powder synthesized at 1600°C. Some of the crystallites

Table 1. Reliability factors of Rietveld refinement, lattice parameters, estimated carbon stoichiometry, crystallite sizes, surface areas, particle sizes, oxygen contents and C and O occupancies of $ZrC_x$ powders mixed using starting $ZrH_2$:C ratio of 1:0.6 and 1:0.98 and synthesized at 1300°C and 2000°C.

| **Synthesis temperature (°C)** / **Starting $ZrH_2$:C ratio** | | **1300** | **2000** |
|---|---|---|---|
| **1:0.6** | $R_p$ (%) | 5.77 | 5.28 |
| | $R_{wp}$ (%) | 4.98 | 4.77 |
| | Lattice parameter(Å) | 4.679 | 4.678 |
| | Strain | $2.50\times10^{-4}$ | $2.50\times10^{-5}$ |
| | Carbon stoichiometry | 0.6 | 0.6 |
| | Crystallite size (nm) | 81.6 | 108.0 |
| | Surface area $m^2/g$ | 0.795 | 0.636 |
| | Particle size (μm) | 1.138 | 1.422 |
| | Oxygen content (wt%) | 1.953 | 2.297 |
| | C occupancy | 0.60 | 0.60 |
| | O and N occupancy | 0.14 | 0.12 |
| **1:0.98** | $R_p$ (%) | 5.33 | 7.63 |
| | $R_{wp}$ (%) | 5.07 | 5.28 |
| | Lattice parameter(Å) | 4.682 | 4.695 |
| | Strain | $8.50\times10^{-4}$ | $1.25\times10^{-4}$ |
| | Carbon stoichiometry | N/A | 0.98 |
| | Crystallite size (nm) | 43.3 | 130.7 |
| | Surface area $m^2/g$ | 5.310 | 0.612 |
| | Particle size (μm) | 0.170 | 1.478 |
| | Oxygen content (wt%) | 1.997 | 1.011 |
| | C site occupancy | 0.82 | 0.98 |

appeared to be smaller than 100 nm, which is consistent with the size determined by Rietveld refinement of XRD data. However, most of the crystallites were larger than 200 nm. The apparent differences in crystallite size between values estimated from XRD and TEM may be due to the limited number of particles observed by TEM, the different shape of the crystals (i.e., not spherical), or the crystallite size distribution.

All of the synthesized powders contained oxygen impurities. Oxygen contents determined by gas fusion ranged from as high as 2.3 wt% for powder synthesized at 2000°C for a starting $ZrH_2$:C ratio of 1:0.60 to as low as 1.0 wt% for powder synthesized at 2000°C using a starting $ZrH_2$:C ratio of 1:0.98 (Table 1). High resolution TEM revealed that particles all had an exterior oxide layer that was typically about 5 nm thick

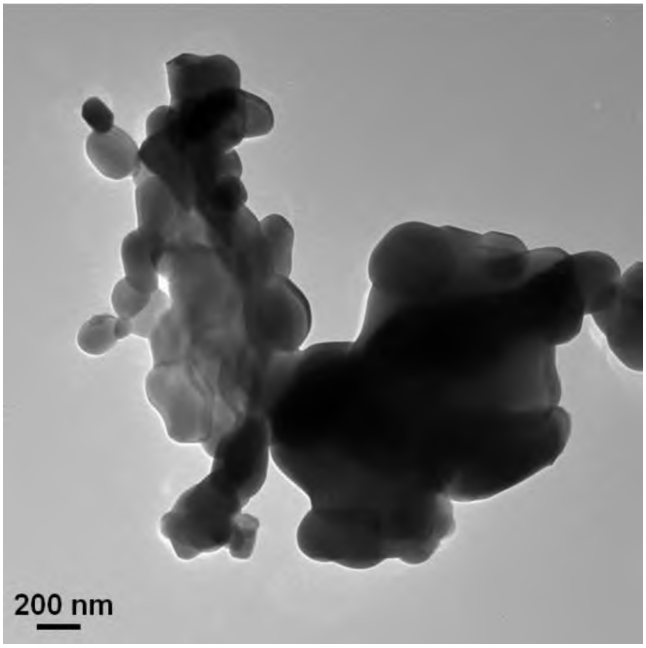


Figure 6. TEM micrographs for $ZrC_x$ powders synthesized using a starting $ZrH_2$ : C ratio of 1 : 0.98 after heating to 1600°C.

that accounted for at least some of the measured oxygen content (Figure 7). However, oxygen can also dissolve into the lattice and occupy carbon sites that would otherwise be vacant, so some of the measured oxygen content could be dissolved in the lattice. Likewise, nitrogen can dissolve into the lattice and occupy carbon vacancies.

Unfortunately, gas fusion analysis determines only total oxygen and nitrogen contents cannot distinguish between surface impurities and those on lattice sites. Based on this analysis, oxygen contents appear to decrease as carbon stoichiometry increases. The presence of dissolved oxygen also complicates determination of carbon stoichiometry from the lattice parameter of $ZrC_x$ since dissolved oxygen leads to a

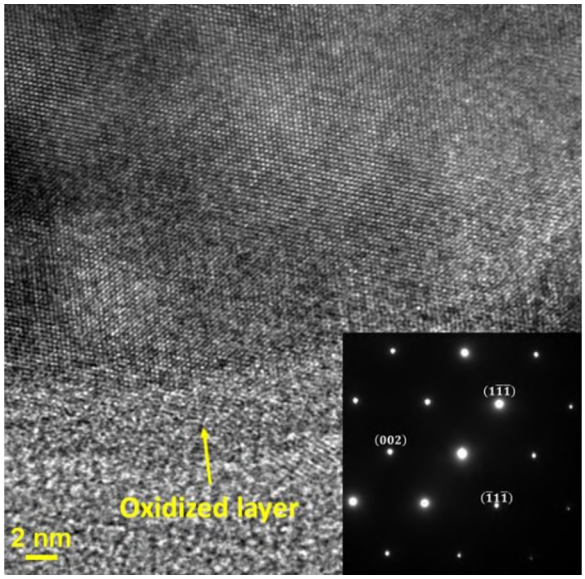


Figure 7. High resolution TEM micrographs of a $ZrC_x$ particle synthesized using a starting $ZrH_2$:C ratio of 1:0.98 after heating to 2000°C and an inset SAED pattern indexed to the $Fm\bar{3}m$ crystal structure.

decrease in lattice parameter compared to full occupancy of carbon lattice sites by carbon, but an increase in lattice parameter compared to the presence of vacancies.

Characterization methods typically used in studies of $ZrC_x$ synthesis are not able to unambiguously determine the fraction of vacant carbon sites or the number of lattice sites occupied by oxygen and/or nitrogen due to lack of sensitivity or convoluted effects[35][37]. For example, XRD patterns are dominated by scattering from the Zr sub-lattice due to its much higher x-ray scattering factor for Zr (40) compared to carbon (6), nitrogen (7), or carbon vacancies (0). As a result, analysis of peak intensity from XRD patterns does not provide enough information to independently determine carbon, oxygen, and nitrogen contents or site occupancies. In contrast, the neutron scattering factors for C (5.6 barn) and N (11.5 barn) are comparable to those of Zr (6.5 barn), which enables more accurate

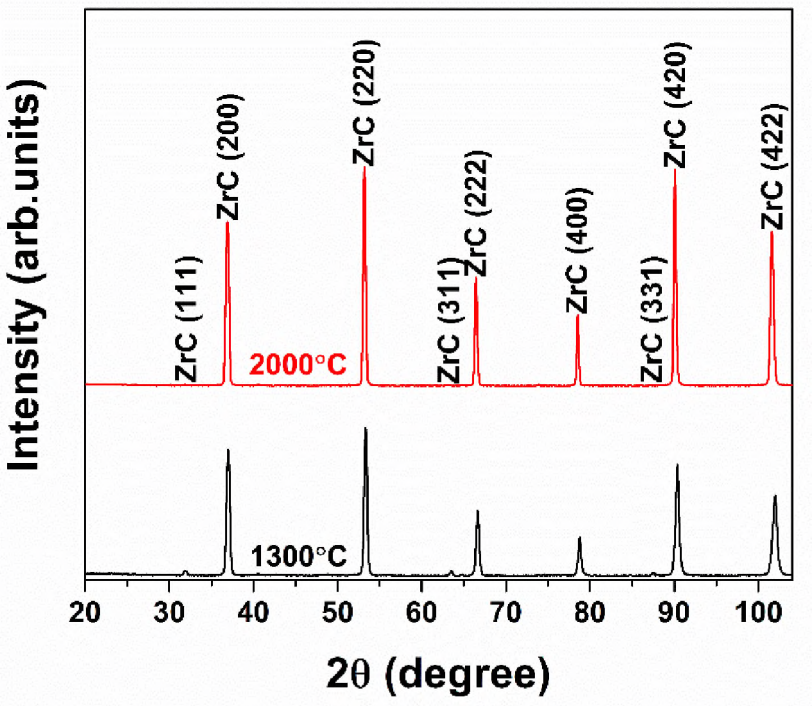


Figure 8. Neutron powder diffraction patterns for $ZrC_x$ powder synthesized using a starting $ZrH_2$:C ratio of 1:0.98 after heating to 1300°C and 2000°C.

refinement of peak intensity data and more reliable estimation of site occupancies from neutron powder diffraction patterns than is possible from XRD. Figure 8 shows neutron diffraction patterns for $ZrC_x$ powders synthesized using a starting $ZrH_2$:C ratio of 1:0.98 and heated to 1300°C and 2000°C. As with the XRD patterns, all of the peaks in both patterns were indexed to $ZrC_x$ with the $Fm\bar{3}m$ crystal structure (JCPDF card 35-0784).

Rietveld refinement was used to estimate the fraction of C sites occupied (Table 1). For this analysis, C sites were considered to either be occupied (i.e., contain a C, O, or N atom) or vacant without attempting to refine for each individual atom type. This analysis estimated that the fraction of C sites occupied after synthesis at 1300°C was 0.82. Increasing the synthesis temperature to 2000°C increased the C site occupancy to 0.98, which is consistent with observations by TEM that all of the initial carbon had been dissolved into the lattice (Figure 2b) as mentioned above. Based on this analysis and accepted Zr-C phase diagrams, full carbon stoichiometry was reached (i.e., $ZrC_{0.98}$ was formed). $ZrC_x$ synthesized using a starting $ZrH_2$:C ratio of 1:0.6 showed that the fraction of carbon sites occupied was about 0.60 regardless of the synthesis temperature (Table 1). All of the analysis performed as part of the present study indicates that neutron diffraction is a reliable method for determining occupancy of carbon sites in the $ZrC_x$ lattice.

## 4. CONCLUSION

Solid state reactions of $ZrH_2$ and carbon black were used to synthesize $ZrC_x$ powders. Different ratios of the reactants and different reaction temperatures were used to

study their effects on particle size and carbon stoichiometry. Single phase $ZrC_x$ was synthesized at temperatures as low as 1300°C. Below 1600°C, carbon was not fully incorporated into the $ZrC_x$ lattice. Observations by TEM indicated that all of the available carbon reacted with $ZrH_2$ at 1600°C and higher. Increasing the synthesis temperature increased the size of the resulting $ZrC_x$ crystallites from ~40 nm after reaction at 1300°C or 1400°C to ~130 nm after reaction at 2000°C. Oxygen impurities were present in all of the powders regardless of the starting $ZrH_2$:C ratio. Some of the oxygen was present as an oxide layer on the exterior of $ZrC_x$ particles, while the rest of the oxygen impurities were dissolved in the $ZrC_x$ lattice. Although XRD can confirm formation of the rock salt carbide structure, it was not able to determine carbon stoichiometry or dissolved oxygen content in transition metal carbides. Neutron diffraction was able to discern differences in site occupancy, showing that carbon stoichiometry increased and dissolved oxygen content decreased with increasing synthesis temperature.

## ACKNOWLEDGEMENT

This research was supported by the Ceramics program of the U.S. National Science Foundation as part of project DMR 1742086. The neutron powder diffraction measurements were made at The Missouri Research Reactor, University of Missouri.

## REFERENCES

[1] Sara RV. The system zirconium—carbon. J Amer Ceramic Soc. 1965;48(5):243-247. https://doi.org/10.1111/j.1151-2916.1965.tb14729.x.

[2] Pierson HO. Handbook of refractory carbides and nitrides: properties, characteristics, processing and applications. Norwich, NY: William Andrew; 1996.

[3] Grossman LN. High-Temperature Thermophysical Properties of Zirconium Carbide. J Amer Ceramic Soc. 1965;48(5):236-242. https://doi.org/10.1111/j.1151-2916.1965.tb14728.x.

[4] Katoh Y, Vasudevamurthy G, Nozawa T, Snead LL. Properties of zirconium carbide for nuclear fuel applications. J Nuclear Materials. 2013;441(1-3):718-742. https://doi.org/10.1016/j.jnucmat.2013.05.037.

[5] Shen X, Li K, Li H, Du H, Cao W, Lan F. Microstructure and ablation properties of zirconium carbide doped carbon/carbon composites. Carbon. 2010;48(2):344-351. https://doi.org/10.1016/j.carbon.2009.09.035.

[6] Taylor RE. Thermal conductivity of zirconium carbide at high temperatures. J Amer Ceramic Soc. 1962;45(7):353-354. https://doi.org/10.1111/j.1151-2916.1962.tb11166.x.

[7] Taylor RE, Morreale J. Thermal conductivity of titanium carbide, zirconium carbide, and titanium nitride at high temperatures. J Amer Ceramic Soc. 1964;47(2):69-73. https://doi.org/10.1111/j.1151-2916.1964.tb15657.x.

[8] Zhao D, Zhang C, Hu H, Zhang Y. Preparation and characterization of three-dimensional carbon fiber reinforced zirconium carbide composite by precursor infiltration and pyrolysis process. Ceramics International. 2011;37(7):2089-2093. https://doi.org/10.1016/j.ceramint.2011.02.024.

[9] Zhu Y, Wang S, Li W, Zhang S, Chen Z. Preparation of carbon fiber-reinforced zirconium carbide matrix composites by reactive melt infiltration at relative low temperature. Scripta Materialia. 2012;67(10):822-825. https://doi.org/10.1016/j.scriptamat.2012.07.044.

[10] Sabharwall P, Bragg-Sitton SM, Stoots C. Challenges in the development of high temperature reactors. Energy Conversion Mgmt. 2013;74:574-581. https://doi.org/10.1016/j.enconman.2013.02.021.

[11] Wang Y, Liu Q, Liu J, Zhang L, Cheng L. Deposition mechanism for chemical vapor deposition of zirconium carbide coatings. J Amer Ceramic Soc. 2008;91(4):1249-1252. https://doi.org/10.1111/j.1551-2916.2007.02253.x.

[12] Liu Q, Zhang L, Cheng L, Wang Y. Morphologies and growth mechanisms of zirconium carbide films by chemical vapor deposition. J Coatings Tech Res. 2009;6(2):269-273. https://doi.org/10.1007/s11998-008-9117-5.

[13] Barnier P, Brodhag C, Thevenot F. Hot-pressing kinetics of zirconium carbide. J Materials Science. 1986;21(7):2547-2552. https://doi.org/10.1007/BF01114305.

[14] Wei X, Back C, Izhvanov O, Haines CD, Olevsky EA. Zirconium carbide produced by spark plasma sintering and hot pressing: Densification kinetics, grain growth, and thermal properties. Materials. 2016;9(7):577. 10.3390/ma9070577.

[15] Tsuchida T, Kawaguchi M, Kodaira K. Synthesis of ZrC and ZrN in air from mechanically activated Zr-C powder mixtures. Solid State Ionics. 1997;101:149-154. https://doi.org/10.1016/S0167-2738(97)84023-4.

[16] Yen BK. X-ray diffraction study of mechanochemical synthesis and formation mechanisms of zirconium carbide and zirconium silicides. J Alloys Compounds. 1998;268:(1-2):266-269. https://doi.org/10.1016/S0925-8388(97)00581-1.

[17] Tsuchida T, Yamamoto S. Mechanical activation assisted self-propagating high-temperature synthesis of ZrC and ZrB2 in air from Zr/B/C powder mixtures. J Euro Ceramic Society. 2004;24(1):45-51. https://doi.org/10.1016/S0955-2219(03)00120-1.

[18] Song MS, Huang B, Zhang MX, Li JG. Formation and growth mechanism of ZrC hexagonal platelets synthesized by self-propagating reaction. J Crystal Growth. 2008;310(18):4290-4294. https://doi.org/10.1016/j.jcrysgro.2008.07.016.

[19] Sacks MD, Wang CA, Yang Z, Jain A. Carbothermal reduction synthesis of nanocrystalline zirconium carbide and hafnium carbide powders using solution-derived precursors. J Materials Science 2004;39(19):6057-6066. https://doi.org/10.1023/B:JMSC.0000041702.76858.a7.

[20] Dolle M, Gosset D, Bogicevic C, Karolak F, Simeone D, Baldinozzi G. Synthesis of nanosized zirconium carbide by a sol–gel route. J Euro Ceramic Society. 2007;27(4):2061-2067. https://doi.org/10.1016/j.jeurceramsoc.2006.06.005.

[21] Ding J, Guo D, Deng C, Zhu H, Yu C. Low-temperature synthesis of nanocrystalline ZrC coatings on flake graphite by molten salts. Applied Surface Science. 2017;407:315-321. https://doi.org/10.1016/j.apsusc.2017.02.196.

[22] Dai L, Wang X, Zhou H, Yu Y, Zhu J, Li Y et al. Direct electrochemical synthesis of zirconium carbide from zirconia/C precursors in molten calcium chloride. Ceramics International. 2015;41(3):4182-4188. https://doi.org/10.1016/j.ceramint.2014.12.101.

[23] Leconte Y, Maskrot H, Combemale L, Herlin-Boime N, Reynaud C. Application of the laser pyrolysis to the synthesis of SiC, TiC and ZrC pre-ceramics nanopowders. J Anal Appl Pyrolysis. 2007;79(1-2):465-470. https://doi.org/10.1016/j.jaap.2006.11.009.

[24] Combemale L ,Leconte Y, Portier X, Herlin-Boime N, Reynaud C. Synthesis of nanosized zirconium carbide by laser pyrolysis route. J Alloys Compounds. 2009;483(1-2):468-472. https://doi.org/10.1016/j.jallcom.2008.07.159.

[25] Matteazzi P, Le Caër G. Room-Temperature Mechanosynthesis of Carbides by Grinding of Elemental Powders. J Amer Ceramic Soc. 1991;74(6):1382-1390. https://doi.org/10.1111/j.1151-2916.1991.tb04116.x.

[26] Song M, Huang B, Zhang M, Li J. Formation and growth mechanism of ZrC hexagonal platelets synthesized by self-propagating reaction. J Crystal Growth. 2008;310(18):4290-4294. https://doi.org/10.1016/j.jcrysgro.2008.07.016.

[27] Wang L, Si L, Zhu Y, Qian Y. Solid-state reaction synthesis of ZrC from zirconium oxide at low temperature. Int J Refract Met H. 2013;38:134-136. https://doi.org/10.1016/j.ijrmhm.2012.12.001.

[28] Gendre M, Maître A, Trolliard G. Synthesis of zirconium oxycarbide (ZrCxOy) powders: Influence of stoichiometry on densification kinetics during spark plasma sintering and on mechanical properties. J Euro Ceramic Society. 2011;31(13):2377-2385. https://doi.org/10.1016/j.jeurceramsoc.2011.05.037.

[29] Bokhonov BB, Dudina DV. Synthesis of ZrC and HfC nanoparticles encapsulated in graphitic shells from mechanically milled Zr-C and Hf-C powder mixtures. Ceramics International. 2017;43(16):14529-14532. https://doi.org/10.1016/j.ceramint.2017.07.164.

[30] David J, Trolliard G, Gendre M. TEM study of the reaction mechanisms involved in the carbothermal reduction of zirconia. J Euro Ceramic Society. 2013;33(1):165-179. https://doi.org/10.1016/j.jeurceramsoc.2012.07.024.

[31] Mitrokhin VA, Lyutikov RA, Yurkova RS. Change in the lattice constant of zirconium carbide in the region of homogeneity. Inorg. Mater. 1975;11(6):978-980.

[32] Vitalij KP, Peter YZ. Fundamentals of Powder Diffraction and Structural Characterization of Materials. 2nded. New York, NY: Springer; 2009.

[33] J. Rodriguez-Carvajal, FULLPROF version July-2017, ILL.

[34] Jackson HF, Lee WE. Properties and characteristics of ZrC. In: Konings RJM, eds. Volume 2 in Comprehensive Nuclear Materials. Amsterdam, Netherland: Elsevier; 2012:339-372.

[35] Harrison RW, Lee WE. Processing and properties of ZrC, ZrN and ZrCN ceramics: a review. Adv in Applied Ceramics. 2016;115(5):294-307. https://doi.org/10.1179/1743676115Y.0000000061.

[36] Diagram 8963 in Phase Diagrams for Ceramists Volume X: Borides, Carbides, and Nitrides. McHale AE ed. Westerville, OH: American Ceramic Society. 1994.

[37] Sarkar SK, Miller AD, Mueller JI. Solubility of oxygen in ZrC. J Amer Ceramic Soc. 1972;55(12):628-630. https://doi.org/10.1111/j.1151-2916.1972.tb13457.x.

# II. CARBON VACANCY ORDERING IN ZIRCONIUM CARBIDE POWDER

Yue Zhou [a], Thomas W. Heitmann [b], Eric Bohannan [a], Joseph C. Schaeperkoetter [c], William G. Fahrenholtz [a], Gregory E. Hilmas [a]

[a] *Department of Materials Science and Engineering, Missouri University of Science and Technology, Rolla, MO 65409, USA*

[b] *The Missouri Research Reactor, University of Missouri, Columbia, MO 65211, USA*

[c] *Department of Physic and Astronomy, University of Missouri, Columbia, MO 65211, USA*

## ABSTRACT

Ordered carbon vacancies were detected in zirconium carbide ($ZrC_x$) powders that were synthesized by direct reaction. Zirconium hydride ($ZrH_2$) and carbon black were used as starting powders with the molar ratio of $ZrH_2$:C=1:0.6. Powders were reacted at 1300°C or 2000°C. The major phase detected by x-ray diffraction was $ZrC_x$. No excess carbon was observed by transmission electron microscopy in powders synthesized at either temperature. Ordering of the carbon vacancies was identified by neutron powder diffraction and further supported by selected area electron diffraction. The vacancies in carbon-deficient $ZrC_x$ exhibited diamond cubic symmetry with a supercell that consisted of eight (2x2x2) $ZrC_x$ unit cells with the rock salt structure. Rietveld refinement of the neutron diffraction patterns revealed that the synthesis temperature did not have a significant effect on the degree of vacancy ordering in $ZrC_x$ powders. Direct synthesis of $ZrC_{0.6}$ resulted in the partial ordering of carbon vacancies without the need for extended isothermal annealing as reported in previous experimental studies

***Keywords:*** zirconium carbide; neutron diffraction; vacancies; non-stoichiometry; vacancy ordering.

## 1. INTRODUCTION

Zirconium carbide ($ZrC_x$) is one of the transition metal monocarbides (TMCs) that are part of the family of ultra-high temperature ceramics (UHTCs)[1]. Zirconium carbide has the rock salt crystal structure, but is typically carbon-deficient compared to the ideal one-to-one metal to carbon stoichiometric ratio. Experimental phase diagrams for the Zr-C show that $ZrC_x$ is stable for x values ranging from 0.63 to 0.98[2]. Similarly, variable carbon stoichiometry is exhibited by other TMCs, such as $TiC_x$[3][4][5], $HfC_x$[6][7], $VC_x$[8], $NbC_x$[3][9], $TaC_x$[10][11] and $WC_x$[12]. Carbon stoichiometry affects the sinterability[13][14][15], mechanical properties[16][17], electrical properties[18] and radiation resistance[19] of $ZrC_x$ ceramics. Short- and long-range ordering of carbon vacancies in non-stoichiometric carbides have both been studied theoretically[20][21][22]. For example, a $Zr_2C$ superstructure with ordered carbon vacancies was predicted in a computational study of the Zr-C phase diagram[23]. Also, $ZrC_x$ with ordered carbon vacancies has been reported in several experimental studies. Carbon vacancy ordered $ZrC_{0.61}$ was prepared by spark plasma sintering (SPS) after mechanochemical powder synthesis[24]. In another study, a superlattice was identified using a combination of electrical resistivity, differential thermal analysis, and x-ray diffraction measurements on a specimen of $ZrC_{0.7}$ that was prepared by arc-melting and annealing[25]. Crystal structures of non-stoichiometric $ZrC_x$ have also been studied by computational methods, which predicted the stability of the

$Fd\bar{3}m$ crystal structure at carbon stoichiometries as low as x=0.5 using mixing enthalpy calculations[26]. Phase stability of highly carbon deficient compositions (e.g., $x \leq 0.5$) has been studied using formation enthalpy calculations, which showed that the $Fd\bar{3}m$ structure, with ordered vacancies, was the most stable[27]. However, not all of the carbides with the rock-salt crystal structure have the same characteristic as $ZrC_X$. Micro-scale inhomogeneities were detected in the structures of $NbC_X$ and $VC_X$ powders that prepared by high-energy ball milling of the coarse-grained synthesized powders[28][29][30]. A lower carbon content was detected for a small grain size while a higher carbon content was detected for a large grain size by neutron diffraction analysis. Similarly, microscale stoichiometry variations have been identified in both experimental and theoretical studies of other compounds with the rock salt crystal structure including transition-metal monoxides[31][32][33] and PbS[34][35].

The purpose of the present study was to quantify carbon vacancy ordering in $ZrC_X$ powders synthesized by direct reaction of $ZrH_2$ and C with x=0.6.

## 2. EXPERIMENTAL

The starting materials for $ZrC_{0.6}$ synthesis were commercial $ZrH_2$ (Min. 95.5%, 27.1 μm, Chemadyne, LLC., Canoga Park, CA, USA) and carbon black (BP-1100, Cabot Corporation, Alpharetta, GA, USA). The starting powders were batched with a $ZrH_2$:C molar ratio of 1:0.6. Powders were mixed by ball milling using zirconia grinding media in acetone for 12 hours under a rotation speed of 50 rpm. Rotary evaporation (Rotavapor R-124, Bucchi, Flawil, Germany) was used to remove the acetone from the slurry using a

temperature of 80°C, rotation speed of 90 rpm and vacuum of 33.3 kPa (250 mmHg). Three grams of the dried powder was uniaxially pressed under a pressure of 44 MPa to produce cylindrical pellets for synthesis.

Synthesis by Reaction 1 was conducted in a graphite element furnace (3060-FP20, Thermal Technology, Santa Rosa, CA, USA) under flowing argon. The raw powder was heated at 10°C/min from room temperature to 800°C where it was held for 2 hours to promote decomposition of $ZrH_2$. Formation of $ZrC_x$ was promoted by heating at 10°C/min to temperatures of 1300°C or 2000°C with holding time of 3 hours. For synthesis at 2000°C, the furnace was cooled at 50°C/min from the maximum holding temperature to ~1450°C. Below that temperature and for the powder synthesized at 1300°C, the furnace power was shut off and the furnace cooled at its natural rate, which was an average of ~18°C/min between ~1300°C and room temperature.

$$ZrH_{2(s)} + 0.6C_{(s)} \rightarrow ZrC_{0.6(s)} + H_{2(g)} \quad (1)$$

Powder X-ray diffraction (XRD, PANalytical X'Pert3 Powder, Malvern Panalytical Inc., Westborough, MA, USA) with Cu $K_\alpha$ radiation ($\lambda = 1.5418$ Å) was employed for phase identification. The step size was 0.025°, and each step was counted for the equivalent of 75 s using an area detector (PIXCel detector, Malvern Panalytical Inc., Westborough, MA, USA). Rietveld refinement (RIQAS4, Materials Data Inc., Livermore, CA, USA) was used to determine the lattice parameter and average crystallite size of each powder. A high-resolution powder diffractometer was used for neutron powder diffraction (NPD) measurements. Neutrons with a wavelength of $\lambda = 1.485$ Å were selected by a double-focusing Si (511) crystal monochromator. Approximately 1.5 g of the synthesized powder was loaded into a vanadium cell, which was held in an

aluminum exchange gas can. A set of five linear position-sensitive detectors (LPSDs) was employed to collect the diffraction patterns. Data was binned in 0.05° steps over the 20° angular range covered by each LPSD. Five detector arm positions achieved a total 2θ range from 4.45° to 104.4°. Each position underwent counting for ~3.5 hours. An open source code FULLPROF[36] was used to analyze the NPD patterns by the Rietveld method. Additional phase quantification was performed by the Rietveld method using commercial software (RIQAS4, Materials Data Inc., Livermore, CA, USA). A $Zr_2C$ crystal structure simulated in a previous first-principles study[37] was used as control model for analyzing. The peak intensities, peak broadening, and the corresponding C site occupancies were allowed to vary for the simulations. For observation of $ZrC_{0.6}$ powder morphology, transmission electron microscopy (TEM, Tecnai F-20, FEI, Hillsboro, OR, USA) was employed using an accelerating voltage of 200 kV. Selected area electron diffraction (SAED) was used to investigate the crystal structure of the synthesized powders. To prepare the TEM specimens, 3 wt% of powder was suspended in acetone under ultrasonic vibration for 30 minutes, and then dropped onto a Cu TEM grid with a carbon film (Carbon Film only on 400 mesh, Copper, Beijing Zhongjingkeyi Technology Co., Ltd, Beijing).

## 3. RESULTS AND DISCUSSION

Zirconium carbide formed at temperatures as low as 1300°C as described previously[38]. Figure 1 shows the XRD patterns and Table 1 shows the detailed peak indexing for powders synthesized using a starting $ZrH_2$:C ratio of 1:0.6 heated to 1300°C

and 2000°C. $ZrC_x$ with the $Fm\bar{3}m$ crystal structure (ICDD PDF card 35-0784) was the major phase detected in the powder heated to 1300°C, along with a minor amount of residual Zr (ICDD PDF card 01-1147). The only phase in the powder heated to 2000°C was $ZrC_x$ with all of the peaks indexed to ICDD PDF card 35-0784. While XRD was able to identify the formation of $ZrC_x$, it was not able to provide information about carbon site occupancy or carbon stoichiometry due to the low x-ray scattering cross section of carbon (6), nitrogen (7), and oxygen (8) compared to zirconium (40).

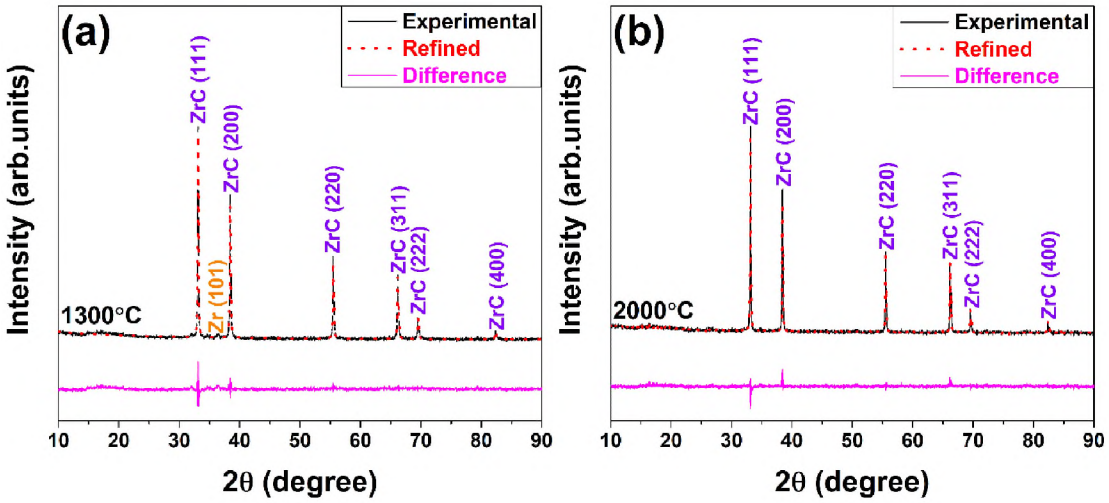


Figure 1. XRD pattern for $ZrC_{0.6}$ powder synthesized using a starting $ZrH_2$:C ratio of 1:0.6 heating to (a) 1300°C and (b) 2000°C. Patterns were collected with Cu $K_\alpha$ radiation ($\lambda = 1.5418$ Å).

The lattice parameter for $ZrC_x$ was determined to be 4.67928 (±0.00003) Å after heating to 1300°C and 4.67749 (±0.00003) Å after heating to 2000°C. The reliability factors were $R_p = 5.52\%$ and $R_{wp} = 4.94\%$ for the powder heated to 1300°C, and $R_p = 5.61\%$ and $R_{wp} = 4.83\%$ for the powder heated to 2000°C. Based only on the lattice parameter alone, the carbon stoichiometry of these powders would be expected to be less than x =

0.6[39]. However, the $ZrC_x$ lattice parameter is affected by other factors such as crystallite size, strain, and partial occupancy of C vacancies by dissolved species such as O or N, meaning that XRD is not a definitive tool for determining C stoichiometry. The slight decrease in lattice parameter with increasing synthesis temperature was likely due to removal of O or N from the $ZrC_x$ lattice or slight changes in C stoichiometry[40][41]. Overall, the lattice parameters are consistent with carbon-deficient $ZrC_x$.

Table 1. Peak positions, d-spacings and the Miller indices of the peaks in the X-ray diffraction patterns ($\lambda = 1.5418$ Å) for $ZrC_x$ synthesized at 1300°C and 2000°C. (*Residual Zr was present in the powder synthesized at 1300°C.)

| Synthesis temperature (°C) | Peak position (2θ) | D-spacing (Å) | Miller indices |
|---|---|---|---|
| **1300** | 33.096 | 2.705 | 111 |
| | *36.443** | *2.463** | *101** |
| | 38.922 | 2.342 | 200 |
| | 55.479 | 1.655 | 220 |
| | 66.164 | 1.411 | 311 |
| | 69.509 | 1.351 | 222 |
| | 82.342 | 1.170 | 400 |
| **2000** | 33.107 | 2.704 | 111 |
| | 38.411 | 2.342 | 200 |
| | 55.508 | 1.654 | 220 |
| | 66.196 | 1.411 | 311 |
| | 69.547 | 1.351 | 222 |
| | 82.376 | 1.170 | 400 |

TEM observations were used to evaluate the morphology of the $ZrC_x$ powders (Figure 2). No excess carbon was observed in either powder, indicating that most, or all, of the carbon was reacted. However, residual Zr was detected by XRD in the powder synthesized at 1300°C (Figure 1), indicating that either a small fraction of carbon black had likely not reacted with zirconium at that synthesis temperature or some of the $ZrC_x$

that formed had a carbon content higher than $ZrC_{0.6}$. The crystallite size of the powders varied significantly from ~50 nm to more than 1000 nm in diameter. In addition, the particles were agglomerated[42].

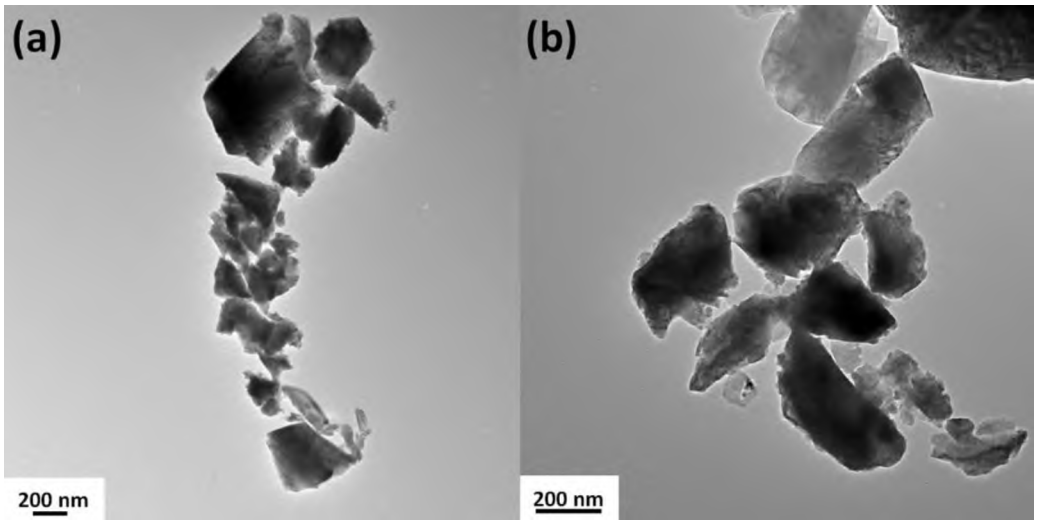


Figure 2. TEM micrographs for $ZrC_{0.6}$ powders synthesized at (a) 1300°C and (b) 2000°C. Magnification varies between the two images.

Neutron powder diffraction was used to further characterize the $ZrC_{0.6}$ powders (Figure 3). Initial analysis showed that the patterns could be indexed to the same $ZrC_x$ structure as the XRD patterns. The d-spacings of peaks that index to the rock salt structure of $ZrC_x$ ($Fm\bar{3}m$ crystal structure, ICDD PDF card 35-0784) are labeled on the image. However, a number of additional peaks were apparent from NPD that were not detected by XRD. These peaks could not be indexed to $ZrC_x$ with the $Fm\bar{3}m$ crystal structure (ICDD PDF card 35-0784). Previous studies that employed first-principles calculations concluded that the lowest energy structure had vacancies ordered on a scale longer than the $ZrC_x$ unit cell, which was described as $Zr_2C$ ($Fd\bar{3}m$, No. 227) with

vacancies having diamond cubic symmetry and a lattice parameter twice that of $ZrC_x$[37]. Building on that knowledge, the peaks from the neutron diffraction patterns were indexed to the carbon vacancy ordered $ZrC_x$ superlattice as shown in Table 2 and Table 3. For instance, for the powder synthesized at 2000°C, the peaks located at 2θ = 15.771°, 30.555°, 31.937°, 37.046° and 40.551° corresponded to the (111), (311), (222), (400) and (331) planes of $Zr_2C$ (Table 3). Based on this assessment, at least some of the vacancies in carbon-deficient $ZrC_x$ appear to be ordered. Further, Rietveld refinement is consistent with vacancy ordering in a unit cell that has a lattice parameter that is twice as large as $ZrC_x$. Additional NPD experiments (not shown) did not reveal any lower angle peaks that would indicate ordering at even longer length scales.

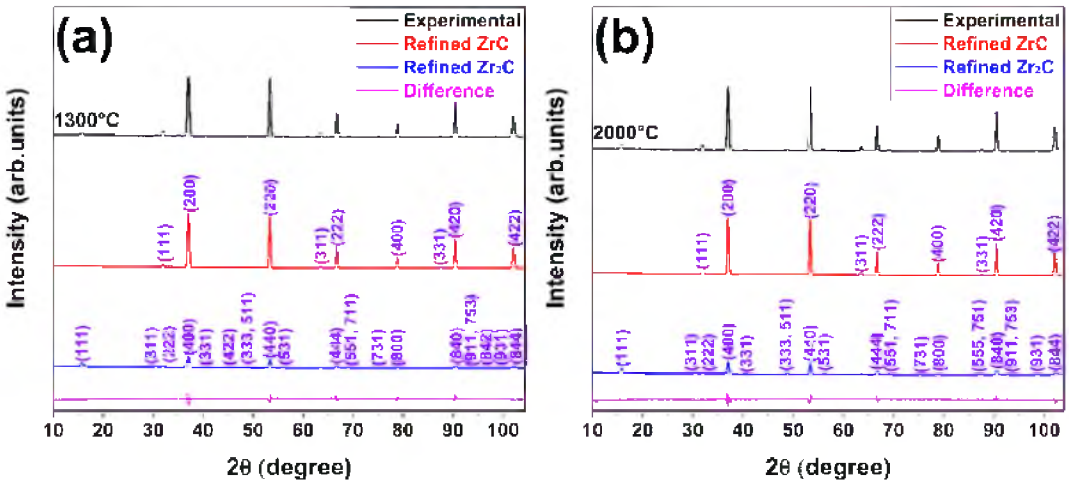


Figure 3. Neutron powder diffraction patterns for $ZrC_{0.6}$ powder synthesized using a starting $ZrH_2$:C ratio of 1:0.6 after heating to (a) 1300°C and (b) 2000°C (λ = 1.485 Å). Miller indices of the $ZrC_x$ rock-salt structure and superlattice were labeled.

Rietveld refinement of neutron diffraction data was also used to determine site occupancies in the $ZrC_x$ superlattice. Dissolved O and N occupied 14% of the C sites in

the powder synthesized at 1300°C and 12% in the powder synthesized at 2000°C, which was estimated using Rietveld analysis of neutron powder diffraction patterns with the assumption that the carbon stoichiometry x = 0.6 as set by the nominal powder batching [38]. Based on this analysis, more than 25% of the carbon sites were vacant. The $\chi^2$-factor

Table 2. Peak positions, d-spacings, and Miller indices of the peaks in the neutron diffraction pattern ($\lambda = 1.485$ Å) for $ZrC_x$ synthesized at 1300°C.

| **Peak position (2θ, °)** | **D-spacing (Å)** | **Miller indices for $ZrC_{0.6}$ unit cell** | **Miller indices for $ZrC_{0.6}$ 2×2×2 supercell** | **Miller indices for Zr** |
|---|---|---|---|---|
| 15.786 | 5.407 | | 111 | |
| 30.582 | 2.815 | | 311 | |
| 31.931 | 2.699 | 111 | 222 | |
| 33.492 | 2.577 | | | 002 |
| 35.160 | 2.458 | | | 101 |
| 37.036 | 2.338 | 200 | 400 | |
| 40.557 | 2.142 | | 331 | |
| 46.085 | 1.897 | | 422 | |
| 48.750 | 1.799 | | 333, 511 | |
| 53.386 | 1.653 | 220 | 440 | |
| 56.035 | 1.581 | | 531 | |
| 60.919 | 1.465 | | | 103 |
| 63.551 | 1.410 | 311 | | |
| 66.714 | 1.350 | 222 | 444 | |
| 69.086 | 1.309 | | 551,711 | |
| 75.173 | 1.217 | | 731 | |
| 78.869 | 1.169 | 400 | 800 | |
| 87.560 | 1.073 | 331 | | |
| 90.476 | 1.046 | 420 | 840 | |
| 92.622 | 1.027 | | 911,753 | |
| 94.950 | 1.007 | | 842 | |
| 98.484 | 0.980 | | 931 | |
| 102.103 | 0.955 | 422 | 844 | |

values of the fittings are 9.7 for the powder synthesized at 1300°C and 12.7 for the powder synthesized at 2000°C.

The SAED patterns were also consistent with the ordering of carbon vacancies at length scales longer than the $ZrC_x$ unit cell. Figure 4 shows a high resolution TEM micrograph of $ZrC_x$ powder synthesized at 2000°C with the corresponding SAED along the [110] zone axis. Fundamental peaks appeared as the larger spots and were due to the rock-salt structure of the $ZrC_x$ unit cell. Superlattice peaks can be seen between the transmission spot and the family of {111} planes, which are consistent with supercell having cubic symmetry, but with a lattice parameter two times that of the $ZrC_x$ unit cell.

Table 3. Peak positions, d-spacings and the Miller indices of the peaks in the neutron diffraction pattern ($\lambda = 1.485$ Å) for $ZrC_x$ synthesized at 2000°C.

| **Peak position (2θ, °)** | **D-spacing (Å)** | **Miller indices for $ZrC_{0.6}$ unit cell** | **Miller indices for $ZrC_{0.6}$ 2×2×2 supercell** | **Miller indices for graphite** |
|---|---|---|---|---|
| 15.771 | 5.412 | | 111 | |
| 25.667 | 3.343 | | | 002 |
| 30.555 | 2.818 | | 311 | |
| 31.937 | 2.699 | 111 | 222 | |
| 37.046 | 2.337 | 200 | 400 | |
| 40.551 | 2.143 | | 331 | |
| 48.748 | 1.799 | | 333,511 | |
| 53.411 | 1.652 | 220 | 440 | |
| 56.054 | 1.580 | | 531 | |
| 63.572 | 1.410 | 311 | | |
| 66.752 | 1.350 | 222 | 444 | |
| 69.104 | 1.309 | | 551,711 | |
| 75.185 | 1.217 | | 731 | |
| 78.911 | 1.168 | 400 | 800 | |
| 86.886 | 1.080 | | 555,751 | |
| 87.630 | 1.072 | 331 | | |
| 90.520 | 1.045 | 420 | 840 | |
| 92.690 | 1.026 | | 911,753 | |
| 98.518 | 0.980 | | 931 | |
| 102.161 | 0.954 | 422 | 844 | |

The SAED pattern of the powder synthesized at 1300°C (not shown) was similar to the one synthesized at 2000°C. These results are consistent with carbon vacancy ordering in both of the as-synthesized $ZrC_x$ powders. Further, the vacancies were ordered on a length scale that appears to be a superlattice consisting of eight $ZrC_x$ unit cells in a 2 by 2 by 2 array.

Additional Rietveld refinements of NPD patterns were used to quantify the degree of ordering of the carbon vacancies in $ZrC_x$. Crystal structures predicted by first principles studies for zirconium carbide with full carbon site occupancy (ZrC) and the lowest carbon site occupancy (called $Zr_2C$ in simulation studies) were used as control models for the simulations[37]. One output of these simulations was the average C site

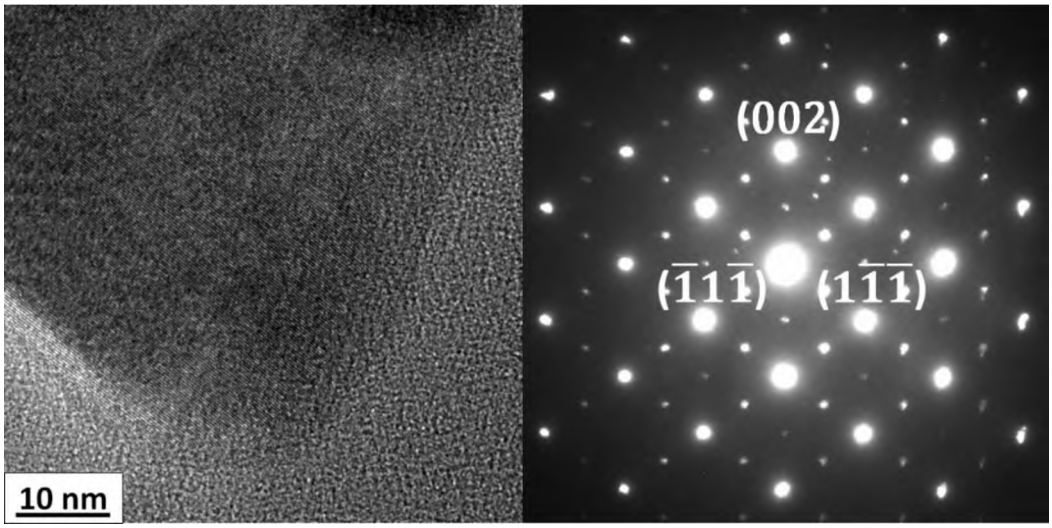


Figure 4. High resolution TEM micrographs and selected area electron diffraction of $ZrC_{0.6}$ powders synthesized at 2000°C.

occupancies for the different synthesis temperatures (Table 4). Average C site occupancies for the overall compositions were higher than 0.6 for both powders due to partial site occupancy by O or N in addition to C.

The additional Rietveld simulations also quantified the relative amounts of $ZrC_x$ with random vacancies (denoted $ZrC_x$) and ordered vacancies (denoted $Zr_2C$). Based on the simulations, ~25 wt% of the powder synthesized at 1300°C and ~23 wt% of the powder synthesized at 2000°C consisted of the carbon vacancy ordered phase $Zr_2C$. The reliability factors of the NPD pattern refinement, $R_{wp}$, were 8.74% and 8.50% for the powders synthesized at 1300°C and 2000°C, respectively. The balance of both powders (~75 wt% of the powder synthesized at 1300°C and ~77 wt% of the powder synthesized at 2000°C) had disordered vacancies. Based on this analysis, vacancies were only partially ordered in $ZrC_x$ and synthesis temperature did not have a significant effect on ordering of vacancies in $ZrC_x$ powders. In a multi-phase sample, each phase contributes to the intensity of the NPD peaks[43]. Some parent peaks (Figure 3) are overlapped (e.g., the (222) peak in $Zr_2C$ and the (111) peak in $ZrC_x$), which adds uncertainty to the phase quantification. However, the analysis indicates that the carbon vacancies were partially ordered in the $ZrC_{0.6}$ powders synthesized in the present study.

The observation that the relative amounts of ordered vacancies were present in powders synthesized at different temperatures has two important implications on the results. The phase diagram calculated by Gusev[21] shows that ordering only occurs below the order-disorder transformation temperature of about 900°C. Hence, the first implication is that carbon vacancies should be random at both synthesis temperatures and should only order after synthesis when the powders cool to the order-disorder transition

temperature. Other studies typically report that forming ordered vacancies requires annealing for extended times below the order-disorder transition temperature. Those studies predominantly use powders prepared by carbothermal reduction. The second implication is that the direct synthesis method used in the present study may have enabled vacancy ordering without annealing, but further research is needed to determine the effects that cooling rate and oxygen content have on vacancy ordering.

## 4. CONCLUSION

The ordering of vacancies in carbon-deficient $ZrC_x$ powders was studied. The major phase detected by XRD in the powder heated to 1300°C was $ZrC_x$ with a minor amount of residual Zr while only $ZrC_x$ was detected in the powder synthesized at 2000°C. Neutron diffraction analysis revealed additional peaks that could not be indexed to the rock salt structure of $ZrC_x$. Both neutron diffraction and SAED were consistent with the presence of a superlattice with ordered carbon vacancies. The degree of vacancy ordering was estimated to be between 20% and 25% in powders synthesized at 1300°C and 2000°C, which indicates that synthesis temperature did not have a significant effect on vacancy ordering. These results indicate that $ZrC_x$ with partially ordered vacancies can be synthesized by direct reaction of Zr and C without the need for extended isothermal holds.

## ACKNOWLEDGEMENT

The current research was supported by the Ceramics Program in the U.S. National Science Foundation (DMR 1742086). The neutron powder diffraction data was collected at The Missouri Research Reactor, University of Missouri (MURR).

## REFERENCES

[1]Nakamura K, Yashima M. Crystal structure of NaCl-type transition metal monocarbides MC (M= V, Ti, Nb, Ta, Hf, Zr), a neutron powder diffraction study. Mater. Sci. Eng., B. 2008;148(1-3):69-72.

[2]Sara RV. The system zirconium—carbon. J. Am. Ceram. Soc. 1965;48(5):243-247.

[3] Moisy-Maurice V, De Novion CH, Christensen AN, Just W. Elastic diffuse neutron scattering study of the defect structure of TiC0.76 and NbC0.73. Solid State Commun. (1981);39(5):661-665.

[4]Lee DW, Alexandrovskii SV, Kim BK. Novel synthesis of substoichiometric ultrafine titanium carbide. Mater. Lett. 2004;58(9):1471-1474.

[5]Tong L, Reddy R. Synthesis of titanium carbide nano-powders by thermal plasma. Scr. Mater. 2005;52(12):1253-1258.

[6]Gusev AI, Zyryanova AN. Atomic-vacancy ordering and magnetic susceptibility of nonstoichiometric hafnium carbide. Journal of Experimental and Theoretical Physics Letters. 1999;69(4):324-329.

[7] Gusev AI, Zyryanova AN. Ordering and Magnetic Susceptibility of Non-Stoichiometric Hafnium Carbide. Phys. Status Solidi A. 2000;177(2):419-437.

[8]Rafaja D, Lengauer W, Ettmayer P, Lipatnikov VN. Rietveld analysis of the ordering in V8C7. J. Alloys Compd. 1998;269(1-2):60-62.

[9]Ordan'yan SS, Avgustinik AI, Kudryasheva LV. Densification of nonstoichiometric niobium-carbide phases. Powder Metall. Met. Ceram. 1968;7(8):612-618.

[10] Rowcliffe DJ, Thomas G. Structure of non-stoichiometric TaC. Mater. Sci. Eng. 1975;18(2):231-238.

[11] Balani K, Gonzalez G, Agarwal A, Hickman R, O'Dell JS, Seal S. Synthesis, microstructural characterization, and mechanical property evaluation of vacuum plasma sprayed tantalum carbide. J. Am. Ceram. Soc. 2006;89(4):1419-1425.

[12] Kurlov AS, Gusev AI. Tungsten Carbides. Berlin: Springer; 2013.

[13] Nachiappan C, Rangaraj L, Divakar C, Jayaram V. Synthesis and densification of monolithic zirconium carbide by reactive hot pressing. J. Am. Ceram. Soc. 2010;93(5):1341-1346.

[14] Wang X, Guo W, Kan Y, Zhang G, Wang P. Densification behavior and properties of hot-pressed ZrC ceramics with Zr and graphite additives. J. Eur. Ceram. Soc. 2011;31(6):1103-1111.

[15] Chakrabarti T, Rangaraj L, Jayaram V. Computational modeling of reactive hot pressing of zirconium carbide. J. Mater. Res. 2015;30(12):1876-1886.

[16] Schönfeld K, Martin H, Michaelis A. Pressureless sintering of ZrC with variable stoichiometry. J. Adv. Ceram. 2017;6(2):165-175.

[17] Kannan R, Venkateswarlu K, Rangaraj L. Effect of nonstoichiometry on mechanical properties of reactive hot-pressed monolithic ZrCx Ceramic. Int. J. Appl. Ceram. Technol. 2018;15(6):1366-1374.

[18] Taylor RE, Storms EK. Thermal Transport in Refractory Carbides. In: Klemens PG, Chu TK. Thermal Conductivity 14. Boston, MA: Springer; 1976:161-174.

[19] Yang Y, Lo WY, Dickerson C, Allen TR. Stoichiometry effect on the irradiation response in the microstructure of zirconium carbides. J. Nucl. Mater. 2014;454(1):130-135.

[20] de Novion CH, Landesman JP. Order and disorder in transition metal carbides and nitrides: experimental and theoretical aspects. Pure Appl. Chem. 1985;57(10):1391-1402.

[21] Gusev AI, Rempel AA, Magerl AJ. Disorder and Order in Strongly Nonstoichiometric Compounds. Heidelberg: Springer; 2001.

[22] Gusev AI, Rempel SV. C - Zr // MSIT Workplace - Research Results. Stuttgart: MSI, 2002;50.12291.7.20:1-2.

[23] Gusev AI. Order-disorder transformations and phase equilibria in strongly nonstoichiometric compounds. Phys.-Usp. 2000;43(1):1-37.

[24] Hu W, Xiang J, Zhang Y, et al. Superstructural nanodomains of ordered carbon vacancies in nonstoichiometric ZrC0.61. J. Mater. Res. 2012;27(9):1230-1236.

[25] Naomi O, Noboru N. Superlattice formation in zirconium-carbon system. J. Nucl. Mater. 1976;60(1):39-42.

[26] Zhang Y, Liu B, Wang J. Self-assembly of Carbon Vacancies in Sub-stoichiometric ZrC1− x. Sci. Rep. 2015;5:18098.

[27] Yu X, Weinberger C, Thompson G. Ab initio investigations of the phase stability in group IVB and VB transition metal carbides. Comput. Mater. Sci. 2016;112:318-326.

[28] Balagurov AM, Bobrikov IA, Bokuchava GD, et al. High-resolution neutron diffraction study of microstructural changes in nanocrystalline ball-milled niobium carbide NbC0. 93. Mater. Charact. 2015;109:173-180.

[29] Kurlov AS, Gusev AI, Kuznetsov VS, Bobrikov IA, Balagurov AM, Rempel AA. Time-of-flight neutron diffraction of nanocrystalline powders of nonstoichiometric niobium carbide NbC0.77. Phys. Solid State. 2017;59(3):607-612.

[30] Kurlov AS, Kuznetsov VS, Bobrikov IA, Balagurov AM, Gusev AI, Rempel AA. Microinhomogeneity of the Structure of Nanocrystalline Niobium and Vanadium Carbides. JETP Lett. 2018;108(4):253-259.

[31] Sørensen OT. Nonstoichiometric oxides. New York: Academic Press; 1981.

[32] Ramana CV, Hussain OM, Naidu BS, Julien C, Balkanski M. Physical investigations on electron-beam evaporated vanadium pentoxide films. Mater. Sci. Eng., B. 1998;52(1):32-39.

[33] Gusev AI. Nonstoichiometry and superstructures. Phys.-Usp. 2014;57(9):839-876.

[34] Qadri SB, Singh A, Yousuf M. Structural stability of PbS films as a function of temperature. Thin Solid Films. 2003;431-432:506-510.

[35] Sadovnikov SI, Kozhevnikova NS, Pushin VG, Rempel AA. Microstructure of nanocrystalline PbS powders and films. Inorg. Mater. 2012;48(1):21-27.

[36] J. Rodriguez-Carvajal, FULLPROF version July-2017, ILL.

[37] Xie C, Oganov AR, Li D, et al. Effects of carbon vacancies on the structures, mechanical properties, and chemical bonding of zirconium carbides: a first-principles-study. Phys. Chem. Chem. Phys. 2016;18(17):12299-12306.

[38] Zhou Y, Heitmann TW, Fahrenholtz WG, Hilmas GE. Synthesis of ZrCx with Controlled Carbon Stoichiometry by Low Temperature Solid State Reaction. J. Eur. Ceram. Soc. 2019;39:2594-2600.

[39] Jackson HF, Lee WE. Properties and characteristics of ZrC. In: Konings RJM, eds. Volume 2 in Comprehensive Nuclear Materials. Amsterdam, Netherland: Elsevier; 2012:339-372

[40] Sarkar SK, Miller AD, Mueller JI. Solubility of oxygen in ZrC. J. Am. Ceram. Soc. 1972;55(12):628-630.

[41] Aigner K, Lengauer W, Rafaja D, Ettmayer P. Lattice parameters and thermal expansion of Ti (CxN1− x), Zr (CxN1− x), Hf (CxN1− x) and TiN1− x from 298 to 1473 K as investigated by high-temperature X-ray diffraction. J. Alloys Compd. 1994;215(1-2):121-126.

[42] Ganguli D, Chatterjee M. Ceramic powder preparation: a handbook. New York: Springer Science+Business Media;1997.

[43] Erich HK, Christopher JH. Applications of Neutron Powder Diffraction. Oxford: Oxford University Press; 2008.

# III. FROM THERMAL CONDUCTIVE TO THERMAL INSULATING: EFFECT OF CARBON VACANCY CONTENT ON LATTICE THERMAL CONDUCTIVITY OF $ZRC_X$

Yue Zhou, William G. Fahrenholtz, Joseph Graham, Gregory E. Hilmas

*Department of Materials Science and Engineering, Missouri University of Science and Technology, Rolla, MO 65409, USA*

## ABSTRACT

Lattice thermal conductivities of zirconium carbide ($ZrC_x$, x=1, 0.75 and 0.5) ceramics with different carbon vacancy concentrations were calculated using a combination of first-principles calculations and the Debye-Callaway model. The Grüneisen parameters, Debye temperatures, and phonon group velocities were deduced from phonon dispersions of $ZrC_x$ determined using first-principles calculations. In addition, the effects of average atomic mass, grain size, average atomic volume and Zr isotopes on the lattice thermal conductivities of $ZrC_x$ were analyzed using phonon scattering models. The lattice thermal conductivity decreased as temperature increased for ZrC, $ZrC_{0.75}$ and $ZrC_{0.5}$ ($Zr_2C$) and decreased as carbon vacancy concentration increased. Intriguingly, $ZrC_x$ can be tailored from a thermal conducting material for ZrC with high lattice thermal conductivity to a thermal insulating material for $ZrC_{0.5}$ with low lattice thermal conductivity. Thus, it opens a window to tune the thermal properties of $ZrC_x$ through controlling the carbon vacancy content.

***Keywords:*** Zirconium carbide; Lattice thermal conductivity; Theoretical study; First-principle calculations.

# 1. INTRODUCTION

Zirconium carbide ($ZrC_x$) is a promising candidate material for nuclear energy applications as a layer in tri-isotropic (TRISO) fuel particles[1], which are used in high-temperature gas-cooled reactors[2]. The main function of the $ZrC_x$ layer is as a diffusion barrier for fission products from the kernel. Currently, SiC is the material of choice for such an application[3]. However, ZrC is stronger, which increases the crushing strength of ZrC-TRISO particles at elevated temperatures compared to SiC-TRISO particles[4]. In addition, ZrC is more stable than SiC under neutron irradiation at elevated temperatures[5][6], which increases the integrity of ZrC-TRISO fuel particles. Other potential applications of ZrC include heating elements in vacuum furnaces, coatings and matrices of ultra-high temperature ceramic matrix composites that could be used in hypersonic aerospace vehicles, rocket nozzles[7][8][9][10][11], and cutting tools[12][13][14].

For all the applications mentioned above, thermal conductivity plays a pivotal role. However, significant discrepancies exist among previously measured values of thermal conductivity of $ZrC_x$ ceramics[15][16][17][18][19] as shown in Figure 1. For example, in one study ZrC with a relative density of 93.3% had a thermal conductivity range from 31 to 38 W/m·K at temperatures from 200 - 1000°C[15]. In another study, ZrC with a relative density of 91.9% had a thermal conductivity range from 18 to 26 W/m·K at temperatures from 300 - 1100°C[14]. One possible reason for such differences is that these $ZrC_x$ samples were prepared by different methods that resulted in different average grain sizes, carbon vacancy contents, and/or porosity levels/distributions and relative densities. Table 1 summarizes the preparation methods and characteristics of zirconium carbide

ceramics from previous studies. The highest thermal conductivity values were reported for ZrC with larger grain sizes, lower carbon vacancy contents, and higher relative

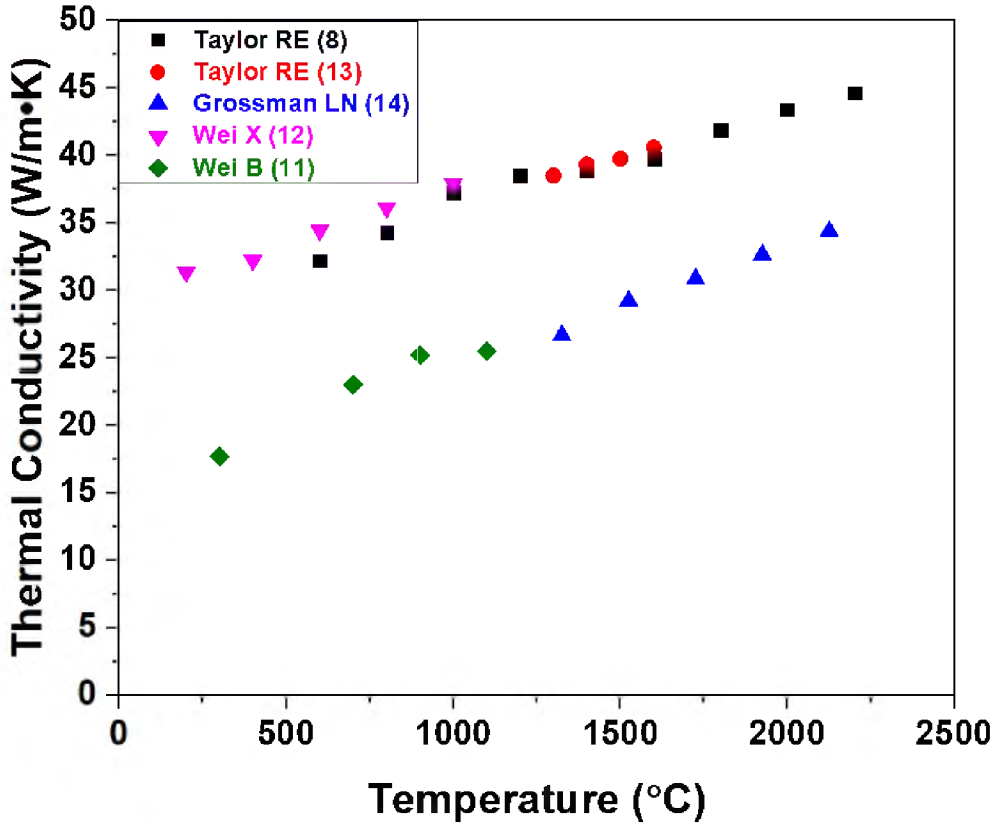


Figure 1. Thermal conductivities of zirconium carbide ceramics measured in previous studies.

densities[13]. The typical room temperature thermal conductivity is about 30 W/m·K, depending on relative density[15].

In the Zr-C phase diagram, rock salt structured zirconium carbide is stable across a wide composition range and is represented by $ZrC_x$ with x ranging from 0.98 to 0.63 (i.e., carbon vacancy contents from 0.02 to 0.37)[20]. The change of carbon content not

only influences the lattice constant of $ZrC_x$, but also the thermal and mechanical properties. Previous studies demonstrated that the total thermal conductivity of $ZrC_x$

Table 1. Densification methods and sample characteristics of $ZrC_x$ from previous studies sorted by highest to lowest thermal conductivity.

| Ref. | Densification method | Composition | Relative density | Average grain size | Impurity Content | Thermal conductivity (W/m·K) |
|---|---|---|---|---|---|---|
| 8 | HP | $ZrC_{0.98}$ | 95% | 50 μm | <0.2 wt% | 32.2, 600°C |
| 13 | HP | $ZrC_{0.98}$ | 95% | 50 μm | <0.2 wt% | 38.5, 1300°C |
| 12 | SPS | ZrC | 93.3% | ~10 μm | N/A | 31.3, 200°C |
| 14 | HP | ZrC | 91.5% | N/A | >0.165 wt% | 26.7, 1325°C |
| 11 | HP | ZrC | 91.9% | 3.7 μm | N/A | 17.7, 300°C |

decreased with increasing carbon vacancy content[21] due to the scattering of phonons and electrons by carbon vacancies. Likewise, theoretical studies[22][23] predicted that the elastic properties, Vickers hardness, and thermal conductivities of $ZrC_x$ decreased with increasing carbon vacancy content. However, relatively few studies have been conducted using first-principles calculations to examine the lattice thermal conductivities of $ZrC_x$ with different carbon vacancy contents. Molecular dynamics[24] and the Debye-Slack model[21] have been used to calculate the lattice thermal conductivities of $ZrC_x$ with different carbon vacancy concentrations. However, the Debye-Callaway model has not been used to evaluate the effect of carbon vacancy on the lattice thermal conductivity of $ZrC_x$[25][26]. The effect of ordering of carbon vacancies on the lattice thermal conductivity was also investigated since the carbon vacancy ordered phase $ZrC_{0.5}$ has not only been predicted computationally[27][28] but also been observed experimentally[29][30]. However,

due to the fact that the carbon vacancy ordered $Zr_2C$ always coexists with rock salt structured $ZrC_x$, its effect on the thermal conductivity of $ZrC_x$ is difficult to determine experimentally. Thus, theoretical prediction of the lattice thermal conductivity of this ordered phase is needed.

$ZrC_x$ is electrically conductive such that both electron and phonon transport contribute to thermal conductivity. As shown in Figure 1, the total thermal conductivity of $ZrC_x$ increases with increasing temperature, which is attributed to the increasing contribution of the electron contribution as temperature increases[31]. In addition, oxygen can dissolve into the $ZrC_x$ lattice and is expected to be present in the carbon vacancy sites[32]. Furthermore, phonon scattering is expected to increase when impurity atoms are present[33] so that the phonon thermal conductivity of $ZrC_x$ should decrease with increasing dissolved oxygen content. Thus, tailoring the thermal conductivity of zirconium carbide requires a deeper understanding of the mechanisms affecting the phonon transport in the lattice.

The Debye model is a statistical thermodynamic methodology to estimate the phonon contribution to heat capacity[34]. When the temperature ($T$) is much lower than the Debye temperature ($\theta_D$), which is designated the "low" temperature regime, the model accurately predicts that heat capacity is proportional to $T^3$. In the low-temperature regime, the phonon group velocity ($v$) has a linear relationship with the frequency distribution of acoustic phonons and is expressed as $\omega = v\boldsymbol{q}$, where ω is the phonon frequency, $v$ is group velocity, and $\boldsymbol{q}$ is the wave vector of the phonon. Optical phonons are not active in the low-temperature regime. Likewise, the Debye model accurately predicts heat capacity in the "high" temperature limit where $T >> \theta_D$ and the Debye model simplifies to the

DuLong-Petit Law. However, at intermediate temperatures where both low and high-frequency phonons are active, the relationship between the acoustic phonon frequency and group velocity is no longer linear, leading to significant inaccuracies in the phonon frequency distribution predicted by the Debye model.

Klemens studied the statistical equilibrium of phonons with respect to temperature gradients and developed a general prediction for the thermal conductivity of dielectric solids with fixed equilibrium atom positions[35]. When atoms deviate from their ideal (i.e., absolute zero) positions, phonons scatter. The mean time between scattering events is defined as the relaxation time and different relaxation times can be determined for each phonon scattering process. Phonon scattering processes are typically divided into two main types: normal processes (N) in which phonon momentum is not changed by scattering and Umklapp processes (U) that change phonon momentum. Normal processes dominate in the low-temperature regime. In contrast, U processes, such as anharmonic phonon-phonon and phonon-electron interactions, typically dominate in the high-temperature regime. Built on the Klemens model, Callaway argued that the total crystal momentum was conserved in N processes, which led to the conclusion that N processes do not contribute to thermal conduction. Callaway modified the initial model to capture the linear relationship between group velocity and the frequency distribution of acoustic phonons[36]. This enabled prediction of thermal conductivity in temperature regimes in which the Debye model accurately captured the phonon frequency distribution (i.e., the low-temperature regime). However, the Debye-Callaway model is not accurate at intermediate temperatures because of inaccuracies in the predictions of the underlying Debye model in this temperature regime.

First-principles calculations can be used to improve the accuracy of the Debye-Callaway model in the intermediate temperature regime by directly determining phonon group velocities and frequency distributions. Using this methodology, intrinsic thermal conductivities have been predicted for γ-$Si_3N_4$, γ-$Ge_3N_4$[37], $ZrB_2$[38], copper antimony selenium, and tin-selenium compounds[39]. For example, this methodology predicted a lattice thermal conductivity of about 300 W/m•K for γ-$Si_3N_4$ at room temperature, which is only ~50% higher than the highest experimentally measured value[40][41]. In contrast, the Slack model predicted a lattice thermal conductivity of 80 W/m·K[42] for the same material, which is less than half of the highest experimental value. Hence, utilizing first-principles calculations to determine phonon vibration frequency distributions improves the accuracy of the Debye-Callaway model in the intermediate temperature regime.

Up to now, this methodology has not been used to predict the thermal conductivity of $ZrC_x$ ceramics. The purpose of the present study is to use a combination of first-principles calculations and the Debye-Callaway model to predict the lattice thermal conductivities of $ZrC_x$ with different carbon stoichiometries. The result of this study is not only useful in explaining the origin of discrepancies in experimentally measured thermal conductivities but also can be used as a guideline for tuning the thermal properties of $ZrC_x$ ceramics.

# 2. CALCULATION METHODS

## 2.1. LATTICE THERMAL CONDUCTIVITY

The total thermal conductivity ($\kappa_{total}$) of $ZrC_x$ arises from both electron ($\kappa_e$) and lattice ($\kappa_L$) contributions, $\kappa_{total} = \kappa_e + \kappa_L$. The magnitude of the electron contribution can be estimated using the Wiedemann-Franz law[43], $\kappa_e = \frac{L_0 T}{\rho}$, where $L_0 = 2.45\times10^{-8}$ $W/\Omega\cdot K^2$ is the theoretical Lorenz number. Previous studies suggested that $\kappa_L$ was the dominant contribution to $\kappa_{total}$ of $ZrC_x$ at lower temperatures[44]. In addition, the calculation of the electron contribution using the Wiedemann-Franz law is straight-forward. As a result, $\kappa_L$ will be the focus of the present study.

A combination of the Debye-Callaway model[45] and first-principles simulations was employed for calculating $\kappa_L$ of $ZrC_x$ with different carbon stoichiometries (ZrC, $ZrC_{0.75}$, and $ZrC_{0.5}$ which is also called $Zr_2C$ in some studies) at different temperatures. In the Debye-Callaway model, heat is assumed to be transported by acoustic phonon modes because the group velocities of the optical phonons are significantly lower, which means their contribution to total thermal conductivity is small[46][35][47]. Two transverse (*TA1* and *TA2*) and one longitudinal (*LA*) acoustic phonon branches contribute to $\kappa_L$ , which can be expressed by Equation 1:

$$\kappa_L = \kappa_{TA1} + \kappa_{TA2} + \kappa_{LA} \tag{1}$$

The acoustic phonon branches ($\kappa_i$, with $i$ represents *TA1*, *TA2* and *LA*) are the usual Debye-Callaway terms and are expressed by Equations 2 and 3:

$$\kappa_{i1} = \frac{1}{3}\frac{k_B^4 T^3}{2\pi^2\hbar^3 v_i}\int_0^{\frac{\theta_i}{T}}\frac{\tau_C^i(x)x^4e^x}{(e^x-1)^2}dx \tag{2}$$

$$\kappa_{i2} = \frac{1}{3}\frac{k_B^4 T^3}{2\pi^2 \hbar^3 v_i}\frac{\left[\int_0^{\frac{\theta_i}{T}} \frac{\tau_C^i(x) x^4 e^x}{(e^x-1)^2} dx\right]^2}{\int_0^{\frac{\theta_i}{T}} \frac{\tau_C^i(x) x^4 e^x}{\tau_N^i(x)\tau_R^i(x)(e^x-1)^2} dx} \quad (3)$$

In Equation 3, $k_B$ is the Boltzmann constant, $\hbar$ is the reduced Planck constant, $v_i$ is the group velocity of the phonons, $\theta_i$ is the Debye temperature of the transverse and longitudinal acoustic phonons, respectively, which is determined by $\theta_i = \hbar\omega_{max}/k_B$, where $\omega_{max}$is the maximum frequency of the acoustic phonon branches at the Brillouin zone boundary[48]. The factor $x$ is expressed by $x = \hbar\omega/k_B T$, $\tau_C$ is the total relaxation time of the active phonon scattering processes. In Equation 3, $\tau_N$ is the scattering rate for normal phonon processes, while $\tau_R$ is the sum of all of the resistive scattering processes. The relationship between the last three factors is $\tau_C^{-1} = \tau_N^{-1} + \tau_R^{-1}$. The total resistive phonon scattering rate ($\tau_R^{-1}$) is the sum of the phonon-phonon Umklapp scattering ($\tau_U^{-1}$), isotope scattering ($\tau_I^{-1}$), grain boundary scattering ($\tau_B^{-1}$), and phonon-vacancy scattering ($\tau_V^{-1}$) rates. The latter was considered only for $ZrC_{0.75}$ since ZrC has no vacancies and the space group for $ZrC_{0.5}$ accounts for carbon vacancies in that structure. The relaxation time of the Umklapp scattering process can be expressed as Equation 4[49]:

$$\left[\tau_U^i\right]^{-1} = \frac{\hbar\gamma_i^2}{M v_i^2 \theta_i}\left(\frac{k_B}{\hbar}\right)^2 x^2 T^3 exp\left(\frac{-\theta_i}{3T}\right) \quad (4)$$

where $M$ is the average mass of atoms in the crystal, $\gamma_i$ is the Grüneisen parameter of the acoustic phonon branch which is estimated by Equation 5[50]:

$$\gamma_i = \frac{\sum \gamma_{i,q} C_i(\boldsymbol{q})}{\sum C_i(\boldsymbol{q})} \quad (5)$$

where $\gamma_{i,q}$ is the mode Grüneisen parameter for mode $i$ at wave vector $\boldsymbol{q}$ which is determined by Equation 6:

$$\gamma_{i,\boldsymbol{q}} = -\frac{\partial ln\omega_{i,q}}{\partial lnV} \tag{6}$$

where $V$ is the volume of the unit cell. In Equation 5, $C_i(\boldsymbol{q})$ is defined by Equation 7:

$$C_i(\boldsymbol{q}) = k_B \left(\frac{\hbar\omega_{i,q}}{k_B T}\right)^2 \frac{exp\left(\frac{\hbar\omega_{i,q}}{k_B T}\right)}{\left[exp\left(\frac{\hbar\omega_{i,q}}{k_B T}\right)-1\right]^2} \tag{7}$$

Isotope scattering was assumed to be scattering from static imperfections with masses that are different from the host in a perfect crystal structure and is expressed as Equation 8[51]:

$$\left[\tau_I^i\right]^{-1} = \frac{Vk_B^4\Gamma}{4\pi\hbar^4 v_L^3} x^4 T^4 \tag{8}$$

where $\Gamma$ is the phonon-scattering parameter of the mass-fluctuation which can be calculated by Equations 9 and 10:

$$\Gamma = \sum_j c_j \left[\frac{m_j - \bar{m}}{\bar{m}}\right]^2 \tag{9}$$

$$\bar{m} = \sum_j c_j m_j \tag{10}$$

where $c_j$ is the fractional atomic natural abundance of the isotope with atomic mass, $m_j$. Scattering from Zr isotopes is also considered in the present work using analysis similar to Equations 8 and 9. The abundance of the isotopes is assumed to be 51.45 wt% $^{90}$Zr, 11.22 wt% $^{91}$Zr, 17.15 wt% $^{92}$Zr, 17.38 wt% $^{94}$Zr, and 2.80 wt% $^{96}$Zr.

Grain boundary scattering was assumed to be independent of temperature and phonon frequency and only dependent on group velocity and grain diameter[40] as shown by Equation 11:

$$\left[\tau_B^i\right]^{-1} = \frac{v_i}{d} \tag{11}$$

where $d$ is the effective diameter of the $ZrC_x$ grains.

Phonon-vacancy scattering was assumed to occur due to the atomic mass and radius differences when vacancies form in a crystal structure[52] as described by Equation 12:

$$[\tau_V]^{-1} = \sum_i f_i(1-\frac{m_i}{\bar{m}})^2 + \sum_i f_i(1-\frac{r_i}{\bar{r}})^2 \quad (12)$$

where $f_i$ is the ratio of vacancy, $\bar{m}$ and $m_i$ are the average masses before and after the vacancy formed, $\bar{r}$ and $r_i$ are the average atomic radius before and after the vacancy formed. As noted previously, phonon-phonon scattering was considered to be a U process and its effect on lattice thermal conductivity is determined using the Callaway model as shown in Equation 13[33]:

$$[\tau_N^L]^{-1} = \frac{Vk_B^5\gamma_L^2}{M\hbar^4 v_T^5} x^2 T^5 \quad (13)$$

The phonon group velocity is defined by Equation 14:

$$v_g(i,\boldsymbol{q}) = \frac{\partial\omega(i,\boldsymbol{q})}{\partial \boldsymbol{q}} \quad (14)$$

where the gradient of the dispersion curve at $\Gamma$ is the group velocity.

## 2.2. FIRST-PRINCIPLE CALCULATIONS

ZrC crystallizes in rock salt structure with a space group of $Fm\bar{3}m$ (No. 225) (Figure 2a). The lattice parameter is $a$ = 4.699 Å[22]. Zr and C atoms are located at (0, 0, 0) and (0.5, 0.5, 0.5), respectively. The crystal structure of $ZrC_{0.75}$ was built by removing one C atom from the 1×1×1 unit cell of ZrC, as shown in Figure 2b, which results in ordered vacancies for the $ZrC_{0.75}$ structure at the scale of the unit cell. The carbon vacancy ordered crystal structure $Zr_2C$ was used for $ZrC_{0.5}$, which was built according to a Rietveld refined structure from the X-ray diffraction pattern[53]. The space group is $Fd\bar{3}m$ (No. 227) and the lattice parameter is $a$ = 9.399 Å. The Zr and C atoms are located

at (0.3702, 0.3702, 0.3702) and (0.1250, 0.1250, 0.1250) positions, respectively, as shown in Figure 2c. This structure is essentially a 2x2x2 super cell of the ZrC unit cell, but with an ordered array of carbon vacancies that requires the larger super cell to fully describe the ordering.

Quantum Espresso (QE)[54] was employed to perform the density functional theory (DFT) calculations. Crystal structures were optimized using the Broyden-Fletcher-Goldfarb-Shanno (BFGS) scheme to minimize the total energy and interatomic force[55]. The criteria for convergence in optimizing lattice parameters and internal atom positions were total energy differences within 0.1 mRy/atom. Vanderbilt-type ultrasoft pseudopotentials[56] were employed to represent the interactions between atom cores and valence electrons. The exchange-correlation energy was treated under the generalized-gradient approximation (GGA)[57] based on the Perdew-Burke-Ernzerhof (PBE) scheme. The cutoff of kinetic energy for wavefunctions were fixed at 70 Ry in structure relaxation and self-consistent calculations after convergence tests for all structures. Brillouin zone sampling integration was conducted by the Monkhorst-Pack method[58] with a k-points

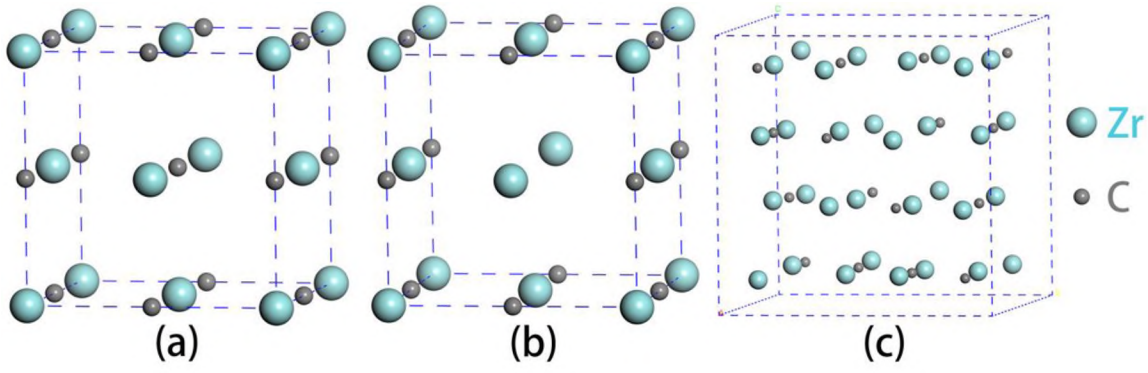


Figure 2. Crystal structures of (a) ZrC, (b) $ZrC_{0.75}$ and (c) $Zr_2C(ZrC_{0.5})$.

mesh separation of 0.04 $Å^{-1}$. Elastic constants were calculated for all three compositions (ZrC, $ZrC_{0.75}$ and $ZrC_{0.5}$). A finite value of homogeneous deformation was generated for calculating the required stress. The three independent symmetry elements, $c_{11}$, $c_{12}$ and $c_{44}$ of the cubic structure were generated for estimating the polycrystalline shear modulus $G$ and bulk modulus $B$ according to the Voigt-Reuss-Hill approximation[59]. The Young's modulus $E$, Poisson's ratio ν and microhardness $H_V$ were calculated based on shear modulus $G$ and bulk modulus $B$ according to the following relationships for isotropic materials[60]:

$$E = \frac{9BG}{3B+G} \tag{16}$$

$$\nu = \frac{3B-2G}{2\times(3B+G)} \tag{17}$$

$$H_V = 2 \times \left(\frac{G^3}{B^2}\right)^{0.585} - 3 \tag{18}$$

In Equation 18, microhardness has a unit of GPa, which must also be used for $G$ and $B$ in this calculation. Phonon frequencies as functions of Brillouin zone directions were conducted using density functional perturbation theory (DFPT)[61] with a 9×9×9, 6×6×6, and 5×5×5 $k$-points mesh for ZrC, $ZrC_{0.75}$, and $ZrC_{0.5}$, respectively. In the phonon calculations within the quasi harmonic approximation (QHA), the cell volume was varied by less than ±1% with respect to the equilibrium cell volume of ZrC, $ZrC_{0.75}$ and $ZrC_{0.5}$.

# 3. RESULTS AND DISCUSSION

## 3.1. LATTICE PARAMETERS, ELASTIC CONSTANTS, AND MECHANICAL PROPERTIES

Lattice parameters of ZrC, $ZrC_{0.75}$ and $ZrC_{0.5}$ were calculated in the present study and are compared in Table 2. The lattice parameter of $ZrC_{0.75}$ was 4.692 Å, which was smaller than the lattice parameter of 4.706 Å for ZrC due to the presence of the carbon vacancies. The lattice parameter of $ZrC_{0.5}$ was larger than those for ZrC and $ZrC_{0.75}$ since the crystal structure contains 48 atoms compared to 8 atoms for ZrC and 7 atoms for $ZrC_{0.75}$. However, the average distance between two neighboring Zr atoms along the crystallographic axes was 4.717 Å, which is analogous to the lattice parameter for the other two structures. The lattice expanded for $ZrC_{0.5}$ in contrast to the trend from ZrC to $ZrC_{0.75}$. The lattice parameter decreased as carbon vacancy content increased initially due to the loss of carbon atoms that resulted in shrinkage of the structure. However, when the carbon vacancy content reaches about 20% (i.e., $ZrC_{0.8}$), the average distance between Zr atoms begins to increase due to the decrease in bond strength that results from the increasing metallic bond character with increasing carbon vacancy content[62].

Elastic properties are direct reflection of chemical bonding. Table 2 tabulates the elastic constants and microhardness of ZrC, $ZrC_{0.75}$ and $ZrC_{0.5}$. Data from previous publications are also included for comparison. The calculated mechanical properties of ZrC and $ZrC_{0.5}$ are consistent with the values from previous studies. For example, the second-order elastic constants $c_{11}$, $c_{44}$ and $c_{12}$ of ZrC are 451.6 GPa, 155.4 GPa and 106.9 GPa, respectively, which are very close to corresponding values of 451.6 GPa, 155.3 GPa and 106.9 GPa calculated in a previous report[63], demonstrating the reliability of present

calculations. The bulk modulus $B$, shear modulus $G$ and elastic modulus $E$ of polycrystalline $ZrC_x$ all decrease with increasing carbon vacancy content. For example, $G$ decreases from 162.2 GPa for ZrC to 119.5 GPa $ZrC_{0.75}$, and 82.1 GPa for $ZrC_{0.5}$. Correspondingly, $Hv$ decreases from 24.2 GPa for ZrC to 16.2 GPa for $ZrC_{0.75}$ and 11.7 GPa for $ZrC_{0.5}$. In contrast, Poisson's ratio increases with increasing carbon vacancy

Table 2. Calculated lattice parameters ($a$ (Å)), elastic constants ($c_{11}$, $c_{44}$, $c_{12}$) (GPa), shear modulus $G$ (GPa), bulk modulus $B$ (GPa), elastic modulus $E$ (GPa), Poisson's ratio $\nu$, and microhardness $H_V$ (GPa) of ZrC, $ZrC_{0.75}$ and $Zr_2C$ ($ZrC_{0.5}$) in the present and *(previously reported)* calculations.

| Composition | ZrC | $ZrC_{0.75}$ | $Zr_2C(ZrC_{0.5})$ |
|---|---|---|---|
| Lattice constant $a$ (Å) | 4.706, *(4.705)*[63] | 4.692 | 9.369[22] |
| $c_{11}$ | 451.6, *(451.6)*[63] | 369.2 | 205.3 |
| $c_{44}$ | 155.4, *(155.3)*[63] | 108.9 | 101.6 |
| $c_{12}$ | 106.9, *(106.9)*[63] | 98.4 | 100.0 |
| $G$ | 162.2, *(162.1)*[63] | 119.5 | 82.1, *(71)*[22] |
| $B$ | 221.8, *(221.8)*[63] | 188.6 | 135.1, *(137)*[22] |
| $E$ | 391.2, *(390.7)*[63] | 295.9 | 204.7 |
| $\nu$ | 0.21, *(0.206)*[61] | 0.24 | 0.25 |
| $H_V$ | 24.2, *(23.4)*[21], *(24.3)*[22] | 16.2 | 11.7, *(8.4)*[22], *(10.8)*[23] |

content from 0.21 for ZrC to 0.25 for $ZrC_{0.5}$, indicating a decrease in average bond strength as carbon atoms are removed from the structure.

## 3.2. PHONON DISPERSIONS AND VIBRATION PROPERTIES

Phonon dispersion curves for ZrC are shown in Figure 3a. The primitive ZrC cell contains one Zr atom and one C atom, which result in six phonon branches, i.e., three acoustic (colored lines) and three optical (black lines). No imaginary frequencies were predicted in any of the high-symmetry directions in the Brillouin zone, indicating the dynamic stability of ZrC under perturbation. The apparent gap between the acoustic phonon branches and optical phonon branches (>5 THz at the L point) is due to anisotropic bonding and mass differences between Zr and C in ZrC. These results also suggest that the contribution of the optical modes to the thermal conductivity of ZrC is negligible due to the significantly higher frequencies, as has been demonstrated in $ZrB_2$ by Xiang et al[42].

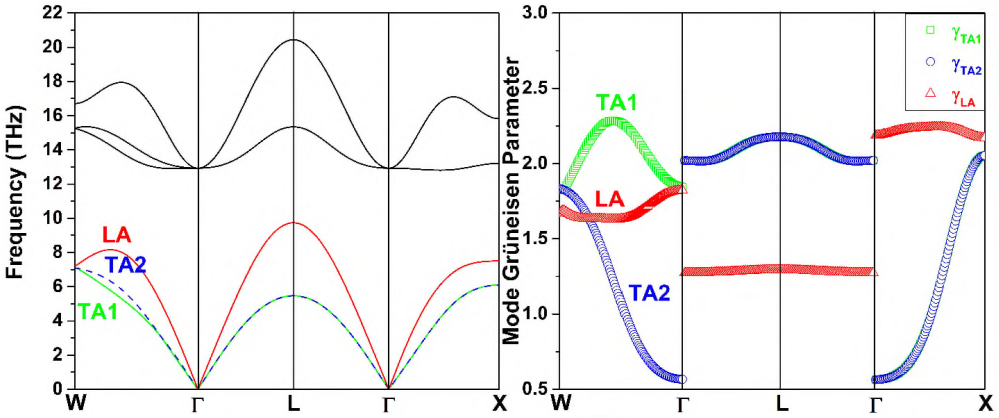


Figure 3. Phonon dispersion (a) and mode Grüneisen parameters (b) of ZrC.

The phonon group velocities for *TA*1, *TA*2, and *LA* of ZrC are 4.2 km/s , 4.2 km/s and 8.0 km/s, respectively, in the Γ-X direction (Table 3). Since spectral thermal conductivity is proportional to the square of the phonon group velocity, $\kappa_s(\omega) =$

$C_s(\omega)V_g(\omega)^2\tau(\omega)$[38], the higher group velocities are an indication of higher thermal conductivity for ZrC. Thermal conductivity is also proportional to the phonon relaxation time[39], which is the mean time between scattering events attributed to the various resistive processes.

The phonon relaxation time can be determined from the mode Grüneisen parameters, $\gamma_i$, which is related to the anharmonicity of the phonon vibrations and plays an important role in thermal conductivity. The mode Grüneisen parameters are calculated using harmonic lattice dynamic calculations over a range of volumes around the

Table 3. The Grüneisen parameters, Debye temperatures, and group velocities of ZrC, $ZrC_{0.75}$ and $Zr_2C$ ($ZrC_{0.5}$) compared with a highly thermal conductive ($ZrB_2$)[37] and thermal insulating rare-earth pyrochlores[64].

| | $\gamma_{TA1}$ | $\gamma_{TA2}$ | $\gamma_{LA}$ | $\theta_{TA1}$ | $\theta_{TA2}$ | $\theta_{LA}$ | $v_{TA1}$ | $v_{TA2}$ | $v_{LA}$ |
|---|---|---|---|---|---|---|---|---|---|
| Unit / Composition | N/A | | | (K) | | | (km/s) | | |
| ZrC | 1.79 | 1.51 | 1.65 | 340 | 340 | 467 | 4.2 | 4.2 | 8.0 |
| $ZrC_{0.75}$ | 0.92 | 1.28 | 1.52 | 242 | 242 | 242 | 2.4 | 2.4 | 3.2 |
| $Zr_2C$ | 10.05 | 9.12 | 4.32 | 167 | 172 | 220 | 4.0 | 4.8 | 7.1 |
| $ZrB_2$ | 1.50 | 1.22 | 1.43 | 380 | 355 | 422 | 6.5 | 6.5 | 9.2 |
| $Nd_2Zr_2O_7$ | 6.23 | 10.10 | 2.75 | 138 | 138 | 260 | 3.13 | 3.13 | 5.91 |
| $Sm_2Zr_2O_7$ | 7.40 | 11.98 | 2.81 | 137 | 137 | 256 | 3.09 | 3.09 | 5.78 |
| $Gd_2Zr_2O_7$ | 7.19 | 11.57 | 2.75 | 137 | 137 | 252 | 3.06 | 3.06 | 5.63 |

equilibrium state using Equation 6. As shown in Figure 3b, the mode Grüneisen parameters of ZrC are positive across the Brillouin zone, which implies that ZrC is stable in the rock salt structure at elevated pressures.

Figure 4a shows the phonon dispersion curves for $ZrC_{0.75}$. Compared to ZrC, the phonon dispersion curves for $ZrC_{0.75}$ contain additional optical phonon modes at frequencies between ~6 THz and ~8 THz, which are due to the presence of carbon vacancy. These moderate frequency optical phonons scatter acoustic phonons (i.e., phonon-phonon scattering), especially the longitudinal acoustic phonon branch. The scattering of acoustic phonons results in reduced group velocities as can be seen from the gradient of the dispersion curve at the Γ points in Figure 4a and the data in Table 3. In

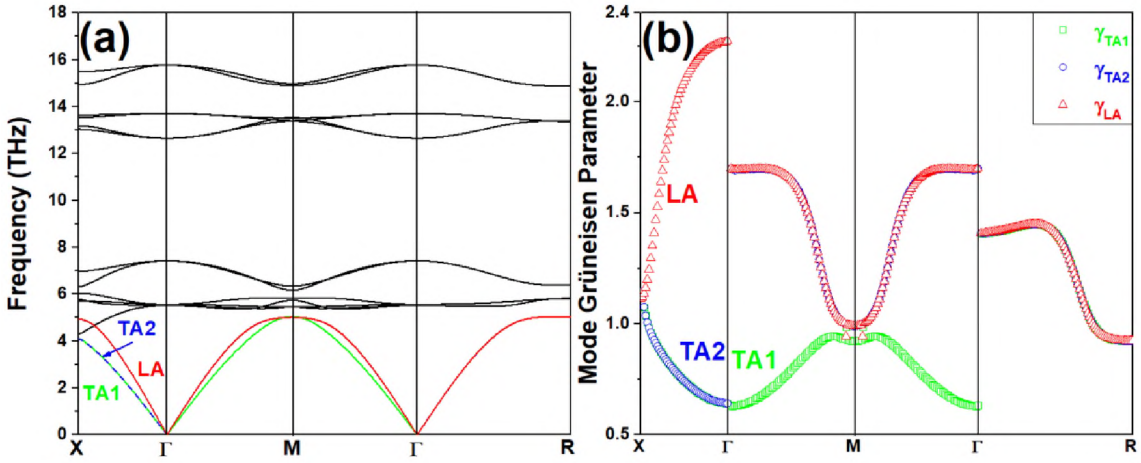


Figure 4. Phonon dispersion (a) and mode Grüneisen parameters (b) of $ZrC_{0.75}$.

addition, the scattering of acoustic phonons by the moderate frequency optical phonons also decreases the Debye temperature and increases the longitudinal acoustic mode Grüneisen parameter compared to ZrC (Figure 4b). Since the Debye temperature is determined by the maximum frequency of the acoustic branches at the Brillouin zone boundary, a decrease in the Debye temperature is reasonable (Table 3) based on Figure 3 and Figure 4. For example, $\theta_{TA1}$ and $\theta_{TA2}$ decrease from 340 K for ZrC to 242 K for $ZrC_{0.75}$, while $\theta_{LA}$ decreases from 467 K for ZrC to 242 K for $ZrC_{0.75}$. As a consequence,

scattering of acoustic phonons by the moderate frequency optical phonons is active in $ZrC_{0.75}$, but not in ZrC, which should decrease the lattice thermal conductivity of $ZrC_{0.75}$.

When more carbon atoms were removed from the structure and $ZrC_{0.5}$ formed, more optical phonon modes were active at frequencies between ~4 THz and ~8 THz, as

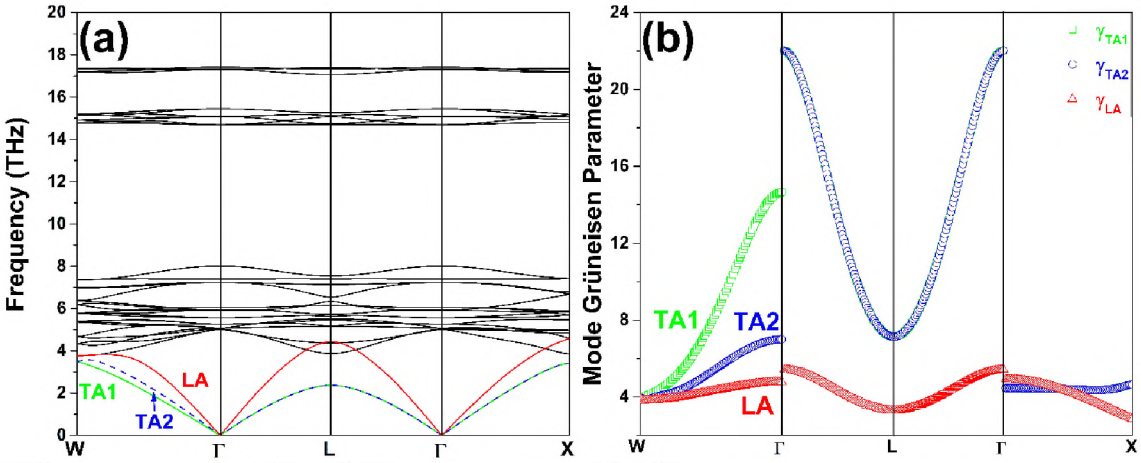


Figure 5. Phonon dispersion (a) and mode Grüneisen parameters (b) of $Zr_2C$ ($ZrC_{0.5}$).

can be seen from the phonon dispersion curves shown in Figure 5a. The number of thesemoderate frequency optical modes increased from 0 for ZrC to 9 for $ZrC_{0.75}$, and 21 for $ZrC_{0.5}$. Scattering of acoustic phonons by these low-lying optical phonons resulted in lower group velocities, which were $v_{TA1}$ = 4.0 km/s, $v_{TA2}$ = 4.8 km/s and $v_{LA}$ = 7.1 km/s (as can be seen from the reduced gradient of the dispersion curve at the Γ points in Figure 5a and Table 3). In addition, the mode Grüneisen parameters of the acoustic branches were very large with *TA*1, and *TA*2 values of more than 22 and *LA* of more than 5 (Figure 5b). Since the mode Grüneisen parameter is a measure of lattice vibration anharmonicity, the large values indicate that the phonon thermal conductivity of $ZrC_{0.5}$ will be much

lower than ZrC or $ZrC_{0.75}$ due to the increased anharmonicity. The longitudinal acoustic phonon branches and the moderate frequencies optical phonon branches overlapped due to scattering of optical phonons by carbon vacancies. The frequencies of the acoustic phonon branches for $ZrC_{0.5}$ were lower than those for $ZrC_{0.75}$, so the Debye temperatures decreased as well (Table 3). For example, $\theta_{TA1}$ and $\theta_{TA2}$ decreased from 242 K for $ZrC_{0.75}$ to 167 K and 172 K for $ZrC_{0.5}$, respectively while $\theta_{LA}$ decreased from 242 K for $ZrC_{0.75}$ to 220 K for $ZrC_{0.5}$. The reduction in the Debye temperature for $ZrC_x$ with increasing carbon vacancy content is consistent with previous studies[22].

### 3.3. GRŰNEISEN PARAMETERS

The Grüneisen parameters ($\gamma_i$), Debye temperatures ($\theta_i$) and group velocities ($v_i$) of the acoustic phonon branches (Table 3) are the determinant parameters for calculating the phonon thermal conductivity. The changes in the thermal properties of $ZrC_x$ can be summarized by comparing the Grüneisen parameters and Debye temperatures with materials that have high lattice thermal conductivities, such as $ZrB_2$[35], and low lattice thermal conductivities, such as rare-earth pyrochlore materials[50]. Grüneisen parameters and Debye temperatures of ZrC are close to $ZrB_2$ (For example, $\gamma_{TA1}$ values are 1.79 and 1.50, $\theta_{TA1}$ values are 340 K and 380 K for ZrC and $ZrB_2$[35], respectively) as presented in Table 3. As the carbon vacancy content increases, the values of the Grüneisen parameters and Debye temperatures tend to change toward representative low lattice thermal conductivity materials such as $Gd_2Zr_2O_7$[64]. Hence, the lattice thermal conductivity of $ZrC_x$ should decrease to values similar to thermal insulators as the carbon vacancy content increases. This result is intriguing since it implies that the thermal conductivity of

$ZrC_x$ can be tuned from a high thermal conductivity/thermal dissipating material to a low thermal conductivity/thermal insulating material through controlling the composition and carbon vacancy content. From this angle, the lattice thermal conductivity can be increased with high x such as ZrC and decreased with low x such as $ZrC_{0.5}$.

### 3.4. THERMAL CONDUCTIVITY

The temperature-dependent lattice thermal conductivities of ZrC, $ZrC_{0.75}$ and $ZrC_{0.5}$ predicted using the Debye-Callaway model are shown in Figure 6. The initial simulations predicted lattice thermal conductivities, labeled $\kappa_{UI}$ in Figure 6, of 122 W/m·K for ZrC, 33 W/m·K for $ZrC_{0.75}$, and 3 W/m·K for $ZrC_{0.5}$, considering the natural abundance of Zr isotopes. From these simulations, the lattice thermal conductivity of $ZrC_x$ decreases with the increasing carbon vacancy content. This decreasing trend is consistent with expectations based on trends in the Grüneisen parameters and Debye temperatures discussed above. The significant change of lattice thermal conductivity opens a new window to tailor the thermal conductivity of $ZrC_x$ through composition and carbon vacancy control. However, the predicted values of ZrC and $ZrC_{0.75}$ are higher than the experimental values for total thermal conductivity at room temperature, which are less than 30 W/m·K for $ZrC_x$ with low (but not well-characterized) carbon vacancy contents. One reason that the predicted lattice thermal conductivity values are higher than measured values for $ZrC_x$ ceramics is that the simulations assumed perfect crystal structure without any impurities or defects. In addition, other possible scattering mechanisms may also need to be considered to decrease the predicted values and make them more realistic compared to experimental values. For ZrC, the room temperature

lattice thermal conductivity decreased from 122 W/m·K when only considering isotope effects ($\kappa_{UI}$) to 100 W/m·K when considering isotope and grain boundary effects ($\kappa_{UA}$), and 68 W/m·K when considering isotope and grain boundary effects along with N and U scattering processes ($\kappa_N$). Even with these effects, the room temperature thermal conductivity of ZrC is still about twice of the experimental value, so other scattering mechanisms may have a significant impact on the lattice thermal conductivity of $ZrC_x$ ceramics. The simulations may also predict values that are too high since the sizes of the cells in the simulations were not large enough to capture the effects of random carbon vacancies (i.e., the simulations include the implicit assumption that the carbon vacancies

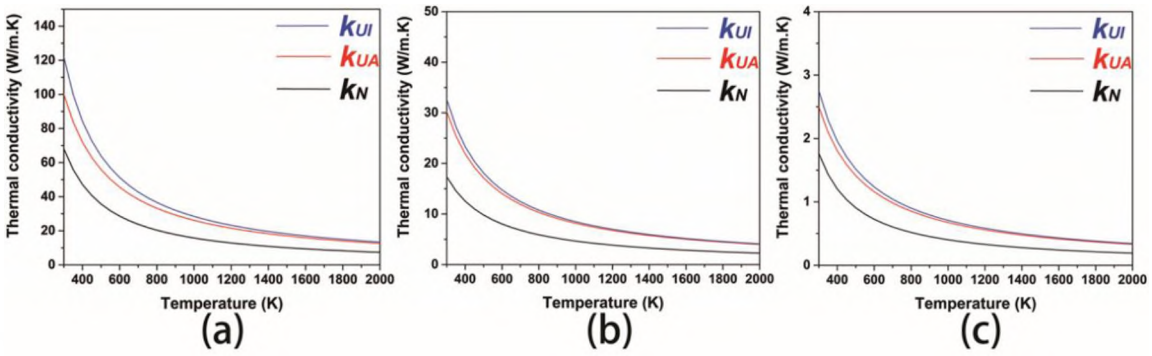


Figure 6. Lattice thermal conductivities of (a) ZrC, (b) $ZrC_{0.75}$ and (c) $Zr_2C$ ($ZrC_{0.5}$) based on theoretical prediction. ($\kappa_{UI}$: isotope effect; $\kappa_{UA}$: isotope and grain boundary effects; $\kappa_N$: isotope, grain boundary, U, and N effects.)

are ordered). Hence, simulations provide an upper bound for possible thermal conductivity values.

The lattice thermal conductivities decreased as temperature increased due to the increased phonon-phonon scattering[4]. When temperature is much higher than the Debye temperature, the number of phonons becomes proportional to temperature, and phonon-

phonon interreactions increase significantly. For ZrC, the lattice thermal conductivity ($\kappa_N$) was 68 W/m·K at room temperature, and decreased to 7 W/m·K when temperature increased to 2000 K. The trend in the present study consist with a previous experimental result wherein the phonon contribution to thermal conductivity was obtained by taking the experimentally measured total thermal conductivity for $ZrC_x$ with x values approaching 1 and subtracting the electron contribution to thermal conductivity that was calculated using the Wiedemann-Franz law[40]. The total thermal conductivity of $ZrC_x$ increases with increasing temperature, as shown in Figure 1, and the high-temperature thermal conductivity is dominated by electron conductivity. In contrast to simulations, experimental measurements should be considered a lower bound for thermal conductivity because of the presence of grain boundaries, dissolved impurities, second phases, and other features that decrease the measured value compared to the inherent thermal conductivity of the material.

Lattice thermal conductivity can either be limited by extrinsic effects (e.g., isotopes, impurities, point defects, or grain boundary scattering)[65] or intrinsic effects (e.g., phonon-phonon scattering)[66]. Grain size is an extrinsic effect that decreases thermal conductivity because phonons are scattered by grain boundaries[29][67][68], thus lattice thermal conductivity decreases as the number of grain boundaries increases with decreasing grain size[69][70]. To quantify this effect, lattice thermal conductivities with grain sizes of 1 μm, 5 μm and 20 μm were calculated for all compositions as shown in Figure 7. For example, lattice thermal conductivity was 78 W/m·K for ZrC with a grain size of 1 μm, 100 W/m·K for a grain size of 5 μm, and 110 W/m·K for a grain size of 20 μm. Similar trends were also predicted for $ZrC_{0.75}$ and $ZrC_{0.5}$. The calculations correctly

predicted that lattice thermal conductivity decreased with decreasing grain size due to increasing phonon scattering at grain boundaries. However, the magnitude of this effect is not sufficient to explain the lattice thermal conductivity values typically measured experimentally for $ZrC_x$ ceramics.

The presence of mixed isotopes also affects lattice thermal conductivity, resulting in a decrease in thermal conductivity when the natural abundance of isotopes was

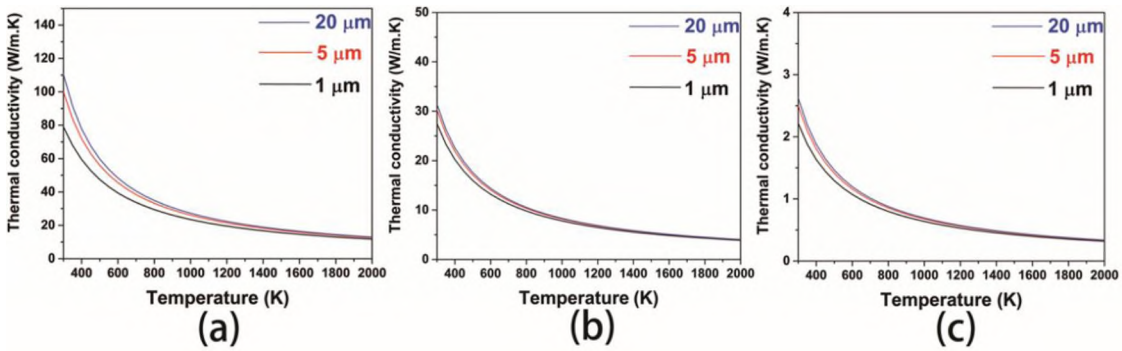


Figure 7. Lattice thermal conductivities of (a) ZrC, (b) $ZrC_{0.75}$ and (c) $Zr_2C$ ($ZrC_{0.5}$) with different grain sizes.

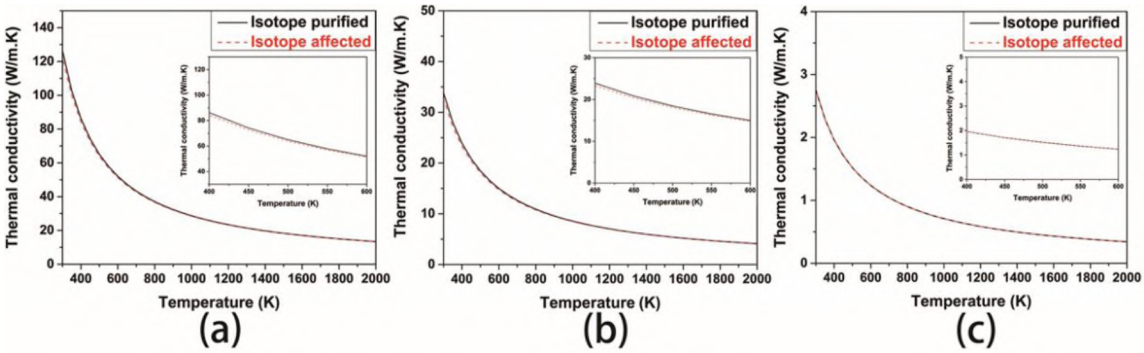


Figure 8. Isotopopically pure and natural abundance isotope lattice thermal conductivities of (a) ZrC, (b) $ZrC_{0.75}$ and (c) $Zr_2C$ ($ZrC_{0.5}$).

considered[71][72][73][74][75][76]. For example, the thermal conductivity of $^{11}B_4{}^{12}C$ was about 15% lower than $^{10}B_4{}^{12}C$ at room temperature[57] and is further lowered when mixtures of isotopes were considered. The heavier isotopes play a critical role in scattering.For some materials that have large mass differences between isotopes, phonon-isotope scattering can dominate the overall thermal conductivity (i.e., overwhelm phonon-phonon scattering) at room or elevated temperatures. For example, the thermal conductivity of GaN with a natural abundance of isotopes is about 33% lower than the isotopically pure GaN at room temperature due to weak anharmonic phonon-phonon scattering[60]. Strong isotope-phonon scattering and weak anharmonic phonon-phonon scattering result in a large isotope effect on the vibrational properties. The isotope effect on lattice thermal conductivity of ZrC was calculated previously[29], which showed that isotope scattering can be the predominant effect in determining lattice thermal conductivity. However, the isotope effect is temperature-dependent and its effectiveness decreases as temperature increases. In the present work, the effect of isotopes on the lattice thermal conductivities of $ZrC_X$ ceramics was minimal as shown in Figure 8. For example, accounting for the natural abundance of Zr isotopes only reduced room temperature lattice thermal conductivity from 126 W/m·K when the effect was not considered to 122 W/m·K when isotope effect was considered. Based on these analyses, isotope scattering is also not sufficient to account for the lower experimental values of thermal conductivity.

### 3.5. MECHANISM OF LOW LATTICE THERMAL CONDUCTIVITY

The combination of the Debye-Calloway model and first principles computations correctly predicted trends for the lattice thermal conductivity of $ZrC_X$ with temperature

and carbon vacancy content. However, the predicted lattice thermal conductivity values for ZrC and $ZrC_{0.75}$ are higher than measured total thermal conductivity values, so additional research will examine other possible mechanisms to explain the differences. As discussed above, part of the difference is due to the effects of defects such as impurities or pores in real materials that reduce the measured thermal conductivity of real materials compared to the inherent value. All of these defects scatter the phonons or otherwise impede thermal transport. Common impurities in zirconium carbide include Hf, O, and N. All Zr-based materials made from commercial Zr sources contain Hf due to its presence in naturally-occurring Zr minerals and the difficulty associated with separating Zr and Hf. The presence of Hf impurities could decrease the thermal conductivity of ZrC significantly. Zirconium carbide also typically contains dissolved O and N that substitute onto carbon vacancy sites. These factors could lower experimental values of thermal conductivity compared to the present results, which do not take those factors into account. Similarly, pores could also reduce the thermal conductivities significantly. $ZrC_x$ samples with lower relative densities have relatively lower thermal conductivities as listed in Table 1 and shown in Figure 1. In addition, the high x value in the bulk $ZrC_x$ sample is 0.98 instead of 1. Thus the measured values are lower than the inherent thermal conductivity, simulations likely overestimate thermal conductivity since not all scattering mechanisms are considered. Future simulations could consider additional factors such as grain boundary resistance or phonon-electron scattering, which may be active in real materials and could reduce the predicted values. Once lattice thermal conductivity values are within the range expected based on experimental studies, then the effects of electron

thermal conductivity can be combined with lattice thermal conductivity predictions to more fully analyze total thermal conductivity of zirconium carbide ceramics.

## 4. CONCLUSION

The lattice thermal conductivities have been predicted for $ZrC_x$ with different carbon vacancy contents (ZrC, $ZrC_{0.75}$ and $ZrC_{0.5}$). Phonon frequencies were calculated as a function of Brillouin zone direction using the finite displacement method. In addition, the Grüneisen parameters, Debye temperatures, and group velocities were determined. The properties calculated from first principles predictions are consistent with other studies and were subsequently used as inputs to the Debye-Callaway model to determine lattice thermal conductivity. The lattice thermal conductivities of $ZrC_x$ with different carbon vacancy contents all decrease as temperature increases due to the effect of phonon-phonon scattering. Lattice thermal conductivities of $ZrC_x$ also decreased with increasing carbon vacancy content because increasing carbon vacancy content decreases the vibration frequencies, which causes a decreased ability to transport heat. Thus, $ZrC_x$ can be tailored from a thermal dissipating material with $x \approx 1$ to a thermal insulating material when $x=0.5$, which opens a new window to tune the thermal conductivity of $ZrC_x$ through carbon vacancy control. The effects of the natural distribution of Zr isotopes, grain boundaries, and phonon-phonon interactions all decrease the lattice thermal conductivities for all of the compositions studied in this work. While these calculations correctly predict the trends in lattice thermal conductivity with temperature, the magnitudes of the values predicted for ZrC are higher than experimentally measured

total thermal conductivity values. Hence, future research will focus on incorporating additional mechanisms to account for differences between predicted lattice thermal conductivity values and those typically measured for $ZrC_x$ ceramics.

## ACKNOWLEDGEMENT

The present research project was supported by the Ceramics Program in the U.S. National Science Foundation (DMR 1742086). The computational efforts, for the first principle calculations, were assisted by the National Supercomputing Center in Shenzhen, China.

## REFERENCES

[1]S. Ueta, J. Aihara, A.Yasuda, H. Ishibashi, T. Takayama, K. Sawa. J. Nucl. Mater. 376(2008) 146-151.

[2]G.D. Del Cui, C.W. Forsberg, W.S. Rickman, ORNL. 27 (2002)4-00.

[3]E. López-Honorato, J. Tan, P.J. Meadows, G. Marsh, P. Xiao. J. Nucl. Mater. 392(2009)219-224.

[4]T. Ogawa, K. Ikawa. J. Nucl. Mater.98(1981)18-26.

[5]G. Newsome, L.L. Snead, T. Hinoki, Y. Katoh, D. Peters. J. Nucl. Mater. 371(2007)76-89.

[6]L.L. Snead, Y. Katoh, S. Kondo. J. Nucl. Mater. 399(2010)200-207.

[7]G.M. Song, Y.J. Wang, Y.Zhou. J.Mater.Sci. 36(2001)4625-4631.

[8]Q. Tong, J. Shi, Y. Song, Q. Guo, L. Liu. Carbon. 42(2004)2495-2500.

[9]M.B. Dickerson, P.J. Wurm, J.R. Schorr, W.P. Hoffman, P.G. Wapner, K.H. Sandhage. J.Mater.Sci. 39(2004)6005-6015.

[10] X.T. Shen, L. Liu, W. Li, K.Z.Li. Ceram. Int. 41(2015)11793-11803.

[11] Q Liu, J Liu, X Luan. J. Mater. Sci. Technol. 35(12)(2019)2942-2949.

[12] C.C. Sorrell, V.S. Stubican, R.C.Bradt. J. Am. Ceram. 69(1986)317-321.

[13] L. Xu, C. Huang, H. Liu, B. Zou, H. Zhu, G. Zhao, J. Wang, Int. J. Refract. Met. Hard Mater. 37(2013)98-105.

[14] Y Xu, W Sun, X Xiong, F Liu, X Luan. J. Mater. Sci. Technol. 35(12)(2019):2785-2798.

[15] R.E. Taylor J. Am. Ceram. Soc. 45(1962)74-78.

[16] B. Wei, L. Chen, Y. Wang et al. J. Eur. Ceram. Soc. 38(2018)411-419.

[17] X. Wei, C. Back, O. Izhvanov, C. Haines, E. Olevsky. Materials. 9(2016)No.577.

[18] R.E. Taylor, J. Morreale. J. Am. Ceram. Soc. 47(1964)69-73.

[19] L.N. Grossman. J. Am. Ceram. Soc. 48(1965)236-242.

[20] R.V. Sara. J. Am. Ceram. Soc. 48(1965)243-247.

[21] Y. Katoh, G. Vasudevamurthy, T. Nozawa, L.L. Snead. J. Nucl. Mater.441(2013)718-742.

[22] C.W. Xie, A.R. Oganov, D. Li, T.T. Debela, N. Liu, D. Dong, Q.F. Zeng. Phys. Chem. Chem. Phys. 18(2016)No.12299.

[23] Y.H. Zhang, B. Liu, J.M. Wang, J.Y. Wang. Acta Mater. 111(2016)232-241.

[24] J.P Crocombette. J. Phys.: Condens. Matter. 25(2013)No.505501.

[25] L.G. Radosevich, W.S. Williams. J. Am. Ceram. Soc.49(1966)156-159.

[26] R.O. Pohl. Phys. Rev. Lett.8(1962)481.

[27] A.I. Gusev, A.A. Rempel, A.J. Magerl. Disorder and Order in Strongly Nonstoichiometric Compounds. Heidelberg: Springer; 2001.

[28] Y. Zhang, B. Liu, J. Wang. Sci. Rep.5( 2015)18098.

[29] Y. Zhou, T.W. Heitmann, E.Bohannan, J.C. Schaeperkoetter, W.G. Fahrenholtz, G.E. Hilmas. J. Am. Ceram. Soc. 103 (2020)2891-2898.

[30] W. Hu, J. Xiang, Y. Zhang et al. J. Mater. Res. 27(2012)1230-1236.

[31] T.A. Mellan, A. Aziz, Y. Xia, R. Grau-Crespo, A.I. Duff. Phys. Rev B. 99(2019)No.094310.

[32] Y. Zhou, T.W. Heitmann, W.G. Fahrenholtz, G.E. Hilmas. J. Eur. Ceram. Soc.39(2019)2594-2600.

[33] E. Padovano, C. Badini, K. Mergia, J. Barcena. Ceram. Int. 44(2018)15050-15057.

[34] T.H.K. Barron, G.K. White. Heat capacity and thermal expansion at low temperatures. Berlin/Heidelberg, Germany: Springer Science & Business Media; 2012.

[35] P.G. Klemens. Proceedings of the Royal Society of London. Series A. Mathematical and Physical Sciences. 208(1951)108-133.

[36] J. Callaway. Phys. Rev. 113(1959)1046.

[37] H. Xiang, Z. Feng, Z. Li, Y. Zhou. Sci. Rep. 8(2018)No.14374.

[38] H. Xiang, J. Wang, Y. Zhou. J. Eur. Ceram. Soc.39(2019)2982-2988.

[39] Y. Zhang. J. Materiomics.2(2016)237-247.

[40] K. Hirao, Y. Zhou, H. Hyuga, T. Ohji, D. Kusano. J. Korean Ceram. Soc.49(2012)380-384.

[41] Y. Zhou, H. Hyuga, D. Kusano, Y. Yoshizawa, K. Hirao. Adv. Mater.23(2011)4563-4567.

[42] D. Morelli, J. Heremans. Appl. Phys. Lett. 81(2013)8-10.

[43] W. Jones, N.H. March, Theoretical Solid State Physics. London, Great Britain: John Wiley & Sons; 1973.

[44] R.E.Taylor. E.K. Storms. Thermal Transport in Refractory Carbides. In: Klemens PH, Chu TK, eds. Thermal Conductivity 14. New York, NY: Plenum Press; 1975.

[45] D.T. Morelli, J.P. Heremans, G.A. Slack. Phys. Rev. B. 66(2002)No.195304.

[46] Asen-Palmer M, Bartkowski K, Gmelin E et al. Phys. Rev. B. 1997;56(15)9431.

[47] Lindsay L, Broido DA, Reinecke TL. Phys. Rev. B.2013;88(14)144306.

[48] Xiang H, Feng Z, Li Z, Zhou Y. Sci. Rep. 8(2018)No.14374.

[49] Morelli DT, Heremans JP, Slack GA. Phys. Rev. B.2002;66(19):195304.

[50] G. Grimvall, Thermophysical properties of materials. Amsterdam, Netherlands: Elsevier; 1999.

[51] P.G. Klemens. Proceedings of the Physical Society. Section A. 68(1955)1113.

[52] E.S. Toberer, A. Zevalkink, G.J. Snyder. J. Mater. Chem. 21(2011)15843-15852.

[53] W. Hu, J. Xiang, S. Liu, Y. Zhang, C. Chen, P. Wang, H. Wang. Inorganic chemistry. 51(2012)5164-5172.

[54] P. Giannozzi et al. J.Phys.:Condens.Matter 21, 395502 (2009).

[55] B.G. Pfrommer, M. Côté, S.G. Louie, M.L. Cohen. J. Comput. Phys.131(1997)233-240.

[56] D. Vanderbilt Phys. Rev B.41(1990)No.7892.

[57] J.P. Perdew, K. Burke, and M. Ernzerhof, Phys. Rev. Lett. 77 (1996) 3865-3868.

[58] H.J. Monkhorst, J.D. Pack . Phys. Rev B.13(1976)5188.

[59] W. Voigt Lehrbuch der Kristallohysic. Teubner, Leipzig, Germany, 1928.

[60] X. Chen, H. Niu, D. Li, Y. Li. Intermetallics. 19(2011)1275-1281.

[61] X. Gonze. Phys. Rev B. 55(1997)No.10337.

[62] Jackson HF, Lee WE. Properties and characteristic of ZrC. In: Konings R, Stoller Volume 2 in Comprehensive nuclear materials. Amsterdam, Netherland: Elsevier; 2012:339-372.

[63] H. Li, L. Zhang, Q. Zeng et al. Solid State Commun. 151( 2011)602-606.

[64] G. Lan, B. Ouyang. J. Song Acta Mater. 91( 2015)304-317.

[65] T. Wang, J. Carrete, A. van Roekeghem, N. Mingo, G.K.H. Madsen. Physical Review B. 95(2017)No.245304.

[66] J.M. Ziman. Electrons and phonons: the theory of transport phenomena in solids. Oxford, United Kingdom: Oxford university press; 2001.

[67] H.J. Goldsmid, A.W. Penn, Phys. Lett. A.27(1968)523-524.

[68] J.E. Parrott. J. Phys. C: Solid State Phys. 2(1969)147.

[69] N. Savvides, H.J. Goldsmid. J. Phys. C: Solid State Phys. 13(1980)4657-4670.

[70] D.M. Rowe, C.M. BhandariAppl. Phys. Lett.47(1985)255-257.

[71] Y. Arita, Y. Nishi, M. Amaya, T. Matsui Thermochim. Acta. 352( 2000)39-42.

[72] S. Chen, Q. Wu, C. Mishra et al. Nat. Mater.11(2012)203-207.

[73] L. Lindsay, D.A. Broido, T.L. Reinecke. Phys. Rev. Lett.,109(2012)No.095901.

[74] L. Lindsay, D.A. Broido, T.L. Reinecke. Phys. Rev B., 87(2013)No.165201.

[75] X. Li, J. Chen, C. Yu, G. Zhang. Appl. Phys. Lett. 103(2013)No.013111.

[76] L. Lindsay, D.A. Broido, T.L. Reinecke. Phys. Rev B, 88(2013)144306.

# IV. ELECTRONIC STRUCTURE AND THERMAL CONDUCTIVITY OF ZIRCONIUM CARBIDE WITH HAFNIUM ADDITIONS

Yue Zhou, William G. Fahrenholtz, Joseph Graham, Gregory E. Hilmas

*Department of Materials Science and Engineering, Missouri University of Science and Technology, Rolla, MO 65409, USA*

## ABSTRACT

The lattice thermal conductivity of ZrC with different Hf contents was investigated theoretically. The band structures, density of states, and electron density differences were calculated for ZrC and (Zr,Hf)C containing 3.125 at% or 6.25 at% Hf . The electronic structure did not change significantly with Hf additions. Lattice thermal conductivities were calculated for all of the compositions by combining first-principles calculations with the Debye-Callaway model. The theoretical lattice thermal conductivity of ZrC was 68 $Wm^{-1}K^{-1}$ at room temperature. When adding 3.125 at% and 6.25 at% Hf into ZrC, lattice thermal conductivity decreased to 18 $Wm^{-1}K^{-1}$ and 21 $Wm^{-1}K^{-1}$, respectively. With the addition of Hf impurities, the frequency of the acoustic phonons decreased, which resulted in decreases in the Debye temperature and lattice thermal conductivity.

***Keywords:*** Zirconium carbide; Lattice thermal conductivity; Theoretical study; First-principle calculations.

# 1. INTRODUCTION

Zirconium carbide is a promising material for potential use in tri-structural isotropic (TRISO) fuel particles[1] that will be used in advanced high temperature nuclear reactors[2][3]. The coolant outlet temperature of the Very High Temperature Reactor concept is around 1000 °C. To optimize the performance of TRISO fuel particles, zirconium carbide is being considered as an alternative to the silicon carbide layer. Zirconium carbide is structurally stable at the predicted operating temperatures and has favorable thermal conductivity, fission product retention characteristics, and radiation damage resistance. Zircon (nominally $ZrSiO_4$) is a naturally occurring mineral and is the principal raw material used in the commercial production of zirconium. Typically, zircon contains about 2 wt% of hafnium[4]. In practice, separating hafnium from zirconium is difficult since they have similar atomic radii, valence electron configurations, and chemical properties[5]. Therefore, Hf impurities are an important defect in ZrC and other zirconium compounds.

Solid solution additions generally decrease the thermal conductivities of the resulting alloys. The thermal conductivity of Ge-Si alloys is lower than that for either pure element[6]. For example, the thermal conductivity of $Si_{0.7}Ge_{0.3}$ is about 6.3 $Wm^{-1}K^{-1}$, which is lower than either pure Si, about 88 $Wm^{-1}K^{-1}$, or pure Ge, about 50 $Wm^{-1}K^{-1}$. Thermal conductivities of Mg alloys also decrease as the amount of alloying increases[7][8][9][10][11]. Likewise, the thermal conductivity of (Zr,Hf)NiSn half-Heusler alloys decreases when Ti is substituted onto the (Zr,Hf) sites, or by substituting Sb onto Sn sites[12]. Solid solutions of yttria-stabilized hafnia-zirconia have lower thermal

conductivities than either yttria-stabilized zirconia (YSZ) or yttria-stabilized hafnia end members. Replacement of $Zr^{4+}$ ions on the zirconia sublattice with $Hf^{4+}$ ions decreases the phonon mean free path[13]. For Al alloys, thermal conductivities of binary Al alloys (Al-Si, Al-Cu, Al-Fe and Al-Mg) are all lower than 99.8 % pure Al[14]. The thermal conductivity of Al-Cu decreases as Cu content increases due to the formation of $Al_2Cu$ at interfaces and the resulting scattering of electrons and phonons[15]. The thermal conductivity of Al-Si foundry alloys decreases due to the addition of the main alloying elements of Si, Cu, and Ni[16]. Some theoretical studies found that solid solutions of $Mg_2Si_xSn_{1-x}$ had bulk thermal conductivities that were smaller than bulk $Mg_2Si$ and bulk $Mg_2Sn$[17]. Similarly, lattice thermal conductivities of $Ti_xHf_{1-x}NiSn$ and $Zr_xHf_{1-x}NiSn$ half-Heusler alloys are lower than those for TiNiSn, ZrNiSn and HfNiSn due to the mass disorder effect[18].

Thermal conductivities of ceramic solid solutions have been studied experimentally. Thermal conductivities of high entropy carbides and high entropy borides are lower than the constituent transition metal carbides and borides[19][20][21][22]. The thermal conductivity of YSZ can be reduced by decreasing the grain size[23] and by doping with rare-earth oxides[24]. The thermal conductivity of Si also decreases with decreasing grain size (i.e., increasing density of grain boundaries) and due to increasing impurity content, both of which scatter phonons[25][26]. Irradiation has been shown to reduce the thermal conductivity of $CeO_2$[27], SiC, $Al_2O_3$, $MgAl_2O_4$, AlN, $Si_3N_4$ and BeO[28] due to defect formation. Grain boundaries of $Y_3Al_5O_{12}$ also scatter phonons and reduce thermal conductivity[29]. Theory-based analysis provides an excellent complement to experimental results and can help provide insight into mechanisms controlling the

observed behavior. Several recent studies have used the Debye-Callaway model with parameters determined from first-principles calculations to calculate lattice thermal conductivity for materials including selenium compounds[30], γ-$Si_3N_4$, γ-$Ge_3N_4$[31] and $ZrB_2$[32]. Previous experimental studies of the thermal conductivity of ZrC have resulted in values that range from about 26 $Wm^{-1}K^{-1}$ to 42 $Wm^{-1}K^{-1}$ at around 1500 K without a systematic explanation of the reasons for the differences[33].

The purpose of this paper is to use theoretical methods to study the effect of hafnium content on the electronic structure and lattice thermal conductivity of (Zr,Hf)C solid solutions. Note that some of the results for pure ZrC used for comparison in the present study were from our previous study of the effect of carbon vacancy content on the thermal properties of $ZrC_x$ ceramics[34]. The previously published results are shown in Figures 1a, 7a, and 8a as well as in Table 1.

## 2. CALCULATION METHODS

### 2.1. FIRST-PRINCIPLE CALCULATIONS

The valence electron configurations are $4d^25s^2$ for zirconium, $5d^26s^2$ for hafnium and $2s^22p^2$ for carbon. The crystal structure of ZrC is rock salt (Space group: $Fm\bar{3}m$, No. 225) with an initial lattice constant of 4.699 Å before geometry optimization as shown in Figure 1a. The atom coordinates are (0, 0, 0) for Zr and (0, 0.5, 0) for C with other atom positions generated based on the rock salt symmetry. To investigate the effect of Hf impurities on the electronic structure and thermal properties of ZrC, 2×2×2 supercells of $(Zr_{1-x}Hf_x)C$ with x = 3.125 at%, hereafter written $Zr_{0.97}Hf_{0.03}C$, and x = 6.250 at%,

hereafter written $Zr_{0.94}Hf_{0.06}C$ were built. The supercells were based on the ZrC unit cell with some Zr atoms replaced by Hf as shown in Figure 1b and c. The Hf atom positions were assigned to ensure that the structures of the supercells retained the point group symmetry of pure ZrC. The equilibrium crystal structures were optimized using the

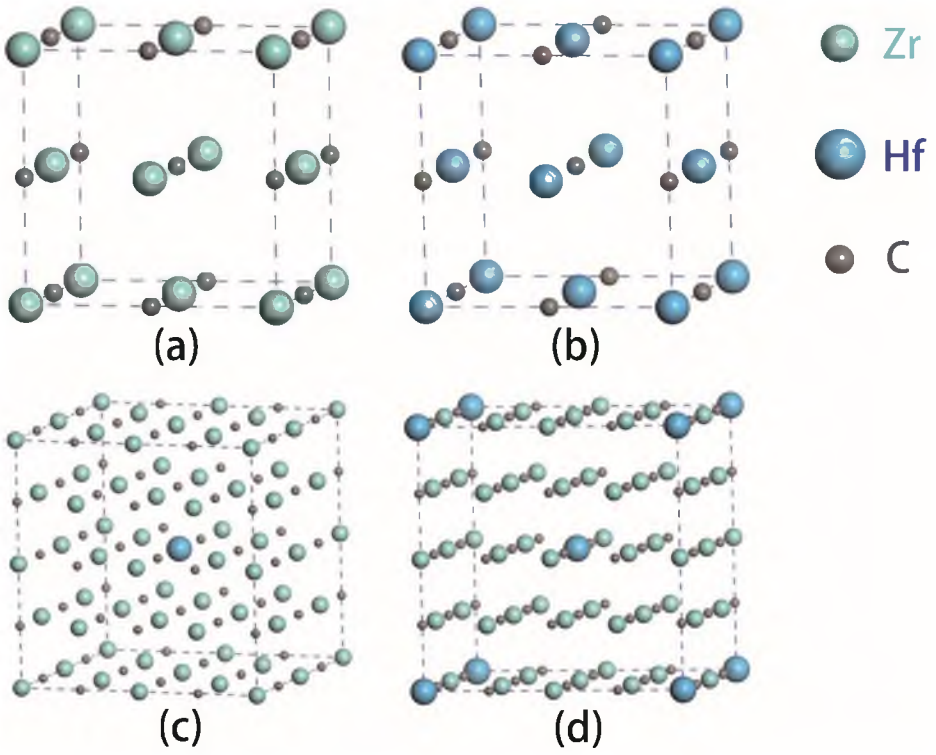


Figure 1. Unit cells of (a) ZrC and (b) HfC, and supercells of ZrC with (c) 3.125 at% Hf ($Zr_{0.97}Hf_{0.03}C$) and (d) 6.25 at% Hf ($Zr_{0.94}Hf_{0.06}C$).

Broyden-Fletcher-Goldfarb-Shanno (BFGS) methodology[35]. The band structures, density of states, electron density differences, and phonon dispersion curves were calculated from first principles using density function theory (DFT; Quantum Expresso)[36]. Interactions between the ionic cores and the valence electrons were represented by Vanderbilt-type ultrasoft pseudopotentials[37]. The generalized-gradient

approximation (GGA)[38] based on the Perdew-Burke-Ernzerhof (PBE) scheme was employed to treat the exchange-correlation energy. A plane-wave cut-off energy of 70 Ry was set after convergence tests. A separation of 0.04 $Å^{-1}$ was selected for the k-point mesh in the Brillouin zone according the Monkhorst-Pack method[39]. Lattice parameters and internal atom positions were optimized assuming the total energy was $5\times10^{-6}$ eV/atom and a maximum ionic displacement of $5\times10^{-4}$ Å. Phonon dispersion curves were calculated using density function perturbation theory[40].

## 2.2. LATTICE THERMAL CONDUCTIVITY CALCULATIONS

Lattice thermal conductivities ($\kappa_l$) were calculated at different temperatures using the Debye-Callaway model[41]. Two transverse ($\kappa_{TA1}$ and $\kappa_{TA2}$) and one longitudinal ($\kappa_{LA}$) acoustic phonon modes contributed to the total lattice thermal conductivity ($\kappa_l$) as expressed by Equation 1:

$$\kappa_l = \kappa_{TA1} + \kappa_{TA2} + \kappa_{LA} \tag{1}$$

In the present study, the contributions of optical phonons to lattice thermal conductivity were ignored due to the low group velocities of the optical phonons, which result in lower contributions to thermal conductivity than for acoustic modes[42][43][44]. Each of the acoustic branches ($\kappa_i$, where $i$ represents $TA1$, $TA2$, and $LA$) give rise to Debye-Callaway terms, which are expressed as:

$$\kappa_{i1} = \frac{1}{3}\frac{k_B^4 T^3}{2\pi^2\hbar^3 v_i}\int_0^{\frac{\theta_i}{T}} \frac{\tau_C^i(x)x^4e^x}{(e^x-1)^2}dx \tag{2}$$

$$\kappa_{i2} = \frac{1}{3}\frac{k_B^4 T^3}{2\pi^2\hbar^3 v_i}\frac{\left[\int_0^{\frac{\theta_i}{T}} \frac{\tau_C^i(x)x^4e^x}{(e^x-1)^2}dx\right]^2}{\int_0^{\frac{\theta_i}{T}} \frac{\tau_C^i(x)x^4e^x}{\tau_N^i(x)\tau_R^i(x)(e^x-1)^2}dx} \tag{3}$$

where $k_B$ is the Boltzmann constant, $\hbar$ is the reduced Planck constant, $v_i$ is the group velocity of the acoustic phonons evaluated at the zone center. $\theta_i$ is the Debye temperature of the acoustic phonons, which is determined from $\theta_i = \hbar\omega_{max}/k_B$, where $\omega_{max}$ represents the maximum frequency of the acoustic phonon branches at the Brillouin zone boundary[30]. The factor $x$ is determined by $x = \hbar\omega/k_BT$. In both Equation 2 and 3, $\tau_C$ is the total relaxation time for all phonon scattering processes. It is a combination of normal (N) and resistive (R) processes. The relaxation time for normal phonon processes is $\tau_N$ while $\tau_R$ is the sum of all the resistive scattering processes. Then, the total scattering rate is the sum of normal and resistive scattering rates, $\tau_C^{-1} = \tau_N^{-1} + \tau_R^{-1}$. The relaxation time for resistive processes is the sum of contributions from isotope scattering ($\tau_I^{-1}$), grain boundary scattering ($\tau_B^{-1}$) and Umklapp scattering ($\tau_U^{-1}$). Isotope scattering arises from random mass variations (from multi-isotope elements) at an atomic site in an otherwise perfect crystal. The scattering rate for isotope scattering can be expressed as[45]:

$$\left[\tau_I^i\right]^{-1} = \frac{Vk_B^4\Gamma}{4\pi\hbar^4 v_L^3}x^4T^4 \tag{4}$$

where $\Gamma$ is the phonon-scattering parameter of the mass-fluctuation as determined by:

$$\Gamma = \sum_j c_j\left[\frac{m_j-\bar{m}}{\bar{m}}\right]^2 \tag{5}$$

with

$$\bar{m} = \sum_j c_j m_j \tag{6}$$

$c_j$ and $m_j$ are the natural abundances and masses of the constituent isotopes.

Grain boundary scattering is related to the phonon transit time between regularly spaced grain boundaries:

$$\left[\tau_B^i\right]^{-1} = \frac{v_i}{d} \tag{7}$$

where $d$ is the effective grain size. The grain boundary scattering rate is independent of

temperature. The Umklapp scattering rate can be expressed as[46]:

$$\left[\tau_U^i\right]^{-1} = \frac{\hbar\gamma_i^2}{Mv_i^2\theta_i}\left(\frac{k_B}{\hbar}\right)^2 x^2T^3exp\left(\frac{-\theta_i}{3T}\right) \quad (8)$$

where $M$ is the average mass of atoms in the structure, $\gamma_i$ is the Grüneisen parameter of the acoustic phonon branch which is calculated by[47]:

$$\gamma_i = \frac{\sum\gamma_{i,q}C_i(q)}{\sum C_i(q)} \quad (9)$$

where $\gamma_{i,q}$ is the mode resolved Grüneisen parameter for mode $i$ at wave vector $q$ which is determined by:

$$\gamma_{i,q} = -\frac{\partial ln\omega_{i,q}}{\partial lnV} \quad (10)$$

where $V$ is the volume of the unit cell. In Equation 9, $C_i(q)$ is expressed as:

$$C_i(q) = k_B\left(\frac{\hbar\omega_{i,q}}{k_BT}\right)^2\frac{exp\left(\frac{\hbar\omega_{i,q}}{k_BT}\right)}{\left[exp\left(\frac{\hbar\omega_{i,q}}{k_BT}\right)-1\right]^2} \quad (11)$$

The group velocities of the acoustic phonons are determined as:

$$v_g(i,q) = \frac{\partial\omega(i,q)}{\partial q} \quad (12)$$

where the directional derivative of the dispersion is taken in the [100]. Low energy acoustic phonons have dispersion surfaces that are approximately conical. Therefore, group velocity is treated as isotropic.

## 3. RESULTS AND DISCUSSION

### 3.1. ELECTRON STRUCTURES

The band structure of pure ZrC is shown in Figure 2a. The bands below about -8 eV have primarily C 2*s* and Zr 4*d* character with Zr 4*p*, Zr 5*s*, and C 2*p* states also having

small contributions. The bands above -6 eV are of primarily C 2*p*, Zr 4*p* and Zr 4*d* character. At the Fermi level, the valence and conduction bands overlap at the Γ point, indicating that metallic bonding is present in ZrC and that ZrC should exhibit metallic conductivity.

The band structures of $Zr_{0.97}Hf_{0.03}C$ and $Zr_{0.94}Hf_{0.06}C$ are shown in Figure 2b and c. Valence bands and conduction bands overlap for both compositions, which indicates metallic bonding and electronic conductivity similar to ZrC.

The density of states for ZrC is shown in Figure 3a. A non-zero density of states at the Fermi level confirms the presence of metallic bonding in ZrC. From the partial density of states curves, the states at the Fermi level are mostly from the Zr 4*d* and C 2*p* states, demonstrating that the main contribution to electrical conductivity is from these states. In addition, an obvious gap is present from -8 eV to -6 eV below the Fermi level, indicating strong hybridization of electron orbitals. From the partial density of states of Zr, the Zr 5*s*, Zr 4*p*, and Zr 4*d* orbitals are in the same energy range due to $d^2sp^3$ hybridization from the $Zr_6$ octahedra present in ZrC. The lowest lying states from -11.4 eV to -8.1 eV are mostly from quasi-core C 2*p* with small contributions from Zr 5*s*, Zr 4*p* and Zr 4*d* bands and they are not involved in chemical bonding. The states from -5.6 eV to -1.7 eV are mainly from overlapping C 2*p* and Zr $4d^2sp^3$ orbitals, which form covalent bonds.

The density of states for $Zr_{0.97}Hf_{0.03}C$ and $Zr_{0.94}Hf_{0.06}C$ are shown in Figures 3b and 3c. The partial density of states for Hf are very similar to Zr in both compositions.

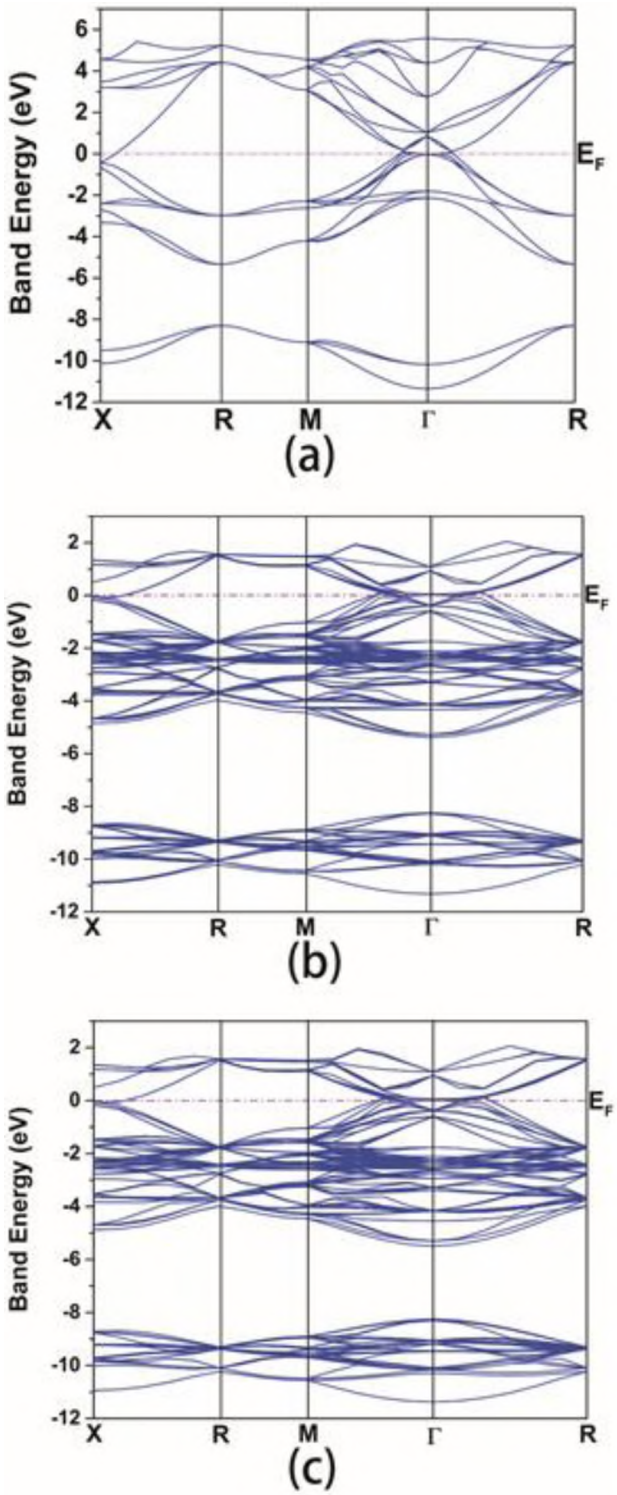


Figure 2. Band structures of (a) a primitive cell of pure ZrC, and supercells for (b) $Zr_{0.97}Hf_{0.03}C$, and (c) $Zr_{0.94}Hf_{0.06}C$.

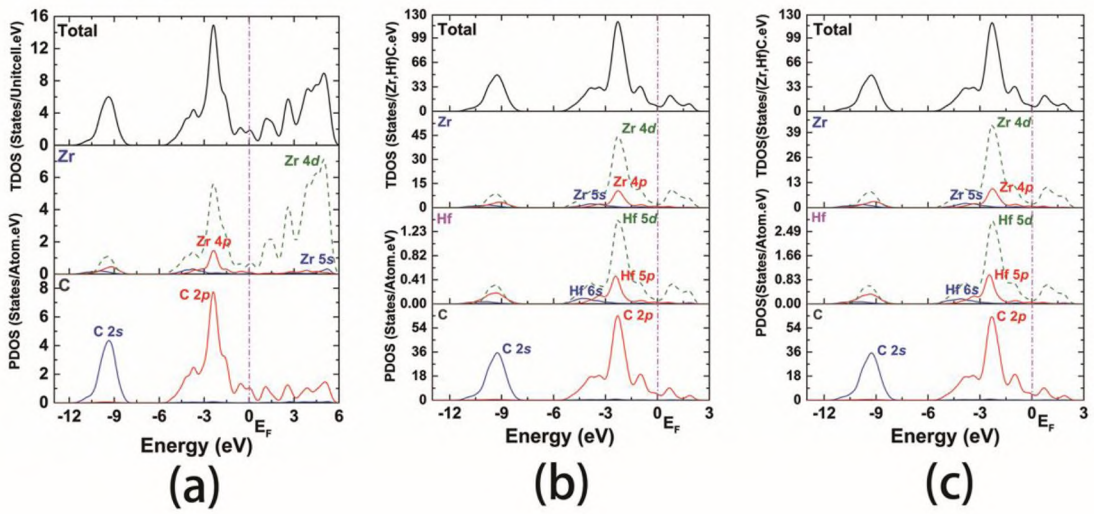


Figure 3. Density of states of (a) pure ZrC, (b) $Zr_{0.97}Hf_{0.03}C$ and (c) $Zr_{0.94}Hf_{0.06}C$.

Thus, the bonding properties of ZrC are not changed significantly when Hf is present in solid solution.

Electron density difference maps for ZrC are shown in Figure 4. The (100) and (111) planes were selected to study Zr – C and Zr – Zr bonds. On the (100) plane (Figure 4a), strong overlap was obvious between the Zr $4de_g$ and C $2p_i$ (i represents the x, y and z directions) orbitals, which indicates that strong covalent bonds form between Zr and C atoms. In addition, the electron densities close to C atoms are higher than that around Zr atoms, which indicates charge transfer from Zr to C. In other words, the bonds between Zr and C atoms have both covalent and ionic character. Typical metallic bonds between Zr atoms result in the triangular-shaped regions of higher electron density seen between Zr atoms on the (111) plane of ZrC (Figure 4b).

Figure 5 and 6 show the electron density difference maps for $Zr_{0.97}Hf_{0.03}C$ and $Zr_{0.94}Hf_{0.06}C$. The (002) planes were selected since these planes contain Zr, Hf and C atoms in both supercells. No significant differences were observed in the covalent-ionic

bonds between Hf and C compared to the bonds between Zr and C atoms. Similar to ZrC, the (111) planes were selected to view the electron density differences between Zr – Zr and Zr – Hf pairs. The metallic bonds in $Zr_{0.97}Hf_{0.03}C$ and $Zr_{0.94}Hf_{0.06}C$ are similar to those in ZrC. Electron density difference maps indicate that the addition of Hf does not

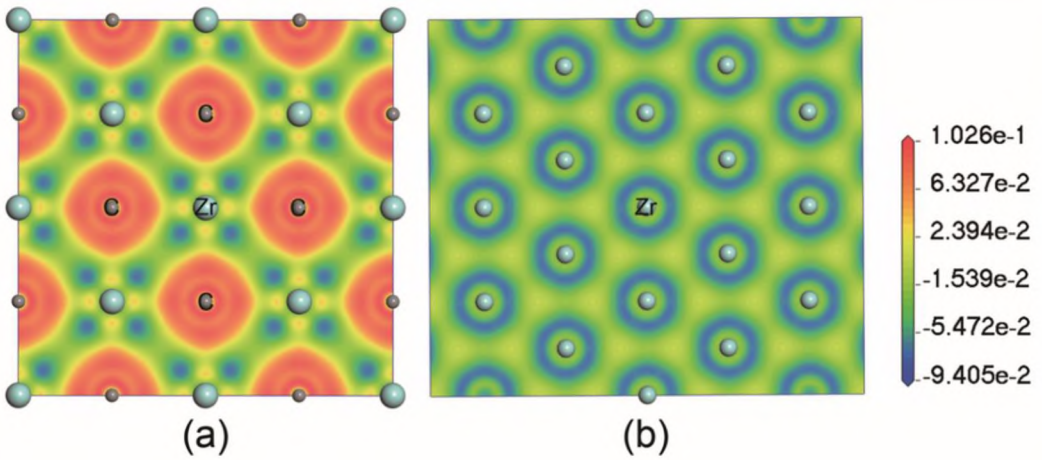


Figure 4. Electron density difference plots of ZrC for the (a) (100) plane and (b) (111) plane.

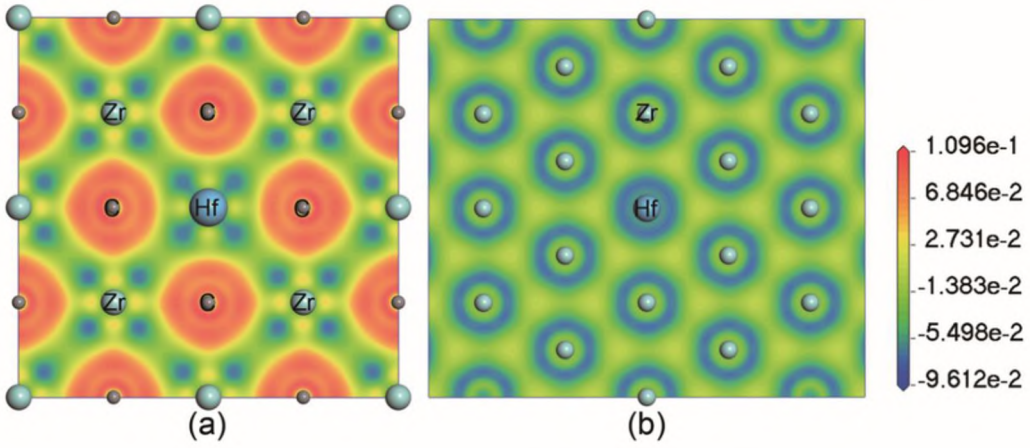


Figure 5. Electron density difference plots of $Zr_{0.97}Hf_{0.03}C$ for the (a) (002) plane and (b) (111) plane.

significantly change the electron structure of $Zr_{0.97}Hf_{0.03}C$ or $Zr_{0.94}Hf_{0.06}C$ compared to ZrC.

### 3.2. PHONON DISPERSION AND GROUP VELOCITY

Phonon dispersion curves and group velocities for ZrC, HfC, $Zr_{0.97}Hf_{0.03}C$, and $Zr_{0.94}Hf_{0.06}C$ are shown in Figure 7. ZrC and HfC have six phonon branches since the primitive cells contain one Zr or Hf atom and one C atom. The low frequency branches (below 10 THz for ZrC and 8 THz for HfC) are acoustic phonons (colored lines) and the high frequency branches (above 10 THz for ZrC and 8 THz for HfC) are optical phonons (black lines). The gaps between the acoustic and optical phonon branches for ZrC (5.6 THz at the Γ point) and HfC (10.3 THz at the Γ point) were attributed to anisotropic bonding and the mass difference between the Zr and C atoms in ZrC, and between the Hf and C atoms in HfC[48]. With the addition of Hf into the ZrC lattice, the low

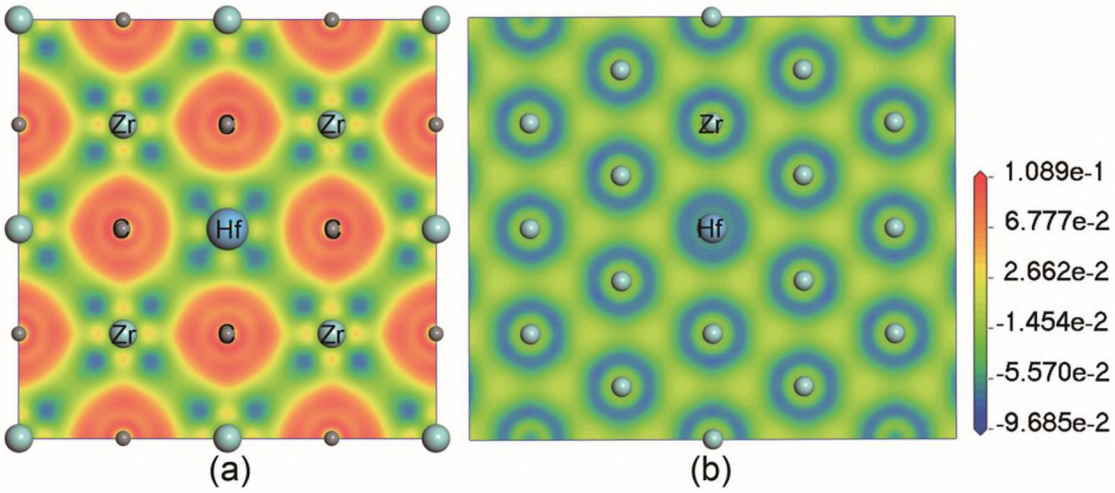


Figure 6. Electron density difference plots of $Zr_{0.94}Hf_{0.06}C$ for the (a) (011) plane and (b) (111) plane.

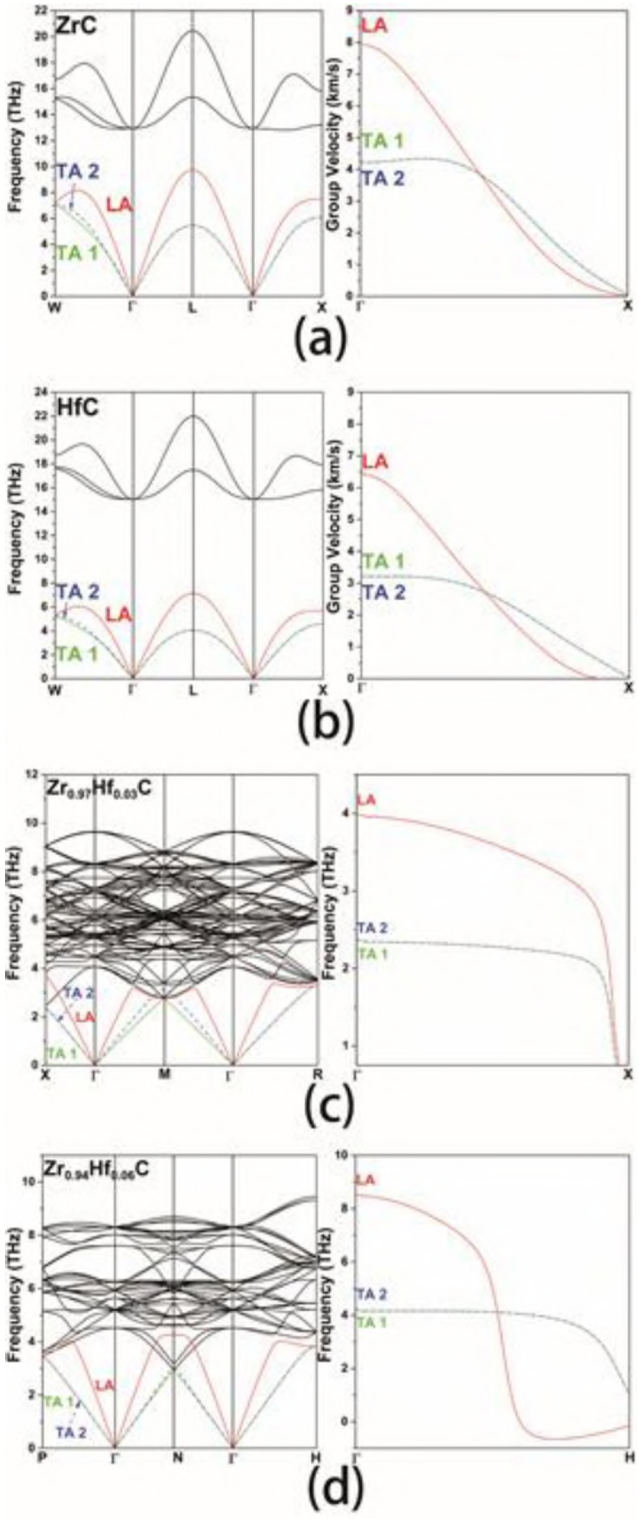


Figure 7. Phonon dispersions and group velocities of (a) ZrC and (b) HfC, (c) $Zr_{0.97}Hf_{0.03}C$ and (d) $Zr_{0.94}Hf_{0.06}C$.

frequency optical phonon branches overlap with the acoustic phonon branches as shown in Figures 7c and7d due to the scattering of the optical phonons by Hf atoms.

Group velocities were calculated for the acoustic phonons for all compositions. The group velocities are shown in Figure 7 beside the corresponding phonon dispersion curves and of the acoustic phonons according to Equation 12. Similarly, the initial addition of 3 at% of Hf into the ZrC lattice decreased the group velocities compared to pure ZrC (for the values are compiled in Table 1. Group velocities of HfC ($v_{TA1}$ = 3.23 km/s, $v_{TA2}$ = 3.23 km/s and $v_{LA}$ = 6.43 km/s) are lower than the corresponding group velocities in ZrC ($v_{TA1}$ = 4.24 km/s, $v_{TA2}$ = 4.24 km/s and $v_{LA}$ = 7.97 km/s). HfC has lower group velocities because of the lower acoustic phonon frequencies, which reduce the slope$Zr_{0.97}Hf_{0.03}C$, $v_{TA1}$ = 2.37 km/s, $v_{TA2}$ = 2.37 km/s and $v_{LA}$=3.99 km/s). When the Hf content increased to 6 at%, group velocities increased (for $Zr_{0.94}Hf_{0.06}C$, $v_{TA1}$ = 4.21 km/s, $v_{TA2}$ = 4.21 km/s and $v_{LA}$ = 8.54 km/s). Higher group velocities of $Zr_{0.94}Hf_{0.06}C$ reflect the higher acoustic phonon frequencies compared to $Zr_{0.97}Hf_{0.03}C$ as shown in Figure 7. The contributions of the optical phonon branches to the group velocities were ignored due to their low values compared to the contributions of the acoustic branch, especially for $Zr_{0.97}Hf_{0.03}C$. Lattice thermal conductivity is proportional to the square of phonon group velocity, which can be expressed as $K_s(\omega) = C_s(\omega)V_g(\omega)^2\tau(\omega)$[ii]. Reduction of group velocity will, therefore, decrease lattice thermal conductivity.

### 3.3. DEBYE TEMPERATURE

Debye temperatures were determined from the maximum acoustic phonon frequencies (two transverse and one longitudinal) at the Brillouin zone boundaries. The Debye temperature for HfC ($\theta_{TA1}$ = 253 K, $\theta_{TA2}$ = 253 K, $\theta_{LA}$ = 343 K) were lower than those for ZrC ($\theta_{TA1}$ = 340 K, $\theta_{TA2}$ = 340 K, $\theta_{LA}$ = 467 K) as shown in Table 1. The lower Debye temperature of HfC was due to the lower acoustic phonon frequencies. The addition of 3 at% Hf into ZrC reduced the Debye temperature (for $Zr_{0.97}Hf_{0.03}C$, $\theta_{TA1}$ = 158 K, $\theta_{TA2}$ = 158 K, $\theta_{LA}$ = 176 K) due to scattering of acoustic phonons by low lying optical phonons as shown in Figures 7c and 7d. Increasing the Hf content to 6 at% in ZrC increased the Debye temperature (for $Zr_{0.94}Hf_{0.06}C$, $\theta_{TA1}$ = 184 K, $\theta_{TA2}$ = 184 K, $\theta_{LA}$ = 204 K) as presented in Table 1. The elastic constants of $Zr_{0.94}Hf_{0.06}C$ ($c_{11}$ = 470.2 GPa, $c_{12}$ = 101.2 GPa, $c_{44}$ = 156.8 GPa) were higher than $Zr_{0.97}Hf_{0.03}C$ ($c_{11}$ = 467.7 GPa, $c_{12}$ = 101.1 GPa, $c_{44}$ = 156.6 GPa), which means $Zr_{0.94}Hf_{0.06}C$ has stronger chemical bonds.

Table 1. Group velocities, Debye temperature and Grüneisen parameters of ZrC, HfC, $Zr_{0.97}Hf_{0.03}C$ and $Zr_{0.94}Hf_{0.06}C$.

| | $v_{TA1}$ | $v_{TA2}$ | $v_{LA}$ | $\theta_{TA1}$ | $\theta_{TA2}$ | $\theta_{LA}$ | $\gamma_{TA1}$ | $\gamma_{TA2}$ | $\gamma_{LA}$ |
|---|---|---|---|---|---|---|---|---|---|
| Unit / Composition | (km/s) | | | (K) | | | N/A | | |
| ZrC | 4.24 | 4.24 | 7.97 | 340 | 340 | 467 | 1.79 | 1.51 | 1.65 |
| HfC | 3.23 | 3.23 | 6.43 | 253 | 253 | 343 | 1.80 | 1.84 | 1.67 |
| $Zr_{0.97}Hf_{0.03}C$ | 2.37 | 2.37 | 3.99 | 158 | 158 | 176 | 1.72 | 0.47 | 1.68 |
| $Zr_{0.94}Hf_{0.06}C$ | 4.21 | 4.21 | 8.54 | 184 | 184 | 204 | 1.91 | 1.08 | 1.42 |

The stronger chemical bonds increased the acoustic phonon frequency and increased the Debye temperature.

### 3.4. LATTICE THERMAL CONDUCTIVITY

Temperature-dependent lattice thermal conductivities for ZrC, HfC, $Zr_{0.97}Hf_{0.03}C$ and $Zr_{0.94}Hf_{0.06}C$ are shown in Figure 8. The grain size was assumed to be 5 μm (Table 2) for all calculations. In those plots, $k_{UI}$ is the lattice thermal conductivity for isotopically pure ZrC and HfC; $k_{UA}$ is the lattice thermal conductivity with grain boundary effects; and $k_N$ represents the thermal conductivity with grain boundary effects plus Umklapp and normal phonon-phonon scattering processes. At room temperature, lattice thermal conductivities of ZrC were 122 $Wm^{-1}K^{-1}$ for $k_{UI}$, 100 $Wm^{-1}K^{-1}$ for $k_{UA}$ and 68 $Wm^{-1}K^{-1}$ for $k_N$. As discussed in our previous study[33], these values are higher than experimentally measured values for $ZrC_x$ ceramics due to the assumption of no carbon vacancies, no impurities, and no porosity.

The lattice thermal conductivities of HfC ($k_{UI}$ = 83 $Wm^{-1}K^{-1}$, $k_{UA}$ = 68 $Wm^{-1}K^{-1}$ and $k_N$ = 47 $Wm^{-1}K^{-1}$ at room temperature) were lower than ZrC, as expected from the lower group velocities. Typical experimental values for thermal conductivity of $HfC_{0.98}$ range from 20 to 25 $Wm^{-1}K^{-1}$ at temperatures from 25 to 100°C[49]. Analogous as $ZrC_x$, the thermal conductivity of HfC predicted herein is higher than the experimental values, which are reduced by the defects in the sintered products[50][51][52] that are not accounted for in the models.

After adding 3.125 at% of Hf into ZrC, the lattice thermal conductivity decreased compared to pure ZrC or pure HfC. At room temperature, $k_{UI}$ was 33 $Wm^{-1}K^{-1}$, $k_{UA}$ was

28 $Wm^{-1}K^{-1}$, and $k_N$ was 18 $Wm^{-1}K^{-1}$ for $Zr_{0.97}Hf_{0.03}C$. The predicted lattice thermal conductivity values for $Zr_{0.94}Hf_{0.06}C$ at room temperature were $k_{UI}$ = 36 $Wm^{-1}K^{-1}$, $k_{UA}$ = 27 $Wm^{-1}K^{-1}$ and $k_N$ = 21 $Wm^{-1}K^{-1}$, which were almost the same as $Zr_{0.97}Hf_{0.03}C$. Four effects contribute to the decrease in lattice thermal conductivity when Hf is added to ZrC.

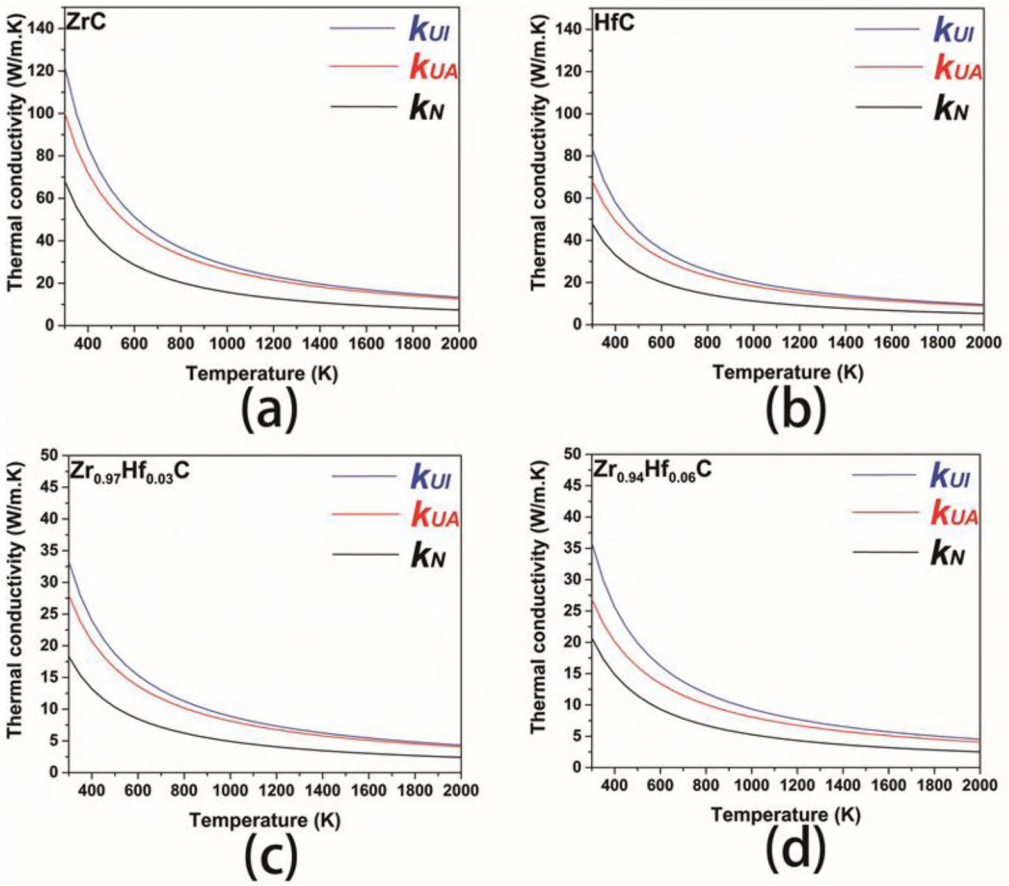


Figure 8. Lattice thermal conductivity of (a) ZrC, (b) HfC, (c) $Zr_{0.97}Hf_{0.03}C$ and (d) $Zr_{0.94}Hf_{0.06}C$. ($k_{UI}$ represents the lattice thermal conductivity which considered as isotope effected; $k_{UA}$ represents the lattice thermal conductivity with isotope and grain boundary effects; $k_N$ represents the thermal conductivity with isotope and grain boundary effects, Umklapp and normal phonon-phonon scattering.)

The first is the decrease in group velocity (Table 1). The spectral thermal conductivity is proportional to the square of the group velocity, $K_s(\omega) = C_s(\omega)V_g(\omega)^2\tau(\omega)$[53], therefore, decreasing group velocity leads to lower lattice thermal conductivity. The second reason is the decrease in Debye temperature (Table 1). According to Equations 2 and 3, decreasing Debye temperature decreases both acoustic and optical phonon thermal conductivities; hence, the total lattice thermal conductivity is also decreased. Third, strain induced by the presence of Hf in the ZrC lattice decreases thermal conductivity. The average Zr – C bond length (which was given after geometry optimization) for ZrC was

Table 2. Average atomic masses, average grain diameters, and average atomic volumes of ZrC, HfC, $Zr_{0.97}Hf_{0.03}C$ and $Zr_{0.94}Hf_{0.06}C$.

| | Average atomic mass (a.u.) | Average diameter (μm) | Average atomic volume (Å$^3$) |
|---|---|---|---|
| ZrC | 51.62 | 5 | 13.02 |
| HfC | 95.25 | 5 | 13.06 |
| $Zr_{0.97}Hf_{0.03}C$ | 52.98 | 5 | 13.04 |
| $Zr_{0.94}Hf_{0.06}C$ | 54.34 | 5 | 13.06 |

2.3524 Å while the average length of Hf – C bonds was 2.3607 Å. After adding 3.125 at% Hf to ZrC, the average Zr – C bond length decreased to 2.3522 Å. Similarly, after adding 6.25 at% Hf to ZrC, the average Zr – C bond length was 2.3519 Å while the average Hf – C bond was 2.3604 Å. The polarization of the bonds increases as the bond length increases due to the strain in the ZrC lattice after adding Hf, which leads to polarization scattering the phonons[54]. The final reason for the decrease in thermal conductivity is the increase in average atomic mass when Hf is added. The average atomic mass increased since Hf has a higher atomic mass than Zr. Increasing average

atomic mass decreases the acoustic phonon frequencies and thereby decreases lattice thermal conductivity.

## 4. CONCLUSION

Electronic structures and lattice thermal conductivities were studied for ZrC and for ZrC containing Hf additions. The addition of Hf did not change the electronic structure of ZrC significantly. The lattice thermal conductivities were calculated with the Debye-Callaway model using Grüneisen parameters, Debye temperatures, and group velocities calculated from first principles. HfC has higher average Grüneisen parameters, lower Debye temperatures, and lower group velocities compared to ZrC. As expected, the lattice thermal conductivity of HfC ($k_N$ = 47 $Wm^{-1}K^{-1}$ at room temperature) was lower than ZrC ($k_N$ = 68 $Wm^{-1}K^{-1}$ at room temperature). The decrease in lattice thermal conductivity with the addition of Hf into the ZrC lattice was attributed to the decrease in frequencies of acoustic phonons, which in turn induced lower the Debye temperatures.

## ACKNOWLEDGEMENT

This research was supported by the Ceramics Program in the Division of Materials Research at the U.S. National Science Foundation (DMR 1742086). The first principles calculations work was conducted with help by National Supercomputing Center in Shenzhen, China.

# REFERENCES

[1]Ueta S, Aihara J, Yasuda A, Hideharu I, Takayama T, Sawa K. Fabrication of uniform ZrC coating layer for the coated fuel particle of the very high temperature reactor. J. Nucl. Mater. 2008; 376(2): 146-151. https://doi.org/10.1016/j.jnucmat.2008.02.068.

[2]Sabharwall P, Bragg-Sitton SM, Stoots C. Energy Convers. Manage. Challenges in the development of high temperature reactors. 2013; 74: 574-581. https://doi.org/10.1016/j.enconman.2013.02.021.

[3]Fütterer MA, Fu L, Sink C, de Groot S, Pouchon M, Kim YW et al. Status of the very high temperature reactor system. Prog. Nucl. Energy. 2014; 77: 266-281. https://doi.org/10.1016/j.pnucene.2014.01.013.

[4]Gambogi J. Zirconium and hafnium. Ind. Miner. 1994:311.

[5] Xu L, Xiao Y, Van Sandwijk A, Xu Q, Yang Y. Production of nuclear grade zirconium: A review. J. Nucl. Mater. 2015; 466: 21-28. https://doi.org/10.1016/j.jnucmat.2015.07.010.

[6]Abeles B, Beers DS, Cody GD, Dismukes JP. Thermal conductivity of Ge-Si alloys at high temperatures. Phys. Rev. 1962; 125(1): 44. https://doi.org/10.1103/PhysRev.125.44.

[7]Rudajevová A, Von Buch F, Mordike BL. Thermal diffusivity and thermal conductivity of MgSc alloys. J. Alloys Compd. 1999; 292(1-2): 27-30. https://doi.org/10.1016/S0925-8388(99)00444-2.

[8]Rudajevova A, Staněk M, Lukáč P. Determination of thermal diffusivity and thermal conductivity of Mg–Al alloys. Mater. Sci. Eng., A. 2003; 341(1-2): 152-157. https://doi.org/10.1016/S0921-5093(02)00233-2.

[9]Pan H, Pan F, Yang R, Peng J, Zhao C, She J et al. Thermal and electrical conductivity of binary magnesium alloys. J. Mater. Sci. 2014; 49(8): 3107-3124. https://doi.org/10.1007/s10853-013-8012-3.

[10] Su C, Li D, Ying T, Zhou L, Li L, Zeng X. Effect of Nd content and heat treatment on the thermal conductivity of MgNd alloys. J. Alloys Compd. 2016; 685: 114-121. https://doi.org/10.1016/j.jallcom.2016.05.261.

[11] Su C, Li D, Luo AA, Ying T, Zeng X. Effect of solute atoms and second phases on the thermal conductivity of Mg-RE alloys: A quantitative study. J. Alloys Compd. 2018; 747: 431-437. https://doi.org/10.1016/j.jallcom.2018.03.070.

[12] Sakurada S, Shutoh N. Effect of Ti substitution on the thermoelectric properties of (Zr, Hf) NiSn half-Heusler compounds. Appl. Phys. Lett. 2005; 86(8): 082105. https://doi.org/10.1063/1.1868063.

[13] Winter MR, Clarke DR. Thermal conductivity of yttria-stabilized zirconia–hafnia solid solutions. Acta Mater. 2006; 54(19): 5051-5059. https://doi.org/10.1016/j.actamat.2006.06.038.

[14] Chen JK, Hung HY, Wang CF, Tang NK. Thermal and electrical conductivity in Al–Si/Cu/Fe/Mg binary and ternary Al alloys. J. Mater. Sci. 2015; 50(16) :5630-5639. https://doi.org/10.1007/s10853-015-9115-9.

[15] Wu J, Zhang H, Zhang Y, Li J, Wang X. Effect of copper content on the thermal conductivity and thermal expansion of Al–Cu/diamond composites. Mater. Des. 2012; 39: 87-92. https://doi.org/10.1016/j.matdes.2012.02.029.

[16] Stadler F, Antrekowitsch H, Fragner W, Kaufmann H, Pinatel EF, Uggowitzer PJ. The effect of main alloying elements on the physical properties of Al–Si foundry alloys. Mater. Sci. Eng.A. 2013; 560: 481-491. https://doi.org/10.1016/j.msea.2012.09.093.

[17] Li W, Lindsay L, Broido DA, Stewart DA, Mingo N. Thermal conductivity of bulk and nanowire $Mg_2Si_xSn_{1-x}$ alloys from first principles. Phys. Rev. B. 2012; 86(17): 174307. https://doi.org/10.1103/PhysRevB.86.174307.

[18] Eliassen SNH, Katre A, Madsen GKH, Persson C, Løvvik OM, Berland K. Lattice thermal conductivity of $Ti_xZr_yHf_{1-x-y}$ NiSn half-Heusler alloys calculated from first principles: Key role of nature of phonon modes. Phys. Rev. B. 2017; 95(4): 045202. https://doi.org/10.1103/PhysRevB.95.045202.

[19] Yan X, Constantin L, Lu Y, Silvain JF, Nastasi M, Cui B. $(Hf_{0.2}Zr_{0.2}Ta_{0.2}Nb_{0.2}Ti_{0.2})$ C high-entropy ceramics with low thermal conductivity. J. Am. Ceram. Soc. 2018; 101(10): 4486-4491. https://doi.org/10.1111/jace.15779.

[20]] Gild Joshua, Wright A, Quiambao-Tomko K, Qin M, Tomko JA, bin Hoque MS et al. Thermal conductivity and hardness of three single-phase high-entropy metal diborides fabricated by borocarbothermal reduction and spark plasma sintering. Ceram. Int. 2020; 46(5): 6906-6913. https://doi.org/10.1016/j.ceramint.2019.11.186.

[21] Dai FZ, Wen B, Sun YJ, Xiang HM, Zhou YC. Theoretical prediction on thermal and mechanical properties of high entropy $(Zr_{0.2}Hf_{0.2}Ti_{0.2}Nb_{0.2}Ta_{0.2})C$ by deep learning potential. J Mater. Sci. Tech. 2020; 43:168-174. https://doi.org/10.1016/j.jmst.2020.01.005.

[22] Dai FZ, Sun YJ, Wen B, Xiang HM, Zhou YC. Temperature Dependent Thermal and Elastic Properties of High Entropy $(Ti_{0.2}Zr_{0.2}Hf_{0.2}Nb_{0.2}Ta_{0.2})B_2$: Molecular Dynamics Simulation by Deep Learning Potential. J Mater. Sci. Tech. 2021; 72: 8-15. https://doi.org/10.1016/j.jmst.2020.07.014.

[23] Yang HS, Bai GR, Thompson LJ, Eastman JA. Interfacial thermal resistance in nanocrystalline yttria-stabilized zirconia. Acta Mater. 2002; 50(9): 2309-2317. https://doi.org/10.1016/S1359-6454(02)00057-5.

[24] Zhu D, Miller RA. Thermal Conductivity and Sintering Behavior of Advanced Thermal Barrier Coatings. Nonmetallic Materials. NASA/TM-2002-211481, NAS 1.15:211481, E-13249. 2002. http://gltrs.grc.nasa.gov/GLTRS.

[25] Wang Z, Alaniz JE, Jang W, Garay JE, Dames C. Thermal conductivity of nanocrystalline silicon: importance of grain size and frequency-dependent mean free paths. Nano Lett. 2011;11(6):2206-2213. https://doi.org/10.1021/nl1045395.

[26] Bux SK. Synthesis and characterization of bulk nanostructured semiconductors for thermoelectric applications. Adv. Funct. Mater. 2009; 19(25): 2445-2452.

[27] Khafizov M, Pakarinen J, He L, Hurley DH. Impact of irradiation induced dislocation loops on thermal conductivity in ceramics. J. Am. Ceram. Soc. 2019; 102(12): 7533-7542. https://doi.org/10.1111/jace.16616.

[28] Snead LL, Zinkle SJ, White DP. Thermal conductivity degradation of ceramic materials due to low temperature, low dose neutron irradiation. J. Nucl. Mater. 2005; 340(2-3): 187-202. https://doi.org/10.1016/j.jnucmat.2004.11.009.

[29] Bisson JF, Yagi H, Yanagitani T, Kaminskii A, Barabanenkov YN, Ueda KI et al. Influence of the grain boundaries on the heat transfer in laser ceramics. Opt. Rev. 2007; 14(1): 1-13. https://doi.org/10.1007/s10043-007-0001-9.

[30] Zhang Y. First-principles Debye–Callaway approach to lattice thermal conductivity. J. Materiomics. 2016; 2(3): 237-247. https://doi.org/10.1016/j.jmat.2016.06.004.

[31] Xiang H, Feng Z, Li Z, Zhou Y. Theoretical investigations on mechanical and dynamical properties of MAlB (M=Mo, W) nanolaminated borides at ground-states and elevated temperatures. Sci. Rep. 2018; 8(1): 1-9. https://doi.org/10.1016/j.jallcom.2017.12.206.

[32] Xiang H, Wang J, Zhou Y. Theoretical predictions on intrinsic lattice thermal conductivity of $ZrB_2$. J. Eur. Ceram. Soc. 2019; 39(10): 2982-2988. https://doi.org/10.1016/j.jeurceramsoc.2019.04.011.

[33] Katoh Y, Vasudevamurthy G, Nozawa T, Snead LL. Properties of zirconium carbide for nuclear fuel applications. J. Nucl. Mater. 2013; 441(1-3): 718-742. 10.1016/j.jnucmat.2013.05.037.

[34] Zhou Y, Fahrenholtz WG, Graham J, Hilmas GE. From thermal conductive to thermal insulating: Effect of carbon vacancy content on lattice thermal conductivity of $ZrC_X$. J. Mater. Sci. Technol. 2021; 82: 105-113. https://doi.org/10.1016/j.jmst.2020.11.068.

[35] Pfrommer BG, Côté M, Louie SG, Cohen ML. Relaxation of crystals with the quasi-Newton method. J. Comput. Phys. 1997; 131(1): 233-240. https://doi.org/10.1006/jcph.1996.5612.

[36] Giannozzi P, Baroni S, Bonini N, Calandra M, Car R, Cavazzoni C et al. QUANTUM ESPRESSO: a modular and open-source software project for quantum simulations of materials. J. Phys.: Condens. Matter. 2009; 21(39): 395502. https://doi.org/10.1088/0953-8984/21/39/395502.

[37] Vanderbilt David. Soft self-consistent pseudopotentials in a generalized eigenvalue formalism. Phys. Rev. B. 1990; 41(11): 7892. https://doi.org/10.1103/PhysRevB.41.7892.

[38] Perdew JP, Burke K, Ernzerhof M. Generalized gradient approximation made simple. Phys. Rev. Lett. 1996; 77(18): 3865. https://doi.org/10.1103/PhysRevLett.77.3865.

[39] Monkhorst HJ, Pack JD. Special points for Brillouin-zone integrations. Phys. Rev. B. 1976; 13(12): 5188. https://doi.org/10.1103/PhysRevB.13.5188.

[40] Gonze X. First-principles responses of solids to atomic displacements and homogeneous electric fields: Implementation of a conjugate-gradient algorithm. Phys. Rev. B. 1997; 55(16): 10337. https://doi.org/10.1103/PhysRevB.55.10337.

[41] Morelli DT, Heremans JP, Slack GA. Estimation of the isotope effect on the lattice thermal conductivity of group IV and group III-V semiconductors. Phys. Rev. B. 2002; 66(19): 195304. https://doi.org/10.1103/PhysRevB.66.195304.

[42] Xiang H, Zhou Y. Phonon engineering in tuning the thermal conductivity of alkaline-earth hexaborides. J. Eur. Ceram. Soc. 2020;40(4):1352-1360. https://doi.org/10.1016/j.jeurceramsoc.2019.10.047.

[43] Asen-Palmer M, Bartkowski K, Gmelin E, Cardona M, Zhernov AP, Inyushkin AV et al. Thermal conductivity of germanium crystals with different isotopic compositions. Phys. Rev. B. 1997; 56(15): 9431. https://doi.org/10.1103/PhysRevB.56.9431.

[44] Lindsay L, Broido DA, Reinecke TL. Phonon-isotope scattering and thermal conductivity in materials with a large isotope effect: A first-principles study. Phys. Rev. B. 2013; 88(14): 144306. https://doi.org/10.1103/PhysRevB.88.144306.

[45] Klemens PG. The scattering of low-frequency lattice waves by static imperfections. Proceedings of the Physical Society. Section A. 1955; 68(12): 1113. https://doi.org/10.1088/0370-1298/68/12/303.

[46] Morelli DT, Heremans JP, Slack GA. Estimation of the isotope effect on the lattice thermal conductivity of group IV and group III-V semiconductors. Phys. Rev. B.2002; 66(19): 195304. https://doi.org/10.1103/PhysRevB.66.195304.

[47] Grimvall G. Thermophysical properties of materials. Amsterdam, Netherlands: Elsevier; 1999.

[48] Xiang H, Feng Z, Li Z, Zhou Y. First-principles investigations on elevated temperature elastic and thermodynamic properties of $ZrB_2$ and $HfB_2$. J. Am. Ceram. Soc. 2017; 100(8): 3662-3672. https://doi.org/10.1111/jace.14877.

[49] Opeka MM, Talmy IG, Wuchina EJ, Zaykoski JA, Causey SJ. Mechanical, thermal and oxidation properties of refractory hafnium and zirconium compounds. J. Eur. Ceram. Soc. 1999; 19(13-14): 2405-2414. https://doi.org/10.1016/S0955-2219(99)00129-6.

[50] Wuchina E, Opeka M, Causey S, Buesking K, Spain J, Cull A et al. Designing for ultrahigh-temperature applications: the mechanical and thermal properties of $HfB_2$, $HfC_x$, $HfN_x$ and αHf (N). J. Mater. Sci. 2004; 39(19): 5939-5949. https://doi.org/10.1023/B:JMSC.0000041690.06117.34.

[51] Chen H, Xiang H, Dai F, Liu J, Zhou Y. Low thermal conductivity and high porosity ZrC and HfC ceramics prepared by in-situ reduction reaction/partial sintering method for ultrahigh temperature applications. J. Mater. Sci. Technol. 2019;35(12):2778-2784. https://doi.org/10.1016/j.jmst.2019.05.044.

[52] Shimada S, Inagaki M, Matsui K. Oxidation kinetics of hafnium carbide in the temperature range of 480 to 600°C. J. Am. Ceram. Soc. 1992; 75(10): 2671-2678. https://doi.org/10.1111/j.1151-2916.1992.tb05487.x.

[53] Morelli D, Heremans J. Thermal Conductivity of Germanium-, Silicon-, and Carbon Nitride. Appl. Phys. Lett. 2003;81(27):8-10. https://doi.org/10.1063/1.1533840.

[54] Toberer ES, Zevalkink A, Snyder GJ. Phonon engineering through crystal chemistry. J. Mater. Chem. 2011;21(40):15843-15852. https://doi.org/10.1039/C1JM11754H.

# SECTION

# 3. SUMMARY AND OVERALL CONCLUSION

This research included $ZrC_x$ powder synthesis, phase formation analysis, and the investigation of the intrinsic thermal properties. Solid state powder synthesis was employed for prepare the samples for the synthesis and phase stability study. Characterizations were performed by XRD, TEM and neutron diffraction. First-principles calculations and the Debye-Callaway model were used for investigate the $ZrC_x$ intrinsic thermal properties.

$ZrC_x$ powders with different carbon vacancy contents were synthesized using starting materials of $ZrH_2$ and carbon black in different ratios by solid state reaction. Powders were synthesized at different temperatures to study the effects on the final particle size and the carbon stoichiometry. Single phase of $ZrC_x$ was achieved at temperatures as low as 1300°C, and carbon fully reacted with $ZrH_2$ at 1600°C. Crystallite size of the as-synthesized powder was not affected by the temperature below 1400°C. When the synthesis temperature was more than 1400°C, crystallite size increased with increasing temperature. All the synthesized powders were partially oxidized during synthesis. An oxidized layer was observed on particles by TEM. Part of the oxygen also dissolved into vacancies in the $ZrC_x$ lattice. Neutron diffraction results revealed that carbon content increased with increasing synthesis temperature, and the dissolved oxygen decreased with increasing carbon stoichiometry.

$ZrC_{0.6}$ powders were synthesized at 1300°C and 2000°C to study the ordering of carbon vacancies. According to XRD, the major phase of the powder synthesized at 1300°C was $ZrC_x$ with a small quantity of Zr. $ZrC_x$ was the only phase detected in the powder synthesized at 2000°C. Neutron diffraction analysis of both powders detected peaks for a $ZrC_{0.6}$ superlattice, which indicated ordering of vacancies on a length scale that was longer than the unit cell. Ordering was also supported by SAED. The degrees of vacancy ordering were about 20% and 25% for the powder synthesized at 1300°C and 2000°C.

The lattice thermal conductivities of $ZrC_x$ ceamics with different carbon vacancy (ZrC, $ZrC_{0.75}$ and $ZrC_{0.5}$) and Hf (3.125 wat% and 6.25 at%) contents were calculated by a combination method of Debye-Callaway model and first-principles calculations. Phonon dispersion curves for $ZrC_x$ were calculated as a function of Brillouin zone direction by the finite displacement method. The key parameters for lattice thermal conductivity calculation (Grüneisen parameter, Debye temperature, and group velocity) were determined based on the phonon dispersions. Lattice thermal conductivities decreased with increasing temperature for all compositions due to the effect of phonon-phonon scattering at high temperature. Lattice thermal conductivity also decreased with increasing carbon vacancy and Hf contents. Phonon frequency decreased with increasing carbon vacancy content, which reduced the thermal transport through the lattice. Consequently, $ZrC_x$ with $x = 1$ can be treated as a thermal dissipating material and $ZrC_{0.5}$ with a higher carbon vacancy content can be considered to be a thermal insulating material according to our calculation data. The effects of Zr isotopes, grain boundaries, and phonon-phonon interactions all decrease the lattice thermal conductivity of $ZrC_x$. The

ffect of Hf impurities on $ZrC_x$ thermal conductivity was also studied. The electronic structure did not change with the addition of Hf into $ZrC_x$, thus, the change of lattice thermal conductivity dominated the change of the total thermal conductivity. The lattice thermal conductivity of HfC was lower than ZrC. Hf impurities reduced the lattice thermal conductivity of $ZrC_x$ by decreasing of acoustic phonon frequencies.

Solid state reaction with starting materials of $ZrH_2$ and carbon black is better than carbothermal reduction method for synthesis $ZrC_x$. The existence of the ordered phase in $ZrC_{0.6}$ was proved experimentally. Together with previous theoretical studies, one can see that the Zr-C phase diagram needs additional experimental validation. Thermal conductivity of $ZrC_x$ can be tuned by adjusting the carbon stoichiometry and Hf content. That is another advantage for $ZrC_x$ applied in nuclear fuel compared to SiC.

# 4. SUGGESTIONS FOR FUTURE WORK

The forming conditions for vacancy ordered phases in $ZrC_x$ should be studied. $ZrC_{0.6}$ can be synthesized at 1300°C with a cooling rate of 10°C/min. According to a calculated Zr-C phase diagram, $ZrC_x$ with carbon content of 0.6 should form an ordered phase below 945°C, but experimental verification is needed. This could be done by quenching samples after synthesis at 1300°C (should be fully disordered), and annealing at 900°C after synthesis (should be fully ordered). Neutron diffraction and selected area electron diffraction could be employed to determine the degree of vacancy ordering. Hot-pressing can be used to prepare $ZrC_x$ ceramics with different carbon vacancy contents to determine the carbon stoichiometry range over which the ordered phases can be formed. Through the above experiments, the forming conditions for ordered $ZrC_x$ phases could be defined in terms of temperature, and carbon stoichiometry.

The effect of oxygen impurity content on the ordering of carbon vacancies in low stoichiometry $ZrC_x$ should be investigated. According to a calculated Zr-C-O phase diagram, zirconium oxycarbide can have carbon stoichiometry as low as 0.54 and a maximum oxygen stoichiometry of 0.298 ($ZrC_{0.54}O_{0.298}$) at 2000°C. This composition could potentially be synthesized by solid state reaction. The stable phase formed could be characterized by XRD, neutron diffraction, and SAED to determine the relative degrees of carbon vacancy ordering. Carbon and oxygen stoichiometry could be measured by combustion methods. This series of experiments could disclose the effect of dissolved oxygen atoms on the carbon ordering.

Thermal conductivity of $ZrC_x$ could be measured from room temperature to 2000°C by the laser flash method. A dilatometer can be used to measure the thermal expansion of the sample, then the density can be calculated. Specific thermal conductivities can be calculated based on heat capacities determined from the standard thermodynamic data. This methodology could be used to study the effects of carbon stoichiometry, hafnium content, and oxygen content on thermal conductivity since the thermal conductivity of the material needs to be known for nuclear applications.

# BIBLIOGRAPHY

[1] Nakamura K, Yashima M. Crystal structure of NaCl-type transition metal monocarbides MC (M= V, Ti, Nb, Ta, Hf, Zr), a neutron powder diffraction study. Mater Sci Eng, B. 2008;148(1–3):69–72.

[2] R.V. Sara. The system zirconium—carbon. J. Am. Ceram. Soc. 1965;48(5):243–247.

[3] H.O. Pierson. Handbook of Refractory Carbides and Nitrides: Properties, Characteristics, Processing and Applications. William Andrew, Norwich, NY, 1996.

[4] R.E. Taylor. Thermal Conductivity and Expansion of BeryIIia at High Temperatures. J. Am. Ceram. Soc.1962;45:74–78.

[5] L.N. Grossman. High-temperature thermophysical properties of zirconium carbide. J. Am. Ceram. Soc. 1965;48(5):236-242.

[6] Y. Katoh, G. Vasudevamurthy, T. Nozawa, L.L. Snead. Properties of zirconium carbide for nuclear fuel applications. J. Nucl. Mater. 2013;441(1-3):718–742.

[7] Shen X, Li K, Li H, Du H, Cao W, Lan F. Microstructure and ablation properties of zirconium carbide doped carbon/carbon composites. Carbon. 2010;48(2):344-351.

[8] Taylor RE. Thermal conductivity of zirconium carbide at high temperatures. J Amer Ceramic Soc. 1962;45(7):353-354.

[9] R.E. Taylor, J. Morreale. Thermal conductivity of titanium carbide, zirconium carbide, and titanium nitride at high temperatures. J. Am. Ceram. Soc. 1964;47(2):69–73.

[10] Fahrenholtz, William G., Eric J. Wuchina, William E. Lee, and Yanchun Zhou, eds. Ultra-high temperature ceramics: materials for extreme environment applications. John Wiley & Sons, 2014.

[11] B. Wei, L. Chen, Y. Wang, H. Zhang, S. Peng, J. Ouyang, D. Wang, Y. Zhou. Densification, mechanical and thermal properties of $ZrC_{1-x}$ ceramics fabricated by two-step reactive hot pressing of ZrC and ZrH2 powders. J. Eur.Ceram. Soc. 2018;38:411–419.

[12] X. Wei, C. Back, O. Izhvanov, C. Haines, E. Olevsky. Zirconium carbide produced by spark plasma sintering and hot pressing: densification kinetics, grain growth, and thermal properties. Materials. 2016;9:577.

[13] L.N. Grossman. High ‐ temperature thermophysical properties of zirconium carbide. J. Am. Ceram. Soc. 1965;48:236 ‐ 242.

[14] Margrave JL. Refractory Materials. Academic Press Inc, New York, NY, 1967.

[15] Hu W, Xiang J, Zhang Y, et al. Superstructural nanodomains of ordered carbon vacancies in nonstoichiometric $ZrC_{0.61}$. J Mater Res. 2012;27(9):1230.

[16] Naomi O, Noboru N. Superlattice formation in zirconium-carbon system. J Nucl Mater. 1976;60(1):39-42.

[17] Gusev AI, Rempel AA, Magerl AJ. Disorder and order in strongly nonstoichiometric compounds. Heidelberg: Springer, 2001.

[18] Gusev AI, Rempel SV. C - Zr // MSIT Workplace – Research Results. Stuttgart: MSI; 2002;50.12291.7.20:1-2.23.

[19] Gusev AI. Order-disorder transformations and phase equilibria in strongly nonstoichiometric compounds. Phys-Usp. 2000;43(1):1–37.

[20] Zhang Y, Liu B, Wang J. Self-assemstoichiometric $ZrC_{1-x}$. Sci Rep. 2015;5:18098.

[21] Xie Ciu N, Dong D, et al. Effects of carbon vacancies on the structures, mechanical properties, and chemical bonding of zirconium carbides: a first-principles-study. Phys Chem Chem Phys. 2016;18(17):12299-12306.

[22] W. Jones, N.H. March, Theoretical Solid State Physics. London, Great Britain: John Wiley & Sons; 1973.

[23] Radosevich LG, Williams WS. Thermal conductivity of transition metal carbides. J. Am. Ceram. Soc. 1970;53(1):30-33.

[24] Williams WS. High - temperature thermal conductivity of transition metal carbides and nitrides. J. Am. Ceram. Soc. 1966;49(3):156-159.

[25] Wei B, Chen L, Wang Y, et al. Densification, mechanical and thermal properties of $ZrC_{1-x}$ ceramics fabricated by two-step reactive hot pressing of ZrC and $ZrH_2$ powders. J. Eur. Ceram. Soc. 2018;38(2):411-419.

[26] Chen H, Xiang H, Dai F, Liu J, Zhou Y. Low thermal conductivity and high porosity ZrC and HfC ceramics prepared by in-situ reduction reaction/partial sintering method for ultrahigh temperature applications. J. Mater. Sci. Technol. 2019;35(12):2778-2784.

[27] Yan N, Fu Q, Zhang Y et al. Preparation of pore-controllable zirconium carbide ceramics with tunable mechanical strength, thermal conductivity and sound absorption coefficient. Ceram. Int. 2020;46(11):19609-19616.

[28] Gambogi J. Ind. Miner. 1994:311.

[29] Cui S, Suo H, Jing F et al. Facile preparation of ZrCO composite aerogel with high specific surface area and low thermal conductivity. J. Sol-Gel Sci. Technol. 2018;86(2):383-390.

[30] Y. Wang, Q. Liu, J. Liu, L. Zhang, L. Cheng. Deposition mechanism for chemical vapor deposition of zirconium carbide coatings. J. Am. Ceram. Soc. 2008;91(4):1249–1252.

[31] Q. Liu, L. Zhang, L. Cheng, Y. Wang. Morphologies and growth mechanisms of zirconium carbide films by chemical vapor deposition. J. Coat. Tech. Res. 2009;6(2):269–273.

[32] Ding J, Guo D, Deng C, Zhu H, Yu C. Low-temperature synthesis of nanocrystalline ZrC coatings on flake graphite by molten salts. Appl. Surf. Sci. 2017;407:315-321.

[33] [33] Song MS, Huang B, Zhang MX, Li JG. Formation and growth mechanism of ZrC hexagonal platelets synthesized by self-propagating reaction. J. Cryst. Growth. 2008;310(18):4290-4294.

[34] T. Tsuchida, M. Kawaguchi, K. Kodaira. Synthesis of ZrC and ZrN in air from mechanically activated Zr-C powder mixtures. Solid State Ion. 1997;101:149-154.

[35] B.K. Yen. X-ray diffraction study of mechanochemical synthesis and formation mechanisms of zirconium carbide and zirconium silicides. J. Alloys Comp. 1998;268(1-2):266-269.

[36] T. Tsuchida, S. Yamamoto. Mechanical activation assisted self-propagating hightemperature synthesis of ZrC and $ZrB_2$ in air from Zr/B/C powder mixtures. J. Eur. Ceram. Soc. 2004;24(1):45–51.

[37] M.D. Sacks, C.A. Wang, Z. Yang, A. Jain. Carbothermal reduction synthesis of nanocrystalline zirconium carbide and hafnium carbide powders using solution-derived precursors. J. Mater. Sci. 2004;39(19):6057–6066.

[38] M. Dolle, D. Gosset, C. Bogicevic, F. Karolak, D. Simeone, G. Baldinozzi. Synthesis of nanosized zirconium carbide by a sol–gel route. J. Eur. Ceram. Soc. 2007;27(4):2061–2067.

[39] J. Ding, D. Guo, C. Deng, H. Zhu, C. Yu. Low-temperature synthesis of nanocrystalline ZrC coatings on flake graphite by molten salts. Appl. Surf. Sci. 2017;407:315–321.

[40] L. Dai, X. Wang, H. Zhou, Y. Yu, J. Zhu, Y. Li, et al. Direct electrochemical synthesis of zirconium carbide from zirconia/C precursors in molten calcium chloride. Ceram. Int. 2015;41(3):4182–4188.

[41] Y. Leconte, H. Maskrot, L. Combemale, N. Herlin-Boime, C. Reynaud. Application of the laser pyrolysis to the synthesis of SiC, TiC and ZrC pre-ceramics nanopowders. J. Anal. Appl. Pyrolysis. 2007;79(1-2):465-470.

[42] L. Combemale, Y. Leconte, X. Portier, N. Herlin-Boime, C. Reynaud. Synthesis of nanosized zirconium carbide by laser pyrolysis route. J. Alloys Comp. 2009;483(1-2):468-472.

[43] [43] Mahday AA., El-Eskandarany MF, Ahmed HA, Amer AA. Mechanically induced solid state carburization for fabrication of nanocrystalline ZrC refractory material powders. J. Alloys Compd. 2000;299(1-2):244-253.

[44] P. Barnier, C. Brodhag, F. Thevenot. Hot-pressing kinetics of zirconium carbide. J. Mater. Sci. 1986;21(7):2547-2552.

[45] Nachiappan C, Rangaraj L, Divakar C, Jayaram V. Synthesis and densification of monolithic zirconium carbide by reactive hot pressing. J. Am. Ceram. Soc. 2010;93(5):1341-1346.

[46] Chakrabarti T, Rangaraj L, Jayaram V. Computational modeling of reactive hot pressing of zirconium carbide. J. Mater. Res. 2015;30(12):1876-1886.

[47] Kuriakose AK, Margrave JL. The oxidation kinetics of zirconium diboride and zirconium carbide at high temperatures. J. Electrochem. Soc. 1964;111(7):827.

[48] Sarkar SK, Miller AD, Mueller JI. Solubility of oxygen in ZrC. J. Am. Ceram. Soc. 1972;55(12):628-630.

[49] Barnier P, Thévenot F. Synthesis and hot-pressing of single-phase ZrCxOy and two-phase $ZrC_xO_y$ - $ZrO_2$ materials. Int. J. High Technol. Ceram. 1986:2(4):291-307.

[50] Shimada S, Ishil T. Oxidation kinetics of zirconium carbide at relatively low temperatures. J. Am. Ceram. Soc. 1990;73(10):2804-2808.

[51] Rao GAR, Venugopal V. Kinetics and mechanism of the oxidation of ZrC. J. Alloys Compd. 1994;206(2):237-242.

[52] Shimada S, Nishisako M, Inagaki M, Yamamoto K. Formation and microstructure of carbon - containing oxide scales by oxidation of single crystals of zirconium carbide J. Am. Ceram. Soc. 1995;78(1):41-48.

[53] Shimada S, Inagaki M, Suzuki M. Microstructural observation of the $ZrC/ZrO_2$ interface formed by oxidation of ZrC. J. Mater. Res. 1996;11(10):2594-2597.

[54] Bellucci A, Gozzi D, Kimura T, Noda T, Otani S. Zirconia growth on zirconium carbide single crystals by oxidation. Surf. Coat. Technol. 2005;197(2-3):294-302.

[55] Gasparrini C, Podor R, Horlait D, Chater R, Lee WE. Zirconium carbide oxidation: Maltese cross formation and interface characterization. Oxid. Met. 2017;88(3):509-519.

[56] Gendre M, Maitre A, Trolliard G. A study of the densification mechanisms during spark plasma sintering of zirconium (oxy-) carbide powders. Acta Mater. 2010;58(7):2598-2609.

[57] Hu W, Xiang J, Liu S, Zhang Y, Chen C, Wang P et al. Low-temperature diffusion of oxygen through ordered carbon vacancies in $Zr_2C_x$: The formation of ordered $Zr_2C_xO_y$. Inorganic chemistry. 2012;51(9):5164-5172.

[58] Réjasse F, Rapaud O, Trolliard G, Masson O, Maitre A. Experimental investigation and thermodynamic evaluation of the C–O–Zr ternary system. RSC advances. 2016;6(102):100122-100135.

[59] Jackson HF, Jayaseelan DD, Manara D, Casoni CP, Lee WE. Laser melting of zirconium carbide: determination of phase transitions in refractory ceramic systems. J. Am. Ceram. Soc. 2011;94(10):3561-3569.

[60] Silva E, de Figueiredo MR, Franz R, Galindo RE, Palacio C, Espinosa A et al. Structure–property relations in ZrCN coatings for tribological applications. Surf. Coat. Technol. 2010;205(7):2134-2141.

[61] Harrison R, Rapaud O, Pradeilles N, Maître A, Lee WE. On the fabrication of ZrCxNy from ZrO2 via two-step carbothermic reduction–nitridation. J. Eur. Ceram. Soc. 2015;35(5):1413-1421.

[62] Ueta S, Aihara J, Yasuda A, Ishibashi H, Takayama T, Sawa K. Fabrication of uniform ZrC coating layer for the coated fuel particle of the very high temperature reactor. J. Nucl. Mater. 2008;376(2):146-151.

[63] López-Honorato E, Tan J, Meadows PJ, Marsh G, Xiao P. TRISO coated fuel particles with enhanced SiC properties. J. Nucl. Mater. 2009;392(2):219-224.

[64] Reynolds GH, Janvier JC, Kaae JL, Morlevat JP. Irradiation behavior of experimental fuel particles containing chemically vapor deposited zirconium carbide coatings. J. Nucl. Mater. 1976;62(1):9-16.

[65] Kim S, Szlufarska I, Morgan D. Ab initio study of point defect structures and energetics in ZrC. J. Appl. Phys. 2010;107(5):053521.

[66] Auskern A. Rare gas diffusion in nonstoichiometric zirconium carbide. J. Nucl. Mater. 1967;22(3):257-268.

[67] Fukuda K, Ikawa K, Iwamoto K. Fission product diffusion in ZrC coated fuel particles. J. Nucl. Mater. 1979;87(2-3):367-374.

[68] Bullock RE, Kaae JL. Performance of coated $UO_2$ particles gettered with ZrC. J. Nucl. Mater. 1983;115(1):69-83.

[69] Bullock RE. Fission-product release during postirradiation annealing of several types of coated fuel particles. J. Nucl. Mater. 1984;125(3):304-319.

[70] Snead LL, Katoh Y, Kondo S. Effects of fast neutron irradiation on zirconium carbide. J. Nucl. Mater. 2010;399(2-3):200-207.

[71] Motta A, Sridharan K, Morgan D, Szlufarska I. Understanding the Irradiation Behavior of Zirconium Carbide. No. DOE/NEUP-10-679. Pennsylvania State Univ., University Park, PA (United States); Univ. of Wisconsin, Madison, WI (United States), 2013.

[72] Gusev AI, Rempel AA. Calculation of phase diagrams of interstitial compounds. J. Phys. Chem. Solids. 1994;55(3):299-304.

[73] Kim S, Szlufarska I, Morgan D. Ab initio study of point defect structures and energetics in ZrC. J. Appl. Phys. 2010;107(5):053521.

[74] Zhang Y, Bin Liu B, Wang J. Self-assembly of carbon vacancies in sub-stoichiometric $ZrC_{1-x}$. Sci. Rep. 2015;5(1):1-9.

[75] Zhang Y, Liu B, Wang J, Wang J. Theoretical investigations of the effects of ordered carbon vacancies in $ZrC_{1-x}$ on phase stability and thermo-mechanical properties. Acta Mater. 2016;111:232-241.

[76] Yu XX, Weinberger CR, Thompson GB. Ab initio investigations of the phase stability in group IVB and VB transition metal carbides. Comput. Mater. Sci. 2016;112:318-326.

[77] Li H, Zhang L, Zeng Q, Guan K, Li K, Ren H et al. Structural, elastic and electronic properties of transition metal carbides TMC (TM= Ti, Zr, Hf and Ta) from first-principles calculations. Solid State Commun. 2011;151(8):602-606.

[78] Weber W. Lattice dynamics of transition-metal carbides. Phys. Rev. B. 1973;8(11):5082.

[79] Fu H, Peng W, Gao T. Structural and elastic properties of ZrC under high pressure. Mater. Chem. Phys. 2009;115(2-3):789-794.

[80] Crocombette JP. Origins of the high temperature increase of the thermal conductivity of transition metal carbides from atomistic simulations. J. Phys.: Condens. Matter. 2013;25(50):505501.

[81] Mellan TA, Aziz A, Xia Y, Grau-Crespo R, Duff AI. Electron and Phonon Interactions and Transport in Ultra-High-Temperature Ceramic ZrC. Phys. Rev. B. 2019;99:094310.

[82] Song GM, Wang YJ, Zhou Y. Elevated temperature ablation resistance and thermophysical properties of tungsten matrix composites reinforced with ZrC particles. J. Mater. Sci. 2001;36(19):4625-4631.

[83] Dickerson MB, Wurm PJ, Schorr JR, Hoffman WP, Wapner PG, Sandhage KH. Near net-shape, ultra-high melting, recession-resistant ZrC/W-based rocket nozzle liners via the displacive compensation of porosity (DCP) method. J. Mater. Sci. 2004;39(19):6005-6015.

[84] Zhuang L, Fu Q, Tan B, Guo Y, Ren Q, Li H et al. Ablation behaviour of C/C and C/C–ZrC–SiC composites with cone-shaped holes under an oxyacetylene flame. Corros. Sci. 2016;102:84-92.

[85] Sorrell CC, Stubican VS, Bradt RC. Mechanical properties of ZrC - $ZrB_2$ and ZrC - $TiB_2$ directionally solidified eutectics. J. Am. Ceram. Soc. 1986;69(4):317-321.

[86] Zhang GJ, Ando M, Yang JF, Ohji T, Kanzaki S. Boron carbide and nitride as reactants for in situ synthesis of boride-containing ceramic composites. J. Eur. Ceram. Soc. 2004;24(2):171-178.

[87] Xu L, Huang C, Liu H, Zou B, Zhu H, Zhao G et al. Study on in-situ synthesis of $ZrB_2$ whiskers in $ZrB_2$–ZrC matrix powder for ceramic cutting tools. Int. J. Refract. Met. Hard Mater. 2013;37:98-105.

[88] Wagner P. High-temperature fuel technology for nuclear process heat: ZrC-containing coated particle fuels and high-density graphite fuel matrices. No. LA-6984. Los Alamos Scientific Lab., N. Mex.(USA), 1977.

[89] Ogawa T, Fukuda K, Kashimura S, Tobita T, Kobayashi F, Kado S et al. Performance of ZrC - Coated Particle Fuel in Irradiation and Postirradiation Heating Tests. J. Am. Ceram. Soc. 1992;75(11):2985-2990.

[90] Zhao D, Zhang C, Hu H, Zhang Y. Preparation and characterization of three-dimensional carbon fiber reinforced zirconium carbide composite by precursor infiltration and pyrolysis process. Ceram. Int. 2011;37(7):2089-2093.

[91] Zhu Y, Wang S, Li W, Zhang S, Chen Z. Preparation of carbon fiber-reinforced zirconium carbide matrix composites by reactive melt infiltration at relative low temperature. Scr. Mater. 2012;67(10):822-825.

[92] Porter IE, Knight TW, Dulude MC, Roberts E, Hobbs J. Design and fabrication of an advanced TRISO fuel with ZrC coating. Nucl. Eng. Des. 2013;259:180-186.

[93] Sani E, Mercatelli L, Meucci M, Balbo A, Silvestroni L, Sciti D. Compositional dependence of optical properties of zirconium, hafnium and tantalum carbides for solar absorber applications. Sol. Energy. 2016;131:199-207.

[94] Charbonnier FM, Mackie WA, Xie T, Davis PR. Enhanced field emission from carbide-coated field emitters, and device applications. Ultramicroscopy. 1999;79(1-4):73-82.

# VITA

Yue Zhou was raised in Institute of Metal Research, Chinese Academy of Science. When Yue was a little child, materials characterization scopes attracted him a lot. Magic surface morphologies under high magnification made him want dig into the materials.

Yue pursued a Master of Science degree of mechanical engineering in West Virginia University, received in July 2016. Yue was a graduate assistant focused on enhancing the ionic conductivity of solid-state electrolyte LaLiTiO3, and tried to assemble, and test the properties of zinc-air fuel cell. After he finished his research program, he tried to calculate some properties of LaLiTiO3 using DFT method. He also responded to the TEM characterization for the research group, and collaborated with National Energy Technology Lab. During his master's period, he published three papers as co-author.

Yue started the PhD program in July 2017 at Missouri S&T, majoring in Materials Science and Engineering. His research focused on the intrinsic properties of zirconium carbide. During this time, he had four presentations in International Conference and Expo on Advanced Ceramics and Composites, published four papers as first author, and published four as co-author.

Yue received the Doctor of Philosophy in Materials Science and Engineering in July 2021 from Missouri University of Science and Technology.